การจำลองเชิงตัวเลขของการไหลหมุนวนแบบไม่ยุบตัว
โดยใช้วิธีผลต่างอันตะ

นางสาวกัญญุตา ภู่ชินาพันธุ์

A NUMERICAL SIMULATION OF INCOMPRESSIBLE SWIRLING FLOW USING FINITE DIFFERENCE METHOD

Kanyuta Poochinapan

A Thesis Submitted in Partial Fulfillment of the Requirements

for the Degree of Doctor of Philosophy in Applied Mathematics

Suranaree University of Technology

Academic Year 2007

A NUMERICAL SIMULATION OF INCOMPRESSIBLE SWIRLING FLOW USING FINITE DIFFERENCE METHOD

Suranaree University of Technology has approved this thesis submitted in partial fulfillment of the requirements for the Degree of Doctor of Philosophy.

Thesis Examining Committee

_____

(Assoc. Prof. Dr. Prapasri Asawakun)

Chairperson

_____

(Assoc. Prof. Dr. Nikolay Moshkin)

Member (Thesis Advisor)

_____

(Assoc. Prof. Dr. Varangrat Juntasaro)

Member

_____

(Prof. Dr. Sergey Meleshko)

Member

_____

(Assoc. Prof. Dr. Ekachai Juntasaro)

Member

_____   _____

(Prof. Dr. Pairote Sattayatham)   (Assoc. Prof. Dr. Prapan Manyum)

Vice Rector for Academic Affairs   Dean of Institute of Science

กัญญุตา ภู่ชินาพันธุ์ : การจำลองเชิงตัวเลขของการไหลหมุนวนแบบไม่ยุบตัวโดยใช้วิธี ผลต่างอันตะ (A NUMERICAL SIMULATION OF INCOMPRESSIBLE SWIRLING FLOW USING FINITE DIFFERENCE METHOD) อาจารย์ที่ปรึกษา : รองศาสตราจารย์ ดร.นิโคไลน์ มอสกิน, 140 หน้า.

งานวิจัยนี้ศึกษาเกี่ยวกับการจำลองเชิงตัวเลขของการไหลมีความหนืดแบบไม่ยุบตัวในสอง มิติที่ควบคุมโดยสมการนาเวียร์สโตก การศึกษาครั้งนี้แบ่งเป็นสองส่วน ส่วนแรกเป็นการตรวจสอบ และเปรียบเทียบประสิทธิภาพของวิธีผลต่างอันตะสามวิธี เพื่อหาคำตอบโดยประมาณของสมการนา เวียร์สโตกแบบไม่ยุบตัวในสองมิติในรูปแบบของฟังก์ชันกระแส ส่วนที่สองเป็นการพัฒนาและ ศึกษาวิธีผลต่างอันตะเพื่อจำลองการไหลแบบไม่ยุบตัวในสองมิติในรูปแบบใหม่ที่เสนอโดย อริ สตอฟ และ พุกเนเชฟ (Aristov and Pukhnachev, Doklady Physics, 49(2), 2004)

ปัญหาของการไหลในโพรงแบบสองมิติใช้เป็นบรรทัดฐานในการเปรียบเทียบวิธีผลต่าง อันตะสามวิธี สำหรับคำตอบโดยประมาณของสมการนาเวียร์สโตกในรูปแบบของสมการทวิฮาร์มอ นิกสำหรับฟังก์ชันกระแส การประมาณของพจน์ที่ไม่เชิงเส้นทำให้วิธีทั้งสามมีความแตกต่างกันนั่น คือ การประมาณแบบชัดแจ้ง, การทำซ้ำภายใน และการแยกตัวดำเนินการ เทคนิคการหาคำตอบทั้ง สามแบบนี้มีการเปรียบเทียบในแง่ของความเสถียร ความถูกต้อง และอัตราการลู่เข้า งานวิจัยครั้งนี้ แสดงให้เห็นว่า วิธี การแยกตัวดำเนินการที่เสถียรทางทฤษฎีล้มเหลวที่ค่าเรย์โนลด์สูง ในขณะที่ วิธีการทำซ้ำภายใน ได้คำตอบโดยประมาณด้วยอัตราการลู่เข้าที่เร็วกว่า

รูปแบบใหม่ของสมการนาเวียร์สโตก สำหรับการไหลของของไหลที่มีความหนืดแบบไม่ ยุบตัวในสองมิติเสนอโดย อริสตอฟ และ พุกเนเชฟ (2004) นั้นได้แนะนำฟังก์ชันใหม่ซึ่งสัมพันธ์ กับความดัน และประสบความสำเร็จในการเชื่อมต่อกันเป็นระบบของสมการขนส่งสองสมการ สำหรับฟังก์ชันกระแสและความเร็วเชิงมุม และสมการอิลลิปติกสำหรับฟังก์ชันใหม่ ขั้นตอนการ คำนวณเชิงตัวเลขใช้สมการที่เป็นระบบเชื่อมต่อแบบแยกจากกันไม่ได้ ซึ่งยอมให้ใช้เงื่อนไขสอง เงื่อนไขสำหรับฟังก์ชันกระแสที่ไม่มีเงื่อนไขจากฟังก์ชันช่วย การเพิ่มพารามิเตอร์ขนาดเล็กใน เงื่อนไขขอบช่วยกำจัดภาวะเอกฐานของเมทริกซ์ได้ เครื่องมือเชิงตัวเลขแบบใหม่นี้ถูกนำมา ประยุกต์ใช้กับการไหลแบบเทย์เลอร์- คูเอทท์ ระหว่างสองทรงกระบอกที่มีจุดศูนย์กลางร่วมกันโดย ที่ขอบบนและขอบล่างมีการหมุนเป็นอิสระจากท่อด้านใน ในขณะที่ท่อด้านนอกหยุดนิ่ง การไหลนี้ ถูกขับเคลื่อนถูกใช้เป็นแบบทดสอบมาตรฐานในกรณีสองมิติ วิธีเหล่านี้ได้รับการตรวจสอบบนกริด ที่มีความละเอียดแตกต่างกัน

วิธีการเชิงตัวเลขที่พัฒนาขึ้นในงานวิจัยนี้มีพื้นฐานจากรูปแบบเชิงทฤษฎีของอริสตอฟและ
พุกเนเชฟของสมการนาเวียร์สโตกสามารถใช้สำหรับศึกษาปรากฏการณ์ใหม่ในการไหลสองมิติ
แบบหมุนวนและแบบระนาบ

สาขาวิชาคณิตศาสตร์   ลายมือชื่อนักศึกษา_____

ปีการศึกษา 2550   ลายมือชื่ออาจารย์ที่ปรึกษา_____

                                                         ลายมือชื่ออาจารย์ที่ปรึกษาร่วม_____

KANYUTA POOCHINAPAN : A NUMERICAL SIMULATION OF
INCOMPRESSIBLE SWIRLING FLOW USING FINITE
DIFFERENCE METHOD. THESIS ADVISOR : ASSOC. PROF.
NIKOLAY MOSHKIN, Ph.D. 140 PP.

FINITE DIFFERENCE METHOD/ 2D FLOW/ NAVIER-STOKES EQUA-
TIONS.

The current work deals with a numerical simulation of 2D incompressible
viscous flow governed by the Navier-Stokes equations. This study can be divided
into two parts. The first part is the investigation and comparison of the perfor-
mance of three finite-difference schemes to find the approximate solution of 2D
incompressible Navier-Stokes equations in form of the stream function. The sec-
ond part is the development and study of a finite-difference scheme to simulate
the 2D incompressible flow in a new form proposed by Aristov and Pukhnachev
(see Doklady Physics, 49(2), 2004).

The benchmark problem of 2D cavity flow is used to compare three finite-
difference schemes for the approximate solution of the Navier-Stokes equations
in form of the bi-harmonic equation for the stream function. The schemes are
different for the approximation of nonlinear terms, that is, the explicit approxima-
tion, the internal iteration techniques, and the operator splitting approach. Three
techniques are compared in terms of their stability, accuracy, and convergence
rate. It is shown that the theoretically stable operator splitting scheme fails at
large Reynolds number while the method of internal iteration gives the reasonable
approximate solution and has the faster convergence rate.

The new form of the Navier-Stokes equations for the 2D viscous incompressible fluid flow proposed by Aristov and Pukhnachev (2004) who introduced a new function related to the pressure and succeed to derive a coupled system of two transport equations for the stream function and azimuthal component velocity and one elliptic equation for the new function. The algorithm treats the equations as an inextricably coupled system which allows to satisfy two conditions for the stream function without condition on the auxiliary function. The issue of singularity of the matrix is tackled by adding a small parameter in the boundary conditions. This new numerical tool is applied to the Taylor-Couette flow between the concentric rotating cylinders where the upper and lower lids are allowed to rotate independently from the inner cylinder, while the outer cylinder is held at rest. This flow is utilized as a benchmark test in 2D case. The schemes are thoroughly validated on grids with different resolutions.

The numerical methods developed in this research work based on Aristov and Pukhnachev formulation of the Navier-Stokes equations can be used in the future for in-depth investigations of the new phenomena in rotating and plane 2D flows.

School of Mathematics

Academic Year 2007

Student's Signature_____

Advisor's Signature_____

Co-advisor's Signature_____

ACKNOWLEDGEMENTS

CONTENTS

CONTENTS (Continued)

CONTENTS (Continued)

CONTENTS (Continued)

LIST OF TABLES

LIST OF TABLES (Continued)

LIST OF FIGURES

LIST OF FIGURES (Continued)

LIST OF FIGURES (Continued)

LIST OF FIGURES (Continued)

CHAPTER I

INTRODUCTION

In this chapter, a briefly introduction to mathematical model of a viscous incompressible fluid flow is provided. Different forms of the Navier-Stokes equations (NSEs) are discussed. Mostly, two-dimensional (2D) cases are considered. A new form of the NSEs proposed by Aristov and Pukhnachev (2004) is represented.

1.1 The Navier-Stokes equations of a viscous incompressible fluid motion in general case

The flow problem is described in terms of the velocity field and pressure. The governing equations of a viscous incompressible fluid motion are the NSEs

$$\frac{d\bar{v}}{dt} = -\nabla p + \nu \nabla^2 \bar{v}, \tag{1.1}$$

coupled by the continuity equation

$$\nabla \cdot \bar{v} = 0. \tag{1.2}$$

Here $\bar{v}$ is the velocity vector, p is the pressure divided by the constant density, and ν is the coefficient of kinematic viscosity. The kinematic viscosity ν is assumed to be constant.

1.2 The Navier-Stokes equations in form of vorticity-stream function in 2D plane

The example of 2D flow provides fluid motions parallel to the plane xy. In many handbook, one can find different form of the NSEs. In this representation, Quartapelle (1993) is followed. The 2D incompressible NSEs can be formulated by introducing two scalar variables, the vorticity ω and stream function ψ, in place of the primitive variables, the velocity $\bar{v}$ and pressure p. The scalar vorticity ω is the $z-$component of the vorticity vector $\bar{\omega} = \nabla \times \bar{v}$, normal to the plane, namely,

$$\omega = \nabla \times \bar{v} \cdot \bar{k}, \tag{1.3}$$

where $\bar{v} = (u, v)$, $\nabla = \left(\dfrac{\partial}{\partial x}, \dfrac{\partial}{\partial y} \right)$ and $\bar{k}$ is unit vector normal to the plane xy.

In 2D, the condition of incompressibility $\nabla \cdot \bar{v} = 0$ can be satisfied exactly by expressing $\bar{v}$ in terms of the stream function ψ according to

$$\bar{v} = \nabla \psi \times \bar{k}.$$

This equation, one expressed in terms of the vector components, gives $u = \dfrac{\partial \psi}{\partial y}$ and $v = -\dfrac{\partial \psi}{\partial x}$. Thus, one obtains immediately

$$\nabla \cdot \bar{v} = \nabla \cdot (\nabla \psi \times \bar{k}) = \frac{\partial}{\partial x} \left(\frac{\partial \psi}{\partial y} \right) + \frac{\partial}{\partial y} \left(-\frac{\partial \psi}{\partial x} \right) = 0.$$

In conclusion, taking the curl of the momentum equation (1.1) and make use of the fact that the *curl* of a *gradient* of a scalar ($\nabla \times (\nabla p)$) is zero (so that the pressure terms go away) leads to the vorticity transport equation

$$\frac{\partial \omega}{\partial t} + \frac{\partial \psi}{\partial y} \frac{\partial \omega}{\partial x} - \frac{\partial \psi}{\partial x} \frac{\partial \omega}{\partial y} = \nu \nabla^2 \omega.$$

On the other hand, substitution of the expression $\bar{v} = \nabla \psi \times \bar{k}$, into the vorticity definition (1.3) gives the Poisson equation for the stream function

$$\nabla^2 \psi = -\omega.$$
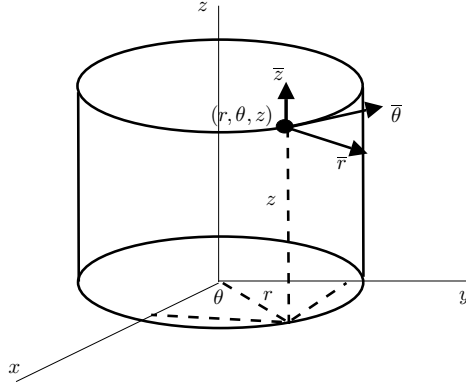
Figure 1.1 Cylindrical polar coordinates system.

The vorticity-stream function formulation of the NSEs for 2D flow are

$$\frac{\partial \omega}{\partial t} + \frac{\partial \psi}{\partial y}\frac{\partial \omega}{\partial x} - \frac{\partial \psi}{\partial x}\frac{\partial \omega}{\partial y} = \nu \nabla^2 \omega, \qquad (1.4)$$

$$\nabla^2 \psi = -\omega. \qquad (1.5)$$

Substitution of $\omega = -\nabla^2 \psi$ into the vorticity transport equation (1.4), one has the following time dependent bi-harmonic equation

$$\frac{\partial \nabla^2 \psi}{\partial t} + \frac{\partial \psi}{\partial y}\frac{\partial \nabla^2 \psi}{\partial x} - \frac{\partial \psi}{\partial x}\frac{\partial \nabla^2 \psi}{\partial y} = \nu \nabla^4 \psi. \qquad (1.6)$$

1.3   The Navier-Stokes equations of 2D axisymmetric flow in cylindrical polar coordinates

An axisymmetric flow is a subject of much interest in many areas of engineering and has been investigated by many researchers. An axisymmetric flow is one of the many cases where the NSEs reduce to the 2D problem. There have been a number of experimental and numerical studies of axisymmetric flows (see some of them, Levit, 1989; Lopez and Perry, 1992a, 1992b; Inamuro, 1997; Stevens, Lopez, and Cantwell, 1999; Iwatsu, 2004).

An axisymmetric flow is most conveniently described in terms of the cylindrical polar coordinates (r, θ, z). The cylindrical polar coordinate system (r, θ, z) is illustrated in Figure 1.1, where r, θ, and z denote the radial, azimuthal, and axial coordinates, respectively. The corresponding velocity vector is denoted by $\bar{v} = (u, v, w)^T$. The NSEs for a viscous incompressible fluid can be written as

$$u_t + uu_r + \frac{v}{r}u_\theta + wu_z - \frac{v^2}{r} = -p_r + \nu\left(\nabla^2 u - \frac{u}{r^2} - \frac{2}{r^2}v_\theta\right), \qquad (1.7)$$

$$v_t + vv_r + \frac{v}{r}v_\theta + wv_z + \frac{uv}{r} = -\frac{1}{r}p_\theta + \nu\left(\nabla^2 v - \frac{v}{r^2} + \frac{2}{r^2}u_\theta\right), \qquad (1.8)$$

$$w_t + uw_r + \frac{v}{r}w_\theta + ww_z = -p_z + \nu\nabla^2 w, \qquad (1.9)$$

$$\frac{1}{r}(ru)_r + \frac{1}{r}v_\theta + w_z = 0, \qquad (1.10)$$

where the Laplace operator in cylindrical coordinates takes the form

$$\nabla^2 = \frac{1}{r}\frac{\partial}{\partial r}\left(r\frac{\partial}{\partial r}\right) + \frac{1}{r^2}\frac{\partial^2}{\partial\theta^2} + \frac{\partial^2}{\partial z^2}.$$

The assumption of axisymmetry implies that the velocity components and pressure are functions of r and z only. Therefore, the NSEs (1.7)–(1.10) in the case of the axisymmetric flow can be reformulated as follows

$$u_t + uu_r + wu_z - \frac{v^2}{r} = -p_r + \nu\left(u_{rr} + \frac{1}{r}u_r - \frac{1}{r^2}u + u_{zz}\right), \qquad (1.11)$$

$$v_t + uv_r + wv_z + \frac{uv}{r} = \nu\left(v_{rr} + \frac{1}{r}v_r - \frac{1}{r^2}v + v_{zz}\right), \qquad (1.12)$$

$$w_t + uw_r + ww_z = -p_z + \nu\left(w_{rr} + \frac{1}{r}w_z + w_{zz}\right), \qquad (1.13)$$

$$u_r + \frac{u}{r} + w_z = 0. \qquad (1.14)$$

1.4 The Navier-Stokes equations of axisymmetric flow in form of vorticity-stream function and angular momentum

For the axisymmetric flow, one can define a stream function in the cylindrical polar coordinates

$$u = -\frac{1}{r}\psi_z \quad , \quad w = \frac{1}{r}\psi_r. \tag{1.15}$$

The azimuthal component of vorticity is

$$\omega = -\frac{1}{r}\frac{\partial^2 \psi}{\partial z^2} - \frac{\partial}{\partial r}\left(\frac{1}{r}\frac{\partial \psi}{\partial r}\right). \tag{1.16}$$

It is convenient to introduce the angular momentum $J = rv$. Here J is proportional to the circulation. The axisymmetric NSEs in terms of ψ, J, and ω (see for example, Lopez, 1994) are

$$J_t - \frac{1}{r}\psi_z J_r + \frac{1}{r}\psi_r J_z = \nu \mathbf{E}J, \tag{1.17}$$

$$\frac{\partial \omega}{\partial t} + \frac{1}{r^2}\psi_z \omega - \frac{1}{r}\psi_z \omega_r + \frac{1}{r}\psi_r \omega_z - \frac{2}{r^3}JJ_z = \nu\left(\mathbf{E}\omega + \frac{2}{r}\omega_r - \frac{1}{r^2}\omega\right), \tag{1.18}$$

$$\mathbf{E}\psi = -r\omega, \tag{1.19}$$

where

$$\mathbf{E} = \frac{\partial^2}{\partial r^2} - \frac{1}{r}\frac{\partial}{\partial r} + \frac{\partial^2}{\partial z^2}$$

is the Stokes operator. Substituting $\mathbf{E}\psi = -r\omega$ into equation (1.18) gives the following form of the NSEs in terms of the stream function and angular momentum

$$J_t - \frac{1}{r}\psi_z J_r + \frac{1}{r}\psi_r J_z = \nu \mathbf{E}J, \tag{1.20}$$

$$\frac{\partial \mathbf{E}\psi}{\partial t} + \frac{2}{r^2}\psi_z \mathbf{E}\psi - \frac{1}{r}\psi_z(\mathbf{E}\psi)_r + \frac{1}{r}\psi_r(\mathbf{E}\psi)_z + \frac{2}{r^2}JJ_z = \nu\mathbf{E}^2\psi. \tag{1.21}$$

1.5 The Navier-Stokes equations of axisymmetric flow in Aristov-Pukhnachev's form

To represent a new form of the NSEs, the results of Aristov and Pukhnachev (2004) are being followed. The axisymmetric NSEs are written using the cylindrical polar coordinate system (r, θ, z). It is well known that a system of equations (1.11)– (1.14) reduces to two equations for the azimuthal velocity component v and stream function ψ. A new form is based on the following observation. Firstly, substituting equation (1.15) into equation (1.13), one gets

$$\frac{\partial}{\partial r}\left(\psi_t - \frac{1}{r}\psi_r\psi_z - \nu\mathbf{E}\psi\right) + \frac{\partial}{\partial z}\left(rp + \frac{1}{r}\psi_r^2\right) = 0. \tag{1.22}$$

Therefore, there is a function Φ satisfying the relations

$$p = -\frac{1}{r^2}\psi_r^2 + \frac{1}{r}\Phi_r, \tag{1.23}$$

$$\psi_t - \frac{1}{r}\psi_r\psi_z + \Phi_z = \nu\mathbf{E}\psi. \tag{1.24}$$

By the same way, substituting equation (1.15) into equation (1.12), which reads

$$v_t - \frac{1}{r}\psi_z v_r + \frac{1}{r}\psi_r v_z - \frac{v}{r^2}\psi_z = \nu\left(v_{rr} + \frac{1}{r}v_r - \frac{1}{r^2}v + v_{zz}\right).$$

Denote $J = rv$, the equation above becomes

$$J_t - \frac{1}{r}\psi_z\left(rv_r + v\right) + \frac{1}{r}\psi_r r\psi_z = \nu\left(rv_{rr} + 2v_r - v_r - \frac{1}{r}v + rv_{zz}\right).$$

Equation (1.12) can be written in the following form

$$J_t - \frac{1}{r}\psi_z J_r + \frac{1}{r}\psi_r J_z = \nu\mathbf{E}J. \tag{1.25}$$

Differentiating equations (1.23) and (1.24) with respect to r and z, respectively, and substituting the resulting expressions into equation (1.11), where u and w are expressed in terms of ψ obtaining

$$\mathbf{E}\Phi = \frac{1}{r^2}\left(J^2 + \psi_z^2\right) + \frac{2}{r}\psi_r\,\mathbf{E}\psi. \tag{1.26}$$

The system of differential equations (1.24), (1.25), and (1.26) is the new form of the NSEs.

1.6 The 2D plane Navier-Stokes equations in Aristov-Pukhnachev's form

The fluid motions parallel to the plane xy are assumed. Next, the transformation of the viscous incompressible NSEs in 2D to a new form will be represented. The NSEs in the Cartesian coordinate system (x, y) are

$$u_t + uu_x + vu_y = -p_x + \nu\left(u_{xx} + u_{yy}\right), \tag{1.27}$$

$$v_t + uv_x + vv_y = -p_y + \nu\left(v_{xx} + v_{yy}\right), \tag{1.28}$$

$$u_x + v_y = 0, \tag{1.29}$$

where u and v are the velocity components in $x-$ and $y-$directions, respectively, p is the pressure, and ν is the kinematic viscosity. Without loss of generality, the fluid density is taken to be equal to unity, and the fluid is subjected to potential external forces. In 2D, the condition of incompressibility $\nabla \cdot \bar{v} = 0$ can be satisfied exactly by expressing the velocity vector $\bar{v} = (u, v)$ in terms of the stream function ψ according to

$$u = \frac{\partial \psi}{\partial y}, \quad v = -\frac{\partial \psi}{\partial x}. \tag{1.30}$$

A new form is based on the following observation. The substitution of equation (1.30) into equation (1.27) yields

$$\frac{\partial}{\partial y}\left(\psi_t - \psi_x\psi_y - \nu\Delta\psi\right) + \frac{\partial}{\partial x}\left(p + \psi_y^2\right) = 0, \tag{1.31}$$

where

$$\Delta \stackrel{\text{def}}{=} \frac{\partial^2}{\partial x^2} + \frac{\partial^2}{\partial y^2}.$$

Therefore, there is a function Φ which satisfies the relations

$$p = -\psi_y^2 + \Phi_y, \tag{1.32}$$

$$\psi_t - \psi_x\psi_y + \Phi_x = \nu\Delta\psi. \tag{1.33}$$

Differentiating equation (1.32) and equation (1.33) with respect to y and x, respectively, and substituting the resulting expressions into (1.28), where u and v are expressed in terms of ψ obtaining

$$\Delta\Phi = 2\psi_y\Delta\psi. \tag{1.34}$$

The system (1.33)–(1.34) is the new form of the NSEs in the 2D plane flow.

1.7 The boundary conditions for the Navier-Stokes equations

1.7.1 The boundary conditions for a viscous incompressible fluid motion

In general case, the statement of the problem for equations (1.1) and (1.2) is made complete by the specification of suitable boundary and initial conditions. A typical boundary condition consists in prescribing the value of the velocity $\bar{v}$ on the boundary

$$\bar{v}\big|_S = \bar{b}(\bar{x}_S, t), \quad t \in [0, T], \tag{1.35}$$

where S is the boundary of the domain V occupied by the fluid, $\bar{b}$ is given function and $\bar{x}_S \in S$. When the boundary is a solid wall in contact with the fluid, the velocity boundary value $\bar{b}$ is equal to the velocity of the wall. The condition on the tangential components of velocity is known as the no-slip condition. Quartapelle (1993, PP.3) shows no boundary condition for pressure.

The initial condition consists in the specification of the velocity field $\bar{v}_0$ at the initial time, $t = 0$, namely,

$$\bar{v}\big|_{t=0} = \bar{v}_0(\bar{x}). \tag{1.36}$$

The boundary velocity $\bar{b}$ must satisfy, for all $t \geq 0$, the global condition

$$\oint \bar{n} \cdot \bar{b}\, ds = 0, \tag{1.37}$$

which follows from integrating the continuity equation (1.2) over V and using the divergent theorem. The vector $\bar{n}$ denotes the outward unit normal to the boundary S. The initial velocity field $\bar{v}_0$ is assumed to be solenoidal, i.e.,

$$\nabla \cdot \bar{v}_0 = 0. \tag{1.38}$$

Finally, the boundary and initial data $\bar{b}$ and $\bar{v}_0$ are assumed to satisfy the following compatibility condition

$$\bar{n} \cdot \bar{b}\big|_{t=0} = \bar{n} \cdot \bar{v}_0\big|_{S}, \tag{1.39}$$

where, of course, $\bar{n} \cdot \bar{b}\, (\bar{x}_S, t)$ is taken to be a continuous function of time as $t \to 0^+$. Condition (1.39) is absent in the steady-state version of the problem. To determine the pressure uniquely additional requirement is needed

$$p(\bar{x}_0, t), \quad \forall\, t \in [0, T], \quad \bar{x}_0 \in V.$$

1.7.2 The boundary conditions for vorticity-stream function equations in 2D

The boundary conditions supplementing the vorticity-stream function formulation of the NSEs (1.4) and (1.5) for the 2D flow are deduced by separating the normal and tangential components of the velocity boundary condition $\bar{v}\big|_{S} = \bar{b}(\bar{x}_S, t)$. Here S represents the boundary of the 2D domain V. Let $\bar{n}$ denotes the outward unit

vector normal to the boundary S and $\bar{\tau}$ is the unit vector tangential to S with anti-clockwise orientation. Finally, let s be the curvilinear coordinate along the boundary S. Then, the boundary condition for the normal component is

$$\bar{n} \cdot \nabla \psi \times \bar{k} \big|_S = \bar{k} \times \bar{n} \cdot \nabla \psi = \bar{\tau} \cdot \bigtriangledown \psi = \frac{\partial \psi}{\partial s} \big|_S = \bar{n} \cdot \bar{b}, \tag{1.40}$$

and for the tangential component

$$\bar{\tau} \cdot \nabla \psi \times \bar{k} \big|_S = \bar{k} \times \bar{\tau} \cdot \nabla \psi = -\bar{n} \cdot \bigtriangledown \psi = \frac{\partial \psi}{\partial n} \big|_S = \bar{\tau} \cdot \bar{b}. \tag{1.41}$$

The boundary condition (1.40), after integrating its right-hand side, provides a Dirichlet condition for ψ. By virtue of the global condition $\oint_S \bar{n} \cdot \bar{b} \, ds = 0$, such as integration defines a single-valued function up to an arbitrary additive function of time, namely,

$$a(s,t) = \int_{s_1}^{s} \bar{n}(s') \cdot \bar{b}(s',t) \, ds' + A(t),$$

where s_1 is the coordinate of any fixed point of S and s' is a dummy variable of integration. To simplify the expression of the boundary conditions for ψ, the term $A(t)$ is dropped from Dirichlet condition and the notation

$$b(s,t) = -\bar{\tau} \cdot \bar{b}(s,t),$$

is introduced so that the two conditions can be written as follows

$$\psi \big|_S = a, \quad \frac{\partial \psi}{\partial n} \big|_S = b, \tag{1.42}$$

where $a = \int_{s_1}^{s} \bar{n} \cdot \bar{b} \, ds'$ and $b = -\bar{\tau} \cdot \bar{b}$. The initial data $\bar{v}_0$ and the boundary data $a(s,t)$ are assumed to satisfy the conditions

$$\nabla \cdot \bar{v}_0 = 0, \quad \frac{\partial \, a(s,0)}{\partial s} = \bar{n} \cdot \bar{v}_0 \big|_S. \tag{1.43}$$

The initial velocity field $\bar{v}_0$ provides the following initial condition for the vorticity

$$\omega \big|_{t=0} = \nabla \times (\bar{v} \big|_{t=0}) \cdot \bar{k} = \nabla \times \bar{v}_0 \cdot \bar{k}. \tag{1.44}$$

In formulation (1.6), the specification of the Dirichret and Neumann boundary conditions (1.42) poses no difficulty because they are both required to supplement the fourth-order elliptic operator. It needs to note that no boundary condition for the vorticity available. This is one of the main difficulty in an approximate solution of the NSEs in terms of the vorticity-stream function formulation.

1.7.3 The boundary conditions for the Navier-Stokes equations in Aristov-Pukhnachev's form

The boundary conditions for the system (1.24), (1.25), and (1.26) are two boundary conditions for the stream function and no-slip boundary condition for the angular momentum $J = rv$. In terms of the functions ψ and J, these conditions are (compare with boundary conditions (1.42))

$$\frac{\partial \psi}{\partial n}\Big|_S = b, \tag{1.45}$$

$$\psi\big|_S = a, \qquad J\big|_S = c, \tag{1.46}$$

where c is the azimuthal velocity component of the boundary S. To complete the formulation of the problem for the system (1.24)–(1.25), it is necessary to specify the initial conditions

$$\psi = \psi_0(r, z), \quad (r, z) \in \bar{\Omega}, \quad t = 0, \tag{1.47}$$

$$J = J_0(r, z), \quad (r, z) \in \bar{\Omega}, \quad t = 0. \tag{1.48}$$

It is no boundary condition for the function Φ. A difficulty in solving the system of equations for ψ, J, and Φ supplemented by the boundary conditions above is that two boundary conditions are specified for ψ while none is available for Φ. This difficulty is similar to the vorticity-stream function equations in 2D. To overcome the difficulty caused by the absence of boundary condition for Φ. Aristov and Puknachev (2004) transform equation (1.26) into the fourth-order equation by applying the operator

$\mathbf{E}$ and using boundary condition $\dfrac{\partial \psi}{\partial n} = 0$. In this case the boundary conditions for ψ, J, and Φ are uncoupled and iterative solution procedures can be used to find an approximate solution. The weak point of such approach is the necessity to solve the Neumann problem for the bi-harmonic equation. An uncoupled solution of this problem can be found up to an arbitrary function which satisfy $\mathbf{E}\tilde{\Phi} = 0$.

Now, the results of Aristov and Pukhnachev (2004) are reproduced how to get of a weakly coupled system with an uncouple boundary condition for the functions ψ, J, and Φ.

Let $\mathbb{R}^+$ be the $r > 0$ half-plane of the (r, z) plane, Σ be the bounded domain in $\mathbb{R}^+$, $\partial\Sigma$ be the boundary of Σ, $Q_T = \Sigma \times (0, T)$, and $S_T = \partial\Sigma \times (0, T)$. Assume the closure $\overline{\Sigma}$ of domain Σ does not contain points lying on the $z-$axis.

Applying the operator $\mathbf{E}$ to equation (1.26) gives the fourth-order equation

$$\mathbf{E}^2\Phi = \mathbf{E}\left[\frac{1}{r^2}\left(J^2 + \psi_z^2\right) + \frac{2}{r}\psi_r\,\mathbf{E}\psi\right]. \tag{1.49}$$

One boundary condition for equation (1.49) follows immediately from equations (1.26), (1.45), and (1.46) with $a \equiv b \equiv 0$.

$$\mathbf{E}\Phi = 0, \quad (r, z, t) \in S_T. \tag{1.50}$$

Applying the operator $\dfrac{\partial}{\partial n}$ to equation (1.26) and using equations (1.45) and (1.46) with $a \equiv 0$ and $b \equiv 0$ yields the second condition

$$\frac{\partial\,\mathbf{E}\Phi}{\partial n} = \frac{2}{r}\frac{\partial\,\Phi_r}{\partial n}\mathbf{E}\psi, \ (r, z, t) \in S_T. \tag{1.51}$$

The problem of determining ψ, J, and Φ is finally formulated as follows: to find those solutions of the system of equations (1.24), (1.25), and (1.49) which satisfy conditions (1.45)–(1.48), (1.50), and (1.51).

1.8 Previous research

This section provides the short review of the problem which becomes the benchmark problem to validate different numerical algorithms in the cases of the 2D incompressible NSEs (plane and axisymmetric flows).

In recent year, many researchers (i.e., Spotz, 1998; Christov and Tang, 2006; Tang and Christov, 2006; Zhang, 2006; Kalita, 2007) have studied the accuracy and performance of the numerical algorithm for the NSEs in 2D. The finite-difference method is one of the most common discreatization technique in computational fluid dynamics. The fourth-order equation appears in the 2D NSEs in terms of the stream function (e.g., Quartapelle, 1993). Many methods for the numerical solution of this equation have been proposed, see for example Christov and Ridha (1994), Mohanty (2003), and Christov and Tang (2006). The splitting method is applied for solving the bi-harmonic boundary-value problems by Christov and Ridha (1994). The implicit time splitting method for the fourth-order parabolic equation is applied to the numerical solution and results are obtained by Christov, Pontes, Walgraef, and Velared (1997).

The lid-driven cavity problem, in general, have been a common experimental approach used to test or improve numerical schemes. The problem geometry is simple and 2D. Many researchers have long been studied this flow ranging from the Stokes flow to higher Reynolds number flow with continued improving accuracy. However, there is no general opinion about existence of steady require for the high Reynolds number. Almost everybody except that is the case $Re < 5000$ steady require is possible.

In any numerical method, a compromise is needed between accuracy of results and the computational effort spent in acquiring the results. Resolving all the quantities of a complex flow proves to be very costly. Moreover, employing highly

turbulence models to a complex phenomena could give inaccurate simulation results. With the increasing interest in time periodic, the solution become chaotic. Bruneau and Saad (2006) compute some periodic solution at $Re = 10000$. Further, Garcia (2007) studied the numerical solution in the 2D high Reynolds number in a cavity flow. Time periodic experiments were performed on different case.

The Taylor-Couette flow provides opportunities for detailed comparison between the results of experimental and numerical investigation. The Taylor-Couette flow is the flow between two rotating concentric cylinders. The concentric cylinder shares the same center, axis or origin with one inside the other. It is simplest example of an axisymmetric flow can be find in any handbook of fluid mechanics (e.g., Batchelor, 2000; Marshall, 2001). This system, first studied at Cambridge University by Geoffery Ingram Taylor in the 1920s. Taylor's pioneering work (1923), nearly all of the research has been related to the stability problem of a viscous liquid between the rotating inner cylinder and the stationary outer one. The assumption that cylinders had infinite axial length and the gap between them was narrow is used to calculate. In recent years, many researchers have investigated the problem of the flow between two rotating concentric cylinders. The phenomenon of the axisymmetric incompressible flow which is driven by a rotating bottom lid and sides of cylindrical container has been extensively studied both numerically (e.g., Lopez and Perry, 1992a; Lopez, 1994; Inamuro, Yamaguchi, and Ogino, 1997; Lopez and Shen, 1998; Iwatsu, 2004; Lopez, Marques, and Shen, 2004; Barbosa and Daube, 2005) and experimentally (e.g., Lopez and Perry, 1992b; Pereira and Sousa, 1997; Stevens, Lopez, and Cantwell, 1999). The results of the experimental and numerical investigations into the Taylor-Couette flow in a very short annulus (gap length to width ranging from 0.3 to 1.4) are detailed by Pfister, Schmidt, Cliffe, and Mullin (1988). Laser-dropper-velocity is used to obtain quantitative information on the bifurcation set experimentally, and novel flow phe-

nomena are uncovered. The experimental results are compared with numerical results which use numerical bifurcation techniques applied to a finite-element discretization of the NSEs. Mullin and Blohm (2001) have observed bifurcation phenomena in the flow between a rotating inner cylinder and a fixed outer cylinder. Asymmetric boundary conditions are used in the problem which has the bottom end wall rotated with the inner cylinder while the other remains stationary. The focus of that study is on the steady cellular flows consist of one or three vortices in the aspect ratio range. Furthermore, the behavior of bifurcation between asymmetric one cell and symmetric two cell flows have been observed by Mullin, Toya, and Tavener (2002), and Schulz, Pfister, and Tavener (2003). Mullin and Blohm (2001) have investigated the flow between one stationary end plate and the other attached to the rotating inner cylinder. In this sense, the rotation of end cell can be changed. The problem of flow with independently rotating end plates is studied in detail by Abshagen et al. (2004). The exchange between two states on two-cell flows is founded. Further, the effect of outer cylinder rotation on the Taylor-Couette flow at small aspect ratio is pointed out by Schulz, Pfister, and Tavener (2003).

1.9   Objectives and overview

In the present research, the performance of numerical methods for the 2D incompressible NSEs in terms of the stream function is studied. In order to study properties of the explicit, implicit, and modification of explicit schemes (internal iteration scheme), a comparative analysis of three numerical methods is performed. The simplest method is an explicit and additional difficulties arise when an implicit method (operator splitting method) is used. The explicit method has motivated but it is not difficult in the context of a computational code. The lid-driven cavity is used as the benchmark problem. Moreover, this dissertation develops and studies a

numerical algorithm for the NSEs in Aristov-Pukhnachev 's formulation for 2D plane and axisymmetric flows. Finite-difference algorithms are validated on the Taylor-Couette and lid-driven cavity flows.

The main objectives of the dissertation are:

(i) To analyze three numerical methods (explicit method, operator splitting method, and internal iteration method) for approximate solutions of the NSEs in terms of the stream function on an example of the lid-driven cavity problem

(ii) To validate and compare results of three finite-difference methods with available data of numerical simulations and laboratory experiments for wide range of the Reynolds number up to 10000

(iii) To derive a numerical method for approximate solutions of the NSEs in new variables proposed by Aristov and Pukhnachev (2004)

(iv) To validate and compare results of numerical solutions using the Taylor-Couette flow for which there are a lot of data of numerical simulations and laboratory experiments

At the end of this introduction, the following short overview should procure an impression of what will be detailed with in the respective chapters of this dissertation. **Chapter II** explains the detail of performance of three finite-difference schemes. After characterizing the methods, the given grid size and the computational effort will be the focus of this chapter. The solution strategies for the higher Reynolds number ($Re > 5000$) are particularly emphasized by the internal iteration method. In **Chapter III**, a finite-differences technique is developed for the implementation of Aristov-Pukhnachev's form of the Navier-Stokes equations for the modelling axisymmetric viscous incompressible fluid flows.

Chapter IV contains a brief insight into some issues of the structure of a new auxiliary function introduced in Aristov and Pukhnachev (2004). This function is reconstructed from the approximation solution of the NSEs in the stream function and angular momentum form by a method of an internal iteration developed in Chapter II.

In **Chapter V**, a novel finite difference scheme for the prediction of the 2D plane viscous incompressible flow is developed. The lid-driven cavity flow is used to validate numerical algorithm. A summary of this work and a recommended future work are provided in **Chapter VI**.

1.10   References

Abshagen, J., Cliffe, K.A., Langenberg, J., Mullin, T., Pfister, G., and Tavener, S.J. (2004). Taylor-Couette flow with independently rotating end plates. **Theoretical and Computational Fluid Dynamics** 18:129–136.

Aristov, S.N., and Pukhnachev, V.V. (2004). On the equations of axisymmetric motion of a viscous incompressible. **Doklady Physics** 49(2):112–115.

Barbosa, E., and Daube, O. (2005). A finitem difference method for 3D incompressible flows in cylindrical coordinates. **Computers & Fluids** Elsevier Ltd.

Batchelor, G.K. (2000). **An Introduction to Fluid Dynamics**. Cambridge Mathematical Library.

Bruneau, C.H., and Saad, M. (2006). The 2D lid-driven cavity problem revisited. **Computers & Fluids** 35:326–348.

Christov, C.I., Pontes, J., Walgraef, D., and Velared, M.G. (1997). Implicit time

splitting for fourth-order parabolic equations. **Computer Methods in Applied Mechanics and Engineering** 148:209–224.

Christov, C.I., and Ridha, A. (1994). Splitting scheme for iIterative solution of bi-harmonic equation application to 2D Navier-Stokes problems. **Advances in Numerical Methods & Applications Sofia** 341–349.

Christov, C.I., and Tang, X.H. (2006). An operator splitting scheme for the stream-function formulation of unsteady Navier-Stokes equations. **International Journal for Numerical Methods in Fluids** 53(3):417–442.

Garcia, S. (2007). The lid-driven square cavity flow: from stationary to time periodic and chaotic. **Communications in Computational Physics** 2(5):900–932.

Inamuro, T., Yamaguchi, A., and Ogino, F. (1997). Fluid flow in a rotating cylindrical container with a rotating disk at the fluid surface. **Fluid Dynamics Research** 21:417–430.

Iwatsu, R. (2004). Flow Pattern and Heat Transfer of Swirling Flows in Cylindrical Container with Rotating Top and Stable Temperature Gradient. **International Journal of Heat and Mass Transfer** 47:2755–2767.

Kalita, J.C. (2007). Effects of clusterring on the simulation of incompressible viscous flows. **Engineering Applications of Computational Fluid Mechanics** 1(1):36–48.

Levit, C. (1989). Parallel solution of pentadiagonal systems using generalized odd-even elimination. **ACM.** 11:333–336.

Lopez, J.M. (1994). On the bifurcation structure of axisymmetric vortex breakdown in a constricted pipe. **Physics of Fluids** 6(11):3683–3693.

Lopez, J.M., Marques, F., and Shen, J. (2004). Complex dynamics in a short annular container with rotating bottom and inner cylinder. **Journal of Fluid Mechanics** 501:327–354.

Lopez, J.M., and Perry, A.D. (1992a). Axisymmetric vortex breakdown, Part 3 onset of periodic flow and chaotic advection. **Journal of Fluid Mechanics**, 234:449–471.

Lopez, J.M., and Perry, A.D. (1992b). Periodic axisymmetric vortex breakdown in a cylinder with a rotating end wall. **Physics of Fluids A** 4:1871.

Lopez, J.M., and Shen, J. (1998). An efficient spectral-projection method for the Navier-Stokes equations in cylindrical geometries. **Journal of Computational Physics** 139:308–326.

Marshall, J.H. (2001). **Inviscid Incompressible Flow**. USA, Wiley Inter-Science.

Mohanty, R.K. (2003). An accurate three spatial grid-point discreatization of for the numerical solution of one-space dimentional unsteady quasi-linear biharmonic problem of second kind. **Applied Mathematics and Computation** 140:1–14.

Mullin, T., and Blohm, C. (2001). Bifurcation phenomena in a Taylor-Couette flow with asymmetric boundary conditions. **Physics of Fluids** 13(1):136–140.

Mullin, T., Toya, Y., and Tavener, S.J. (2002). Symmetry breaking and multiplicity of states in small aspect ratio Taylor-Couette flow. **Physics of Fluids** 14(8):2778–2787.

Pereira, J.C.F., and Sousa, A.M.M. (1997). Steady and transient topologies of confined vortex breakdown generated by a rotating cone. **Optical Diagnostics Engineering** 2(2):61–70.

Pfister, G., Schmidt, H., Cliffe, K.A., and Mullin, T. (1988). Bifurcation phenomena in Taylor-Couette flow in a very short annulus. **Journal of Fluid Mechanics** 191:1–18.

Pukhnachev, V.V. (2004). Integrals of motion of an incompressible fluid occupying the entire space. **Journal of Applied Mechanics and Technical Physics** 45(2):167–171.

Quartapelle, L. (1993). **Numerical Solution of the Incompressible Navier-Stokes Equations**. Basel, Switzerland: Birkhauser Verlag.

Schulz, A., Pfister, A., and Tavener, S.J. (2003). The effect of outer cylinder rotation on Taylor-Couette flow at small aspect ratio. **Physics of Fluids** 15(2):417–425.

Spotz, W.F. (1998). Accuracy and performance of numerical wall boundary conditions for steady, 2D, incompressible streamfunction vorticity. **International Journal for Numerical Methods in Fluids** 28:737–757.

Stevens, J.L., Lopez, J.M., and Cantwell, B.M. (1999). Oscillatory flow state in an enclosed cylinder with a rotating endwall. **Journal of Fluid Mechanics** 389:101–118.

Tang, X.H., and Christov, C.I. (2006). An operator splitting scheme for biharmonic equation with accelerated convergence. **Large Scale Scientific Computatig**. Lirkov I., Margenov S., and Wasniewski J.(Eds.). Lecture notes in computer sciences 3743: Springer Verlag 380–387.

Taylor, G.I. (1923). Stability of a viscous liquid contained between two rotating cylinders. **Philosophical Transactions of the Royal Society A** 223:289–343.

Zhang, K.K.Q., Minkowycz, W.J., and Mashayek, F. (2006). Exact factorization technique for numerical simulations of incompressible Navier-Stokes flows. **International Journal of Heat and Mass Transfer** 29:535–545.

CHAPTER II

COMPARISON OF THREE FINITE

DIFFERENCE SCHEMES FOR STREAM

FUNCTION FORMULATION

The performance of three finite-difference schemes for the approximate solution of the 2D incompressible NSEs in the stream function representation are examined. In one scheme, explicit approximation to nonlinear terms is used. The second one is an operator splitting scheme (i.e., Christov and Tang, 2006). The method of internal iteration is used to approximate nonlinear convective terms in the third finite-difference scheme. The schemes are compared on the standard benchmark problem of the 2D lid-driven cavity flow for the Reynolds number up to 10000. The result of numerical experiments show the finite-difference scheme with internal iteration on nonlinearity is more efficient for the high Reynolds number.

2.1 Introduction

Because of the nonlinearity of the NSEs and the implicit nature of the continuity condition, the practical approximation of any scheme can turn out to be rather different from the theoretical estimates. This is especially true for very high Reynolds numbers. Different schemes perform better in different situations. No single scheme can be best in all distance. That is why in the last several years new schemes have appeared on ever increasing pace (see for example, Kim and Moin, 1985; Karnaidakis, Israeli, and Orszag, 1991; Rosenfeld, Kwak, and Vinokur, 1991; Christov and Mari-

nova, 2001).

The system of incompressible NSEs describes the motion of incompressible viscous liquid.The coupling of NSEs comes through the nonlinear terms, the continuity equation, and the boundary conditions. In the numerical solution of the incompressible NSEs, a serious difficulty arises from the determination of the pressure field. In fact, the continuity equation represents a constraint on the velocity field to be satisfied. At the time, the unknown pressure function provides the degree of freedom needed to accommodate such a constraint. Thus the pressure field is not calculated by an explicit time-advancement procedure but requires instead an implicit determination. This means that the incompressible NSEs are not a system of Cauchy-Kovalevskaya type (Temam, 1977) and this aspect can be considered to be their most distinctive feature. Quite naturally, for the implicit pressure function no boundary conditions have to be prescribed at the rigid boundaries. This is still another formidable obstacle on the way of constructing fully implicit schemes. In 2D, the pressure can be eliminated from the equations by means of stream function ψ and vorticity function $\omega = -\nabla^2 \psi$ (see, $\psi - \omega$ formulation in Chapter I) but then an explicit boundary condition for vorticity is missing.

The implicit nature of the pressure function (or the vorticity function) requires a special care for stability of algorithms since the explicit decoupling of the boundary conditions (descendant of the so-called Thom's condition) imposes significant limitations on the time increment (i.e., Mallison and De Vahl David, 1973; Smagulov and Christov, 1980; Quartapelle, 1981; Vabishchevich, 1984; Christov and Ridha, 1994, 1995; Iliev and Makarov, 1995) for stability.

The simplest way to avoid difficulty by the lack of boundary condition for the vorticity is not to use a vorticity function at all. It is called 'stream function formulation', the simultaneous specification of the Dirichlet and Neumann boundary

conditions create no difficulty, because the correct posing of the boundary value problem for the fourth-order elliptic operator ∇^4 involves two boundary conditions.

The main purpose of this chapter is to validate an efficiency and accuracy of three finite-difference schemes for the NSEs in terms of stream function. The content of this chapter is organized as follows. Next section contains the governing equations. After that the briefed description of three numerical algorithms are given in Section 2.3. Results and discussions about performance of three schemes are presented in Section 2.4, where a detailed comparison with available numerical data is made.

2.2 Governing equation

The standard benchmark problem for testing the 2D plane NSEs is the driven cavity flow. The fluid contained inside a squared cavity is set into motion by the upper wall which is sliding at constant velocity from left to right. The motion of an incompressible viscous fluid is governed by the NSEs (1.6).

The domain is the unit square cavity, and the viscous incompressible flow is governed by the 2D time-dependent incompressible NSEs and driven by the upper wall as seen in Figure 2.1. An unexpected balance of viscous and pressure forces makes the fluid turn into the square cavity. The properties of these forces depend upon the Reynolds number, a hierarchy of eddies develops, the large clockwise-rotating primary, whose location occurs toward the geometric center of the square cavity, and several small eddies: the counterclockwise-rotating secondary eddies, the clockwise-rotating tertiary eddies, whose locations occur at the three relevant corners of the square cavity: bottom left, bottom right, and top left.

Let L be the characteristic length scale associated with the cavity geometry and U be the characteristic velocity scale associated with the moving boundary. The
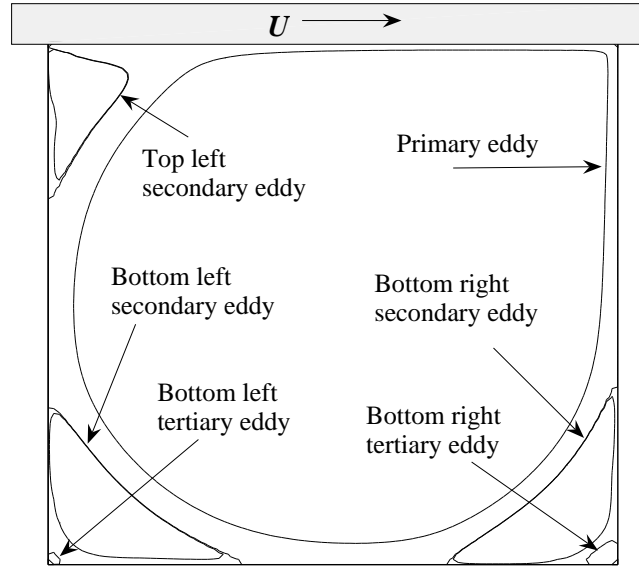
Figure 2.1 Sketch of the basic features in the 2D flow problem.

following dimensionless quantities are introduced: time, $t = \dfrac{t^*\nu}{L^2}$; space, $x = \dfrac{x^*}{L}$; and velocity, $v = \dfrac{v^*}{U}$. The NSEs for a viscous incompressible flow in closed 2D domain Ω with a piecewise smooth boundary $\partial\Omega$ in terms of the stream function ψ are

$$\frac{\partial \Delta \psi}{\partial t} + Re \left(\frac{\partial \psi}{\partial y} \frac{\partial \Delta \psi}{\partial x} - \frac{\partial \psi}{\partial x} \frac{\partial \Delta \psi}{\partial y} \right) - \Delta^2 \psi = 0, \ (x, y) \in \Omega. \tag{2.1}$$

Boundary and initial conditions are the following

$$\psi = 0, \ \frac{\partial \psi}{\partial n} = b(x, y), \ (x, y) \in \partial\Omega, \tag{2.2}$$

$$\psi(x, y, 0) = \psi^0(x, y), \ (x, y) \in \Omega, \tag{2.3}$$

where n is the vector normal to domain boundary, the Reynolds number is defined as $Re = UL/\nu$, where ν is the kinematic viscosity.

2.3 Numerical methods

Three numerical algorithms for a driven cavity flow are represented. The lid-driven flow occupies the region (the cavity)

$$\Omega = \big\{0 \leqslant x \leqslant 1, 0 \leqslant y \leqslant 1\big\}.$$

The flow is induced by the sliding motion of the top wall $(y = 1)$ from left to right. The no-slip boundary conditions take the following forms

$$\psi = \frac{\partial \psi}{\partial x} = 0 \quad \text{for} \quad x = 0 \quad \text{and} \quad x = 1,$$

$$\psi = \frac{\partial \psi}{\partial y} = 0 \quad \text{for} \quad y = 0, \tag{2.4}$$

$$\psi = 0, \frac{\partial \psi}{\partial y} = 1 \quad \text{for} \quad y = 1.$$

For the sake of simplicity, a uniform grid with h_x and h_y spacing in $x-$ and $y-$direction, respectively, $h_x = \dfrac{1}{N_x - 1}$, $h_y = \dfrac{1}{N_y - 1}$ and $(x_i, y_j) = \big((i - 1.5)h_x, (j - 1.5)h_y\big)$ for $i = 1, \ldots, N_x$ and $j = 1, \ldots, N_y$ is assumed. The mesh is
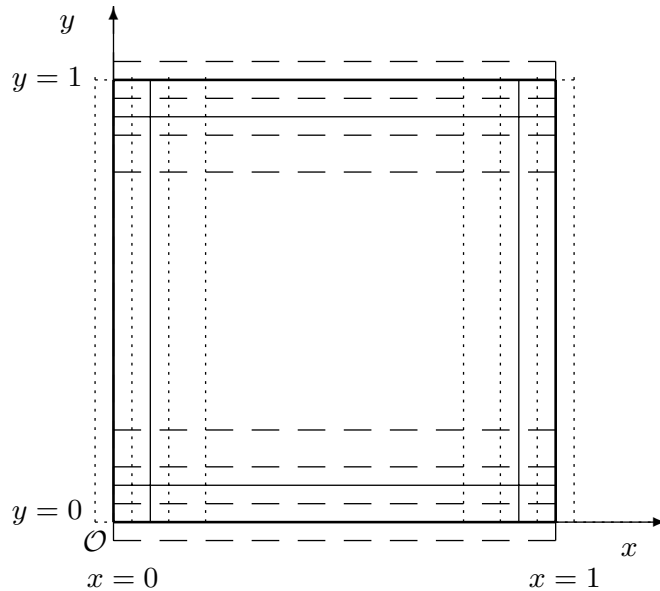
Figure 2.2 Sketch of grid for lid-driven problem.

staggered in $x-$direction on $0.5h_x$ and in $y-$direction on $0.5h_y$ with respect to do-

main boundaries $x = 0$, $x = 1$, $y = 0$, and $y = 1$. Figure 2.2 shows the sketch of grid. For all three finite-difference schemes considered below the boundary conditions are approximated on two-point stencils with the second-order of approximation as follows

$$\psi_{2,j}^n - \psi_{1,j}^n = 0; \qquad \psi_{1,j}^n + \psi_{2,j}^n = 0 \quad \Rightarrow \quad \psi_{1,j}^n = \psi_{2,j}^n = 0, \qquad (2.5)$$

$$\psi_{N_x,j}^n - \psi_{N_x-1,j}^n = 0; \quad \psi_{N_x-1,j}^n + \psi_{N_x,j}^n = 0 \quad \Rightarrow \quad \psi_{N_x-1,j}^n = \psi_{N_x,j}^n = 0, \qquad (2.6)$$

$$\psi_{i,2}^n - \psi_{i,1}^n = 0; \qquad \psi_{i,1}^n + \psi_{i,2}^n = 0 \quad \Rightarrow \quad \psi_{i,1}^n = \psi_{i,2}^n = 0, \qquad (2.7)$$

$$\psi_{i,N_y}^n - \psi_{i,N_y-1}^n = h_y; \quad \psi_{i,N_y-1}^n + \psi_{i,N_y}^n = 0 \quad \Rightarrow \quad \psi_{i,N_y}^n = -\psi_{i,N_y-1}^n = \frac{h_y}{2}, \quad (2.8)$$

where $\psi_{i,j}^n = \psi[x_i, y_j, t^n = (n-1)\tau]$, $i = 1, \ldots, N_x$, $j = 1, \ldots, N_y$, and $n = 1, 2, \ldots$ Here τ is the time increment.

2.3.1 Explicit scheme in nonlinear terms

The simplest method is an explicit in which all nonlinear terms are evaluated using known values at t^n. The Laplace operator is approximated by the Crank-Nicolson scheme. Thus, one has a linear system to calculate the new value of the unknown at each node. It is clear that each term in equation (2.1) can be approximated using the central-difference operators for all derivatives.

The explicit finite-difference scheme for equation (2.1) is

$$\frac{\left(\Delta_h \psi^{n+1}\right)_{i,j} - \left(\Delta_h \psi^n\right)_{i,j}}{\tau} + Re \Bigg\{ \left(\Lambda_y \psi^n\right)_{i,j} \left[\frac{\left(\Delta_h \psi^n\right)_{i+1,j} - \left(\Delta_h \psi^n\right)_{i-1,j}}{2h_x} \right]$$

$$- \left(\Lambda_x \psi^n\right)_{i,j} \left[\frac{\left(\Delta_h \psi^n\right)_{i,j+1} - \left(\Delta_h \psi^n\right)_{i,j-1}}{2h_y} \right] \Bigg\} - \frac{1}{2} \left(\Delta_h^2 \psi^{n+1} + \Delta_h^2 \psi^n \right)_{i,j} = 0 \quad (2.9)$$

where $\Delta_h = \Lambda_{x^2} + \Lambda_{y^2}$ and $\Delta_h^2 = \Lambda_{x^4} + 2\Lambda_{x^2 y^2} + \Lambda_{y^4}$. The difference formulas to be

used are given by

$$(\Lambda_x \psi)_{i,j} = \frac{\psi_{i+1,j} - \psi_{i-1,j}}{2h_x};$$

$$(\Lambda_y \psi)_{i,j} = \frac{\psi_{i,j+1} - \psi_{i,j-1}}{2h_y};$$

$$(\Lambda_{x^2} \psi)_{i,j} = \frac{\psi_{i+1,j} - 2\psi_{i,j} + \psi_{i-1,j}}{h_x^2};$$

$$(\Lambda_{y^2} \psi)_{i,j} = \frac{\psi_{i,j+1} - 2\psi_{i,j} + \psi_{i,j-1}}{h_y^2};$$

$$(\Lambda_{x^3} \psi)_{i,j} = \frac{\psi_{i+2,j} - 2\psi_{i+1,j} + 2\psi_{i-1,j} - \psi_{i-2,j}}{2h_x^3};$$

$$(\Lambda_{y^3} \psi)_{i,j} = \frac{\psi_{i,j+2} - 2\psi_{i,j+1} + 2\psi_{i,j-1} - \psi_{i,j-2}}{2h_y^3};$$

$$(\Lambda_{x^2 y} \psi)_{i,j} = \frac{1}{2h_y h_x^2} \left\{ (\psi_{i+1,j+1} - \psi_{i+1,j-1}) - 2(\psi_{i,j+1} - \psi_{i,j-1}) \right.$$
$$\left. + (\psi_{i-1,j+1} - \psi_{i-1,j-1}) \right\};$$

$$(\Lambda_{x y^2} \psi)_{i,j} = \frac{1}{2h_x h_y^2} \left\{ (\psi_{i+1,j+1} - \psi_{i-1,j+1}) - 2(\psi_{i+1,j} - \psi_{i-1,j}) \right.$$
$$\left. + (\psi_{i+1,j-1} - \psi_{i-1,j-1}) \right\};$$

$$(\Lambda_{x^4} \psi)_{i,j} = \frac{\psi_{i+2,j} - 4\psi_{i+1,j} + 6\psi_{i,j} - 4\psi_{i-1,j} + \psi_{i-2,j}}{h_x^4};$$

$$(\Lambda_{y^4} \psi)_{ij} = \frac{\psi_{i,j+2} - 4\psi_{i,j+1} + 6\psi_{i,j} - 4\psi_{i,j-1} + \psi_{i,j-2}}{h_y^4};$$

$$(\Lambda_{x^2 y^2} \psi)_{i,j} = \frac{1}{h_x^2 h_y^2} \left\{ (\psi_{i+1,j+1} - 2\psi_{i+1,j} + \psi_{i+1,j-1}) - 2(\psi_{i,j+1} - 2\psi_{i,j} + \psi_{i,j-1}) \right.$$
$$\left. + (\psi_{i-1,j+1} - 2\psi_{i-1,j} + \psi_{i-1,j-1}) \right\}.$$

The general sequence of the algorithm is as follows:

Step 1. Set the values of Re, τ, ε, N_x, N_y, and choose an initial guess $\psi_{i,j}^0 = 0$.

Step 2. Consider $\psi_{i,j}^n$ as known entities and calculate $\psi_{i,j}^{n+1}$ from the system of algebraic equation (2.9) added by boundary conditions (2.5)–(2.8). The direct method to solution of banded linear system (2.5)–(2.9) is used. The standard subroutines DGBSV and DGBSVX of LAPACK as well as subroutine devel-

oped by Christov (C.I. Christov, Gaussian elimination with pivoting for multi-diagonal systems, International Report (4), Publisher, University of Reading, 1994) are applied.

Step 3. If the following criterion is satisfied

$$\max_{i,j} \left| \psi_{i,j}^{n+1} - \psi_{i,j}^{n} \right| \leqslant \varepsilon \tag{2.10}$$

then the calculations are terminated. Otherwise the index of iterations is stepped up $n := n + 1$ and the computation is returned to Step 2.

2.3.2 Operator splitting scheme

The implicit methods are unconditionally stable and allow significantly larger time steps, with corresponding economy, as long as accuracy is maintained. To represent an operator splitting scheme, the results from Christov and Tang (2005) and Marchuk (1975) are needed to formulate.

Theorem 1: *Consider the advection operator $A = a(x,y)\dfrac{\partial}{\partial x} + b(x,y)\dfrac{\partial}{\partial y}$. If $a = a(x,y,t)$ and $b = b(x,y,t)$ satisfy the continuity equation $\dfrac{\partial a}{\partial x} + \dfrac{\partial b}{\partial y} = 0$ for $(x,y) \in D$ and $t \geqslant 0$, then with $t \geqslant 0$ fixed, $(A\chi, \chi) = 0$ for $\chi = \chi(x,y,t)$ defined on $\bar{D} \times t \geqslant 0$ if one of the following assumptions holds: (i) χ, as well as a and b, satisfy periodic boundary conditions on ∂D, with identical values on the opposite sides of rectangle. (ii) χ vanishes on ∂D or a and b are both zeros on ∂D for $t \geqslant 0$.*

Theorem 2: *If $\hat{\phi}$ is the grid function approximating χ, it is possible to decompose A into two operators with respect to different special derivatives and construct corresponding second-order difference operator A_x^h and A_y^h such that $A^h = A_x^h + A_y^h$ and*

$(A_x^h \hat{\phi}, \hat{\phi}) = (A_y^h \hat{\phi}, \hat{\phi}) = 0$, *where A_x^h and A_y^h are define as:*

$$(A_x^h \hat{\phi})_{i,j} = \frac{1}{2h_x}(a_{i+\frac{1}{2},j}\hat{\phi}_{i+1,j} - a_{i-\frac{1}{2},j}\hat{\phi}_{i-1,j}),$$

$$(A_y^h \hat{\phi})_{i,j} = \frac{1}{2h_y}(a_{i,j+\frac{1}{2}}\hat{\phi}_{i,j+1} - a_{i,j-\frac{1}{2}}\hat{\phi}_{i,j-1}),$$

(2.11)

where

$$a_{i+\frac{1}{2},j}^{n+\frac{1}{2}} = \frac{a_{i+1,j}^{n+\frac{1}{2}} + a_{i,j}^{n+\frac{1}{2}}}{2}, \quad a_{i-\frac{1}{2},j}^{n+\frac{1}{2}} = \frac{a_{i,j}^{n+\frac{1}{2}} + a_{i-1,j}^{n+\frac{1}{2}}}{2},$$

$$b_{i,j+\frac{1}{2}}^{n+\frac{1}{2}} = \frac{b_{i,j+1}^{n+\frac{1}{2}} + b_{i,j}^{n+\frac{1}{2}}}{2}, \quad b_{i,j-\frac{1}{2}}^{n+\frac{1}{2}} = \frac{b_{i,j}^{n+\frac{1}{2}} + b_{i,j-1}^{n+\frac{1}{2}}}{2}.$$

(2.12)

Let

$$P = -\frac{\partial \triangle \psi}{\partial x} \quad \text{and} \quad Q = \frac{\partial \triangle \psi}{\partial y}.$$

Then the convection terms can be rewritten as follows

$$A\psi = P\frac{\partial \psi}{\partial x} + Q\frac{\partial \psi}{\partial y}.$$

In order to improve the order of approximation in time, one can use the standard extrapolation formula

$$\hat{\psi}_{i,j}^{n+\frac{1}{2}} = \frac{3}{2}\psi_{i,j}^n - \frac{1}{2}\psi_{i,j}^{n-1} = \psi_{i,j}^{n+\frac{1}{2}} + O(\tau^2),$$

when evaluating the coefficients P and Q. Then

$$P_{i,j}^{n+\frac{1}{2}} = -\frac{1}{2h_y}\left[\left(\triangle_h \hat{\psi}^{n+\frac{1}{2}}\right)_{i,j+1} - \left(\triangle_h \hat{\psi}^{n+\frac{1}{2}}\right)_{i,j-1}\right]$$
$$= -\frac{\partial \triangle \psi}{\partial y}\left(ih_x, ih_y, \tau(n+\frac{1}{2})\right) + O(\tau^2 + h_x^2 + h_y^2), \quad (2.13)$$

for $i = 2, \ldots, N_x - 1$ and $j = 2, \ldots, N_y - 1$.

$$Q_{ij}^{n+\frac{1}{2}} = \frac{1}{2h_x}\left[\left(\triangle_h \hat{\psi}^{n+\frac{1}{2}}\right)_{i+1,j} - \left(\triangle_h \hat{\psi}^{n+\frac{1}{2}}\right)_{i-1,j}\right]$$
$$= \frac{\partial \triangle \psi}{\partial x}\left(ih_x, ih_y, \tau(n+\frac{1}{2})\right) + O(\tau^2 + h_x^2 + h_y^2), \quad (2.14)$$

for $i = 2, \ldots, N_x - 1$ and $j = 2, \ldots, N_y - 1$.

The difference operators $C_x^{n+\frac{1}{2}}$ and $C_y^{n+\frac{1}{2}}$ along direction of x and y respectively, acting upon ψ in the middle time stage $(n+\frac{1}{2})$ in order to have the second-order approximation with respect to time are constructed. For the approximation, the notation

$$\psi_{ij}^{n+\frac{1}{2}} = \frac{1}{2}\left(\psi_{ij}^n + \psi_{ij}^{n+1}\right) \tag{2.15}$$

is used and the value of the grid function ψ^{n+1} are considered unknown, but the values of ψ^n are treated as known. Since the stream function ψ vanishes on the boundary, one can use Theorem 1 and 2 to identify the advective operators as follows

$$\left(C_x^{n+\frac{1}{2}}\psi^{n+\frac{1}{2}}\right)_{i,j} = \frac{1}{2h_x}\left(P_{i+\frac{1}{2},j}^{n+\frac{1}{2}}\psi_{i+1,j}^{n+\frac{1}{2}} - P_{i-\frac{1}{2},j}^{n+\frac{1}{2}}\psi_{i-1,j}^{n+\frac{1}{2}}\right)$$

$$\left(C_y^{n+\frac{1}{2}}\psi^{n+\frac{1}{2}}\right)_{i,j} = \frac{1}{2h_y}\left(Q_{i,j+\frac{1}{2}}^{n+\frac{1}{2}}\psi_{i,j+1}^{n+\frac{1}{2}} - Q_{i,j-\frac{1}{2}}^{n+\frac{1}{2}}\psi_{i,j-1}^{n+\frac{1}{2}}\right) \tag{2.16}$$

for $i = 2, \ldots, N_x - 1$ and $j = 2, \ldots, N_y - 1$. Here P and Q are evaluated from the following finite-differences with second order accuracy $O(h_x^2 + h_y^2 + \tau^2)$, namely

$$P_{i+\frac{1}{2},j}^{n+\frac{1}{2}} = \frac{P_{i+1,j}^{n+\frac{1}{2}} + P_{i,j}^{n+\frac{1}{2}}}{2}, \quad P_{i-\frac{1}{2},j}^{n+\frac{1}{2}} = \frac{P_{i,j}^{n+\frac{1}{2}} + P_{i-1,j}^{n+\frac{1}{2}}}{2},$$

$$Q_{i,j+\frac{1}{2}}^{n+\frac{1}{2}} = \frac{Q_{i,j+1}^{n+\frac{1}{2}} + Q_{i,j}^{n+\frac{1}{2}}}{2}, \quad Q_{i,j-\frac{1}{2}}^{n+\frac{1}{2}} = \frac{Q_{i,j}^{n+\frac{1}{2}} + Q_{i,j-1}^{n+\frac{1}{2}}}{2}. \tag{2.17}$$

Using the definitions of the difference operators $C_x^{n+\frac{1}{2}}$ and $C_y^{n+\frac{1}{2}}$, the difference approximation for equation (2.1) based on the Crank-Nicolson scheme can be constructed in the following form

$$\frac{(\triangle_h(\psi^{n+1} - \psi^n))_{i,j}}{\tau} + \Bigg(\left[Re(C_x^{n+\frac{1}{2}} + C_y^{n+\frac{1}{2}}) - (\Lambda_{x^4} + \Lambda_{y^4} + 2\Lambda_{x^2}\Lambda_{x^2})\right]$$
$$\frac{\psi^{n+1} + \psi^n}{2}\Bigg)_{i,j} = 0 \quad (2.18)$$

where $i = 2, \ldots, N_x - 1$ and $j = 2, \ldots, N_y - 1$. In Christov and Tang (2005), the stability and convergence of this scheme have been demonstrated.

The general sequence of the algorithm is as follows:

Step 1. Set the values of Re, τ, ε, N_x, N_y, and choose an initial guess $\psi_{i,j}^0$.

Step 2. Calculate $\psi_{i,j}^1$ from the system of algebraic equation (2.9) added boundary conditions (2.5)–(2.8) by the direct method to solution banded linear system. The standard subroutines DGBSV and DGBSVX of LAPACK as well as subroutine developed by Christov (C.I. Christov, Gaussian elimination with pivoting for multi-diagonal systems, International Report (4), Publisher, University of Reading, 1994) are used.

Step 3. Consider $\psi_{i,j}^n$ as known entities and calculate $\psi_{i,j}^{n+1}$ from the system of algebraic equation (2.18) added boundary conditions (2.5)–(2.8) by direct method to solution banded linear system.

Step 4. If the following criterion is satisfied

$$\max_{i,j} \left| \psi_{i,j}^{n+1} - \psi_{i,j}^n \right| \leqslant \varepsilon$$

then the calculations are terminated. Otherwise the index of iterations is stepped up $n := n + 1$ and the algorithm is returned to Step 3.

2.3.3 Method with internal iteration in nonlinear terms

The general idea when treating the nonlinear terms is to represent it as an implicit approximation and then to linearize it and to conduct internal iterations. After the inner iterations converge one obtains, in fact, the solution for the new time stage. The explicit approximation of nonlinear terms accomplished severe requirement on time step. A single internal iteration on nonlinear terms induce sense of an implicit approximation and reduced very severe band on time step. To improve the stability properties of the explicit approximation of nonlinear terms, one requires a choice for the number of internal iterations.

This part present an improvement accuracy is achieved at small additional expense. The internal iteration scheme may be viewed as a modification of the explicit scheme (2.9). For the beginning, the internal iteration scheme used only three iterations. The reasoning behind the choices in this study was that a single iteration is equivalent to one step of the explicit scheme so, in order to take the economies of the explicit scheme, it is desirable to perform not too many iteration (three internal iterations are chose). The method with an internal iteration of nonlinear terms can be recast in the following form

$$
\frac{\left(\Delta_h \psi^{n+1,k}\right)_{i,j} - \left(\Delta_h \psi^n\right)_{i,j}}{\tau} + Re\Biggl\{ \left(\Lambda_y \tilde{\psi}\right)_{i,j} \left[\frac{\left(\Delta_h \tilde{\psi}\right)_{i+1,j} - \left(\Delta_h \tilde{\psi}\right)_{i-1,j}}{2h_x} \right]
$$
$$
- \left(\Lambda_x \tilde{\psi}\right)_{i,j} \left[\frac{\left(\Delta_h \tilde{\psi}\right)_{i,j+1} - \left(\Delta_h \tilde{\psi}\right)_{i,j-1}}{2h_y} \right] \Biggr\} - \frac{1}{2}\left(\Delta_h^2 \psi^{n+1,k} + \Delta_h^2 \psi^n\right)_{i,j} = 0 \quad (2.19)
$$

The general sequence of the algorithm is as follows:

Step 1. Set the values of Re, τ, ε, N_x, N_y and choose an initial guess $\psi_{i,j}^0 = 0$.

Step 2. Let

    (a) $\tilde{\psi}_{i,j} = \psi_{i,j}^n$ then calculate $\psi_{i,j}^{n+1,1}$ from the system of algebraic equation (2.19) added boundary conditions (2.5)–(2.8) by the direct method to solution banded linear system. The standard subroutines DGBSV and DGBSVX of LAPACK as well as subroutine developed by Christov (C.I. Christov, Gaussian elimination with pivoting for multi-diagonal systems, International Report (4), Publisher, University of Reading, 1994) are used.

    (b) $\tilde{\psi}_{i,j} = \dfrac{\psi_{i,j}^{n+1,1} + \psi_{i,j}^n}{2}$ then calculate $\psi_{i,j}^{n+1,2}$ from the system of algebraic equation (2.19) added boundary conditions (2.5)–(2.8).

    (c) $\tilde{\psi}_{i,j} = \dfrac{\psi_{i,j}^{n+1,2} + \psi_{i,j}^n}{2}$ then calculate $\psi_{i,j}^{n+1,3}$ from the system of algebraic equation (2.19) added boundary conditions (2.5)–(2.8).

Step 3. If the following criterion is satisfied

$$\max_{i,j} \left| \psi_{i,j}^{n+1,3} - \psi_{i,j}^n \right| \leqslant \varepsilon \tag{2.20}$$

then the calculations are terminated and $\psi_{i,j}^{n+1} = \psi_{i,j}^{n+1,3}$. Otherwise the index of iterations is stepped up $n := n + 1$ and the computation is returned to Step 2.

2.4   Results

The results from numerical simulations of the 2D lid-driven cavity flow were presented and compared with published observations. Firstly, a comparison was made between three algorithms that were conducted using the quantities of the stream function and velocity along the cavity centerlines. Secondly, the simulations were performed to evaluate effect of the grid on accuracy of the numerical solution.

2.4.1   Comparisons for the stream function

In this paragraph, performance of three finite-difference schemes from the previous section is discussed. Patterns of stream lines and values and locations of the extrema of the stream function are analyzed. Values of the vorticity at the same locations for $Re \in [0, 10000]$ are also added. The steady-state computed solution is defined by the requirement of the absolute error between two time steps which is less than 10^{-8}.

The vorticity $\omega_{i,j}$ is calculated by the following formula

$$\omega_{i,j} = -\frac{\psi_{i+1,j} - 2\psi_{i,j} + \psi_{i-1,j}}{h_x^2} - \frac{\psi_{i,j+1} - 2\psi_{i,j} + \psi_{i,j-1}}{h_y^2}. \tag{2.21}$$

Numerical data used for comparisons can be found in Botella and Peyret (1998), Bruneau and Saad (2006), Christov and Marinova (2001), Spotz (1998), and Garcia (2007).

The whole three algorithms give the similar stream function that cannot be distinguished on the stream line patterns. The geometrical structure of the flow is displayed in Figures 2.3 and 2.4. To get a feel for the nature of the flow field, it is best to start by looking the streamlines at the Stoke limit $Re = 0$, when the non-linear terms drop out. Presented in Figure 2.3, the driven flow is symmetric around the vertical centerline. The location of clockwise-rotating primary eddy occurs toward the geometric center of the cavity. For $Re = 100$, the location of the primary eddy appears toward the top right. But it is found that, for $Re > 300$, the center of the primary eddy has moved lower and back towards the center plane, it moves toward the geometric center of the square cavity. In the case of $Re \leqslant 1000$, the flow is distinguished by the primary eddy in the center and two counterclockwise-rotating secondary eddies in the bottom corners. For $Re > 1000$, there is an extra counterclockwise-rotating eddy in the upper left corner (as seen in Figure 2.4). For secondary eddies, the corner eddies are symmetric around the midplane in the Stoke flow. As the Reynolds number increases, both bottom right and bottom left secondary eddies grow in size. Growth of the bottom right eddy is greater, as shown in Figure 2.3. As the value of the Reynolds number is increased up to $Re = 7500$, the bottom right clockwise-rotating tertiary eddy is uncovered, as shown in Figure 2.6. Size of the bottom right tertiary and top left eddies increase as the Reynolds number increased from $Re = 7500$ to 10000.
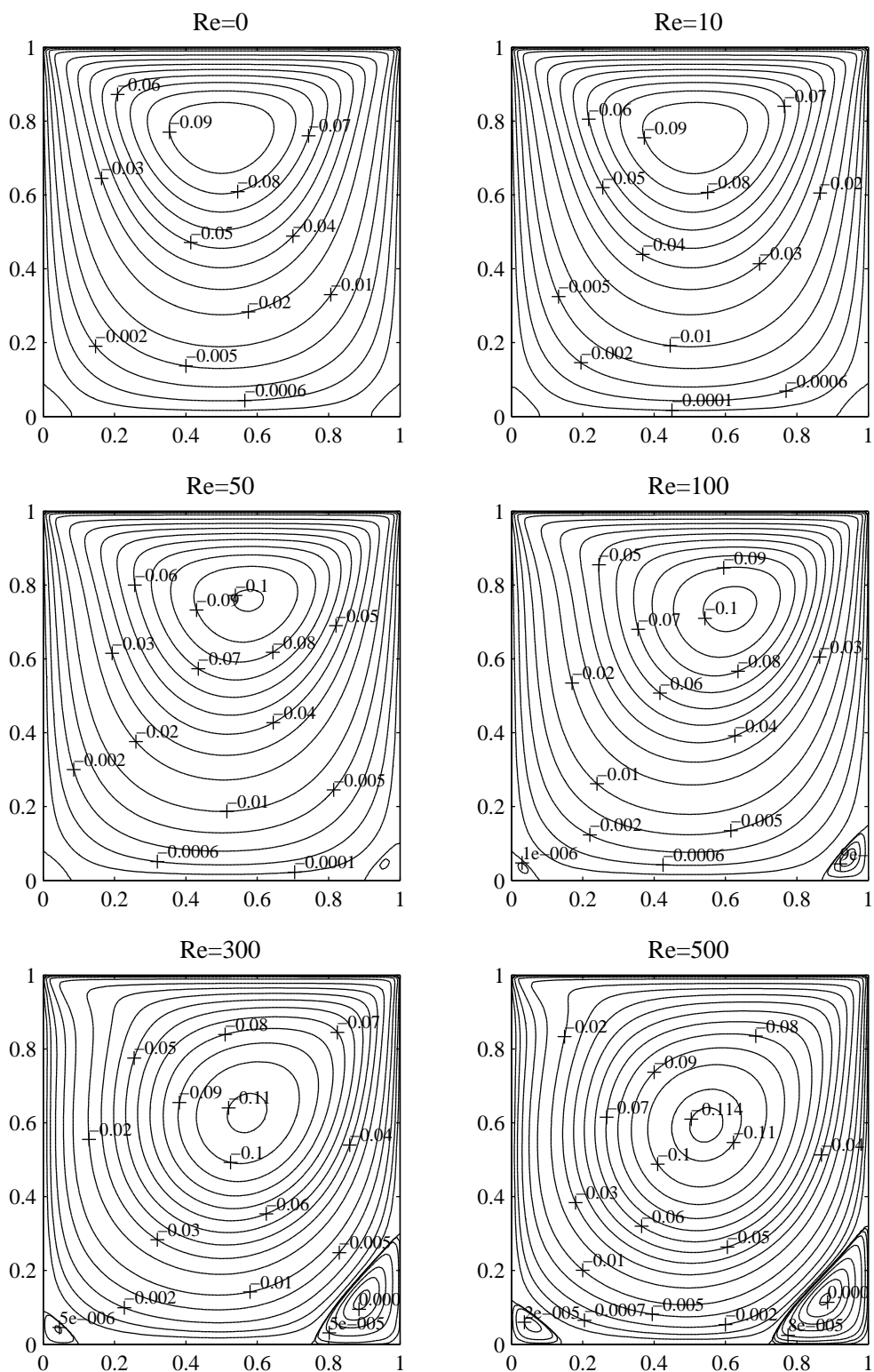
Figure 2.3 Streamline contours for $Re = 0$, 10, 50, 100, 300, and 500.
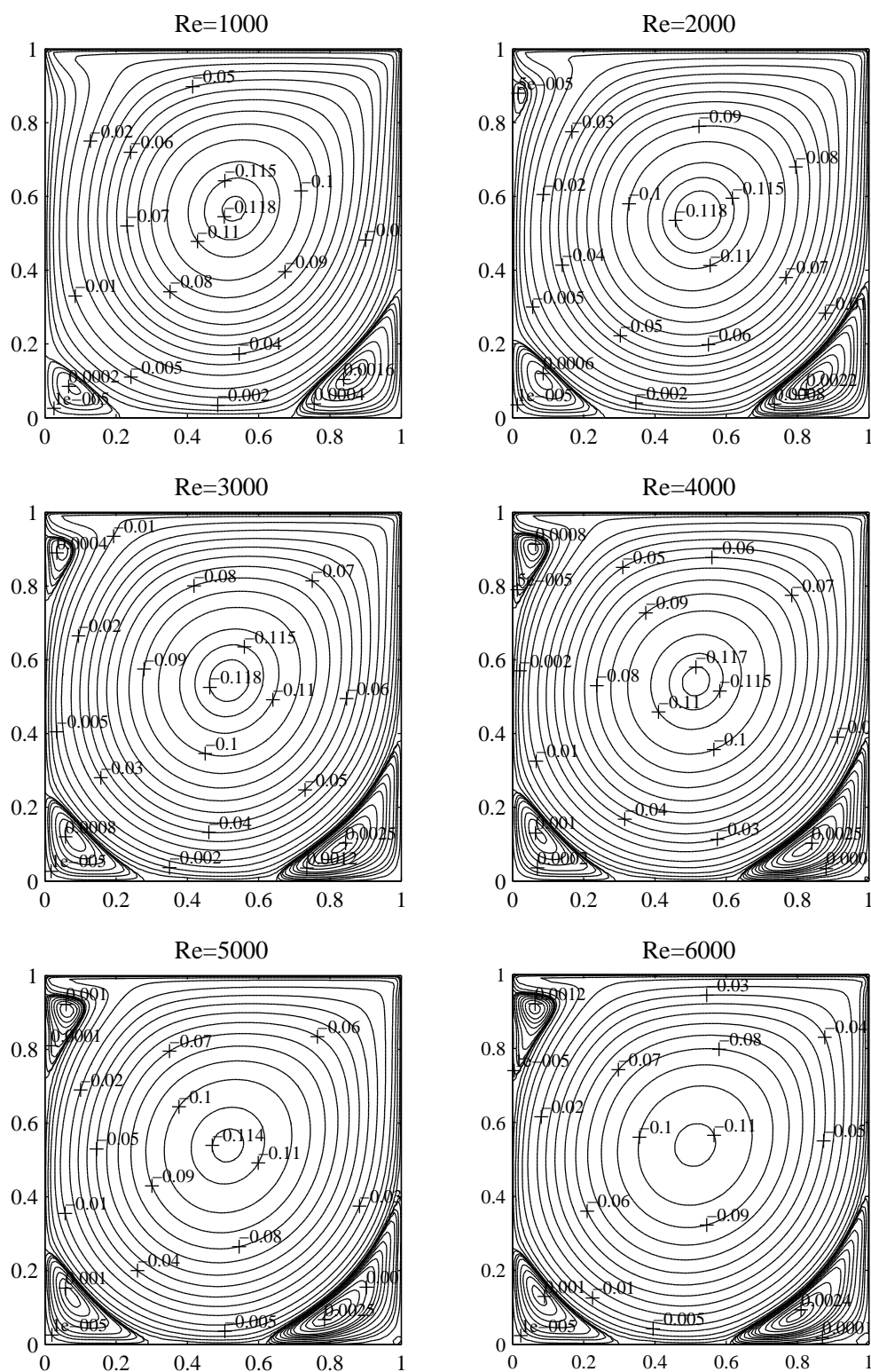
Figure 2.4 Streamline contours for $Re = 1000$, 2000, 3000, 4000, 5000, and 6000.

Table 2.1 Comparison of three schemes on the primary eddy at $Re = 1000$: minimum of the stream function and location.

Reference	Grid	ψ_{min}	ω	x_{min}	y_{min}
Explicit scheme	52×52	-0.1096	-1.911	0.540	0.560
Operator splitting	52×52	-0.1163	-2.077	0.520	0.580
Internal iteration	52×52	-0.1096	-1.911	0.540	0.560
Explicit scheme	102×102	-0.1162	-2.022	0.530	0.560
Operator splitting	102×102	-0.1186	-2.074	0.530	0.560
Internal iteration	102×102	-0.1162	-2.022	0.530	0.560
Botella et al. (1998)	160	-0.11894	-2.0678	0.5308	0.5652
Spotz (1998)	41×41	-0.11724	-2.0533	0.5250	0.5750
Christov et al. (2001)	512×512	-0.11627	–	0.5316	0.5660
Bruneau et al. (2006)	128×128	-0.11786	-2.0508	0.53125	0.5625
Bruneau et al. (2006)	1024×1024	-0.11892	-2.0674	0.53125	0.56543

In Table 2.1, characteristics of the primary eddy for $Re = 1000$ are represented. It shows values of ψ_{min}, ω, and the space location of the stream function ψ_{min}. Six top rows display quantities from three finite-difference methods. From five bottom rows, the quantities obtained by the other authors are displayed. The finite-difference solutions are also compared with the other authors. As shown, three finite-difference schemes give the very similar quantities on the grid 102×102. The values of ψ_{min}, ω, and their locations are in accordance with results observed in the literatures (Botella and Peyret, 1998; Spotz, 1998; Christov and Marinova, 2001; Bruneau and Saad, 2006).

Table 2.2 Comparison of three schemes on the bottom right secondary eddy at $Re = 1000$: maximum of the stream function and location.

Reference	Grid	ψ_{max}	ω	x_{max}	y_{max}
Explicit scheme	52×52	1.301×10^{-3}	0.9891	0.880	0.120
Operator splitting	52×52	1.597×10^{-3}	0.9802	0.860	0.120
Internal iteration	52×52	1.302×10^{-3}	0.9891	0.880	0.120
Explicit scheme	102×102	1.611×10^{-3}	1.005	0.870	0.110
Operator splitting	102×102	1.699×10^{-3}	1.079	0.860	0.110
Internal iteration	102×102	1.611×10^{-3}	1.006	0.870	0.110
Botella et al. (1998)	160	1.7297×10^{-3}	1.1098	0.8640	0.1118
Spotz (1998)	41×41	1.731×10^{-3}	0.9847	0.8500	0.1250
Christov et al.(2001)	512×512	1.640×10^{-3}	–	0.8651	0.1118
Bruneau et al. (2006)	128×128	1.7003×10^{-3}	1.1304	0.8594	0.1094
Bruneau et al. (2006)	1024×1024	1.7297×10^{-3}	1.1120	0.8643	0.1123

In Table 2.2, characteristics of the bottom right secondary eddy for $Re = 1000$ are detailed. It reports values of ψ_{max} appears at the center of the bottom right-hand side eddy, ω, and the space location of the bottom right secondary eddy. Quantities of ψ_{max} agree with those obtained by the other authors. For the bottom right secondary eddy, the results with the grid 102×102 agree within 5% with those obtained by the other authors and case 52×52 differ significantly up to 25% with those obtained in Spotz (1998).

Table 2.3 Comparison of three schemes on the primary eddy at $Re = 5000$: minimum of the stream function and location.

Reference	Grid	ψ_{min}	ω	x_{min}	y_{min}
Explicit scheme	52×52	-0.09299	-1.422	0.540	0.520
Operator splitting	52×52	$-$	$-$	$-$	$-$
Internal iteration	52×52	-0.09315	-1.431	0.540	0.520
Explicit scheme	102×102	-0.1092	-1.714	0.520	0.540
Operator splitting	102×102	-0.1149	-1.848	0.520	0.550
Internal iteration	102×102	-0.1095	-1.727	0.520	0.540
Christov et al. (2001)	512×512	-0.116120	$-$	0.5160	0.5357
Bruneau et al. (2006)	128×128	-0.11731	-1.8595	0.51562	0.53906
Bruneau et al. (2006)	1024×1024	-0.12193	-1.9322	0.51465	0.53516
Garcia (2007)	128×128	-0.1237	$-$	0.5156	0.5352

Table 2.3 shows values of ψ_{min}, ω, and space locations of the primary eddy for $Re = 5000$. On the grid 52×52, the method of an operator splitting reaches a steady solution but this solution does not agree with the numerical solutions obtained by other authors (Bruneau and Saad, 2006; Christov and Marinova, 2001; Garcia, 2007). At the same time, the explicit and internal iteration schemes reach a 'correct' solution. For the primary eddy, results of the operator splitting scheme with the grid 102×102 agree within 5% with those obtained in Bruneau and Saad (2006) with the grid 128×128 and Christov and Marinova (2001) but the two other schemes differ significantly up to 10%.

Table 2.4 Comparison of three schemes on the bottom right secondary eddy at $Re = 5000$: maximum of the stream function and location.

Reference	Grid	ψ_{max}	ω	x_{max}	y_{max}
Explicit scheme	52×52	1.006×10^{-3}	1.485	0.900	0.060
Operator splitting	52×52	–	–	–	–
Internal iteration	52×52	1.006×10^{-3}	1.483	0.900	0.060
Explicit scheme	102×102	2.622×10^{-3}	2.359	0.830	0.070
Operator splitting	102×102	2.576×10^{-3}	2.207	0.800	0.080
Internal iteration	102×102	2.624×10^{-3}	2.357	0.830	0.070
Christov et al. (2001)	512×512	2.890×10^{-3}	–	0.8077	0.0736
Bruneau et al. (2006)	128×128	2.9313×10^{-3}	2.7718	0.8047	0.0703
Bruneau et al. (2006)	1024×1024	3.0694×10^{-3}	2.7245	0.8057	0.0732
Garcia (2007)	128×128	3.07×10^{-3}	–	0.7891	0.0781

Table 2.4 reports values of ψ_{max}, ω, and the space location of the bottom right secondary eddy. For the bottom right secondary eddy, the quantities ψ_{max} with the grid 102×102 agree within 10% with those obtained in Bruneau and Saad (2006) with the grid 128×128 and Christov and Marinova (2001) and differ significantly up to 15% with those obtained Bruneau and Saad (2006) with 1024×1024 mesh and Garcia (2007).

At the high Reynolds number the flow becomes more complicated and significantly finer grids are needed in the vicinity of the walls where the dynamics of the flow is dominated by the viscosity. The coarse grid in general will not resolve the viscous layer near the boundary. In an example, as can be seen on the grid 52×52, the operator splitting method can not get a correct solution. Moreover, the other

two have value of ψ_{max} differ significantly up to 67% with those obtained Bruneau and Saad (2006) with 1024×1024 mesh. With these observations, one can conclude that grid refinement affects the size and position of the eddies. This conclusion can be drawn by examining in Figures 2.5 and 2.6 where the internal iteration method used on the grid 52×52 and 102×102 for $Re = 7500$.
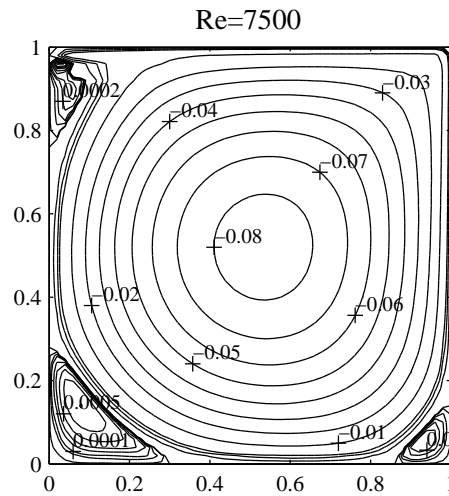
Figure 2.5 Streamline contours for $Re = 7500$ on the grid 52×52.
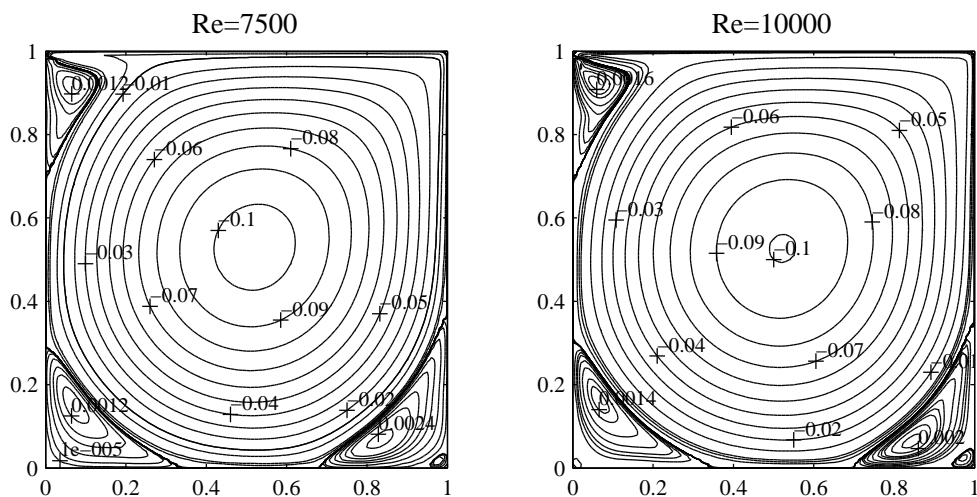
Figure 2.6 Streamline contours for $Re = 7500$ and $Re = 10000$ on the grid 102×102.

One can see, loss of the vortex structure occurs on the bottom right and top left secondary eddies. The turbulence within a lid-driven cavity is maintained by continuous production of the kinetic energy from the lid (moving wall). Only the internal iteration scheme used for higher Reynolds number $Re \geqslant 7500$. The comparisons of numerical results from simulations are presented in Table 2.5. The vortex structures are shown in Figure 2.6 for the Reynolds number $Re = 7500$ and $Re = 10000$ on 102×102 mesh. The quantity of ψ_{min} on the primary eddy agree within 1% with those obtained in Goyon (1996) for $Re = 7500$ while differ significantly up to 12% with Christov and Marinova (2001) in case $Re = 10000$.

Table 2.5 Comparison of numerical solutions on the primary and bottom right secondary eddies.

Re	Reference	Grid	Primary eddy		Bottom right secondary eddy	
			ψ_{min}	location	ψ_{max}	location
7500	Internal iteration	102×102	-0.1042	$(0.520, 0.530)$	2.636×10^{-3}	$(0.840, 0.070)$
	Goyon (1996)	256×256	-0.1052	$(0.5156, 0.5312)$	3.06×10^{-3}	$(0.8008, 0.0664)$
	Christov and Marinova (2001)	512×512	-0.113472	$(0.5141, 0.5322)$	3.022×10^{-3}	$(0.7946, 0.06587)$
	Garcia (2007)	256×256	-0.1246	$(0.5117, 0.5313)$	–	–
10000	Internal iteration	102×102	-0.1004	$(0.510, 0.530)$	2.544×10^{-3}	$(0.840, 0.060)$
	Shen (1991)	49×49	-0.08824	$(0.536, 0.531)$	3.2494×10^{-4}	$(0.922, 0.094)$
	Christov and Marinova (2001)	512×512	-0.113848	$(0.5129, 0.5303)$	3.010×10^{-3}	$(0.7812, 0.0605)$
	Garcia (2007)	256×256	-0.1230	$(0.5117, 0.5313)$	–	–

2.4.2   Comparisons for the velocity components

In this part, the velocity profiles for the horizontal and vertical lines through the geometrical center of the cavity are presented. The profiles of u (velocity in $x-$direction) along the vertical cross section and v (velocity in $y-$direction) along the horizontal cross section are shown in Figures 2.7 and 2.8 which generated using the grid 102×102. The values of the velocity were marked with the different line: —— explicit scheme; $- - -$ operator splitting scheme; $- \cdot -\cdot$ internal iteration scheme. The values of the extrema of the velocity through the cavity center are given in Tables 2.6 and 2.7 for the case $Re = 1000$ and $Re = 5000$, respectively.

Table 2.6 shows that results from numerical simulations using the operator splitting scheme on both grids agree within 3% with those obtained in Botella and Peyret (1998). The two other schemes differ significantly up to 10% in the case of the grid 52×52.
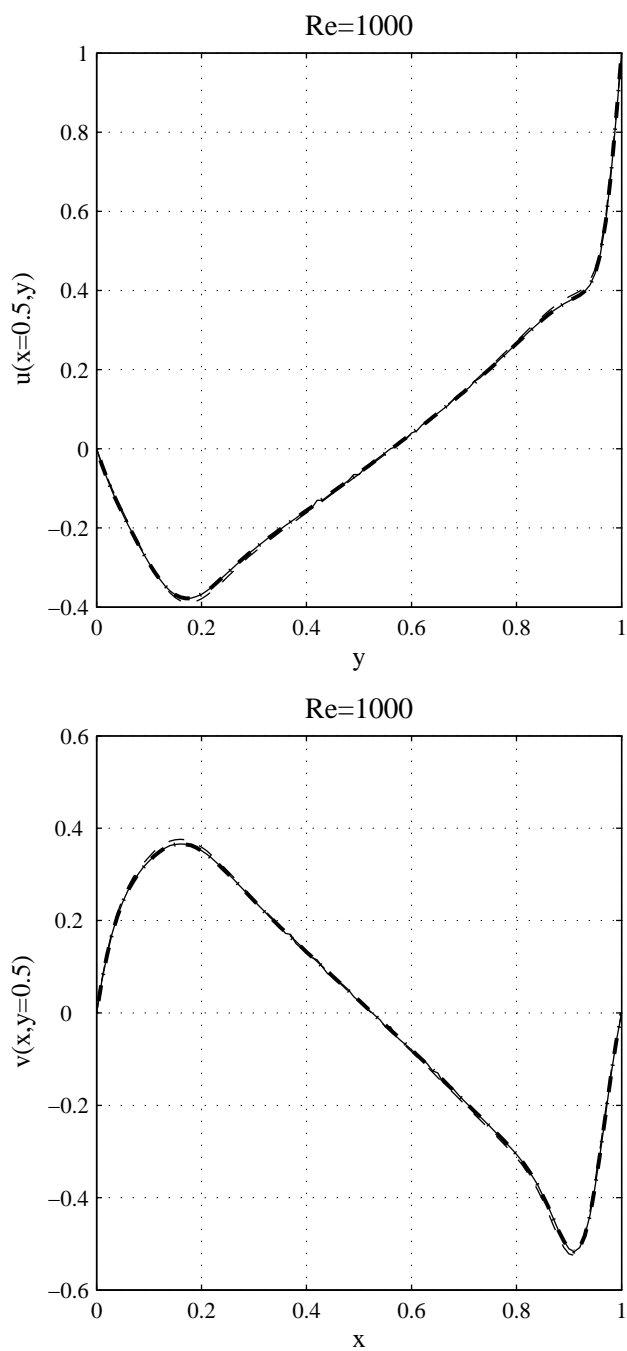
Figure 2.7 Velocity profiles through the cavity center, $Re = 1000$.

Table 2.6 Extrema of the velocity through the center lines of the cavity at $Re = 1000$.

Reference	Grid	u_{min}	y_{min}	v_{max}	x_{max}	v_{min}	x_{min}
Explicit scheme	52×52	-0.353	0.180	0.340	0.160	-0.488	0.920
Operator splitting	52×52	-0.381	0.180	0.367	0.160	-0.511	0.900
Internal iteration	52×52	-0.353	0.180	0.340	0.160	-0.488	0.920
Explicit scheme	102×102	-0.378	0.170	0.366	0.160	-0.517	0.910
Operator splitting	102×102	-0.388	0.170	0.376	0.160	-0.525	0.910
Internal iteration	102×102	-0.378	0.170	0.366	0.160	-0.517	0.910
Botella et al. (1998)	48	-0.3885271	0.1717	0.3768991	0.1578	-0.5270168	0.9092
Botella et al. (1998)	96	-0.3885698	0.1717	0.3769447	0.1578	-0.5270771	0.9092
Botella et al. (1998)	160	-0.3885698	0.1717	0.3769447	0.1578	-0.5270771	0.9092
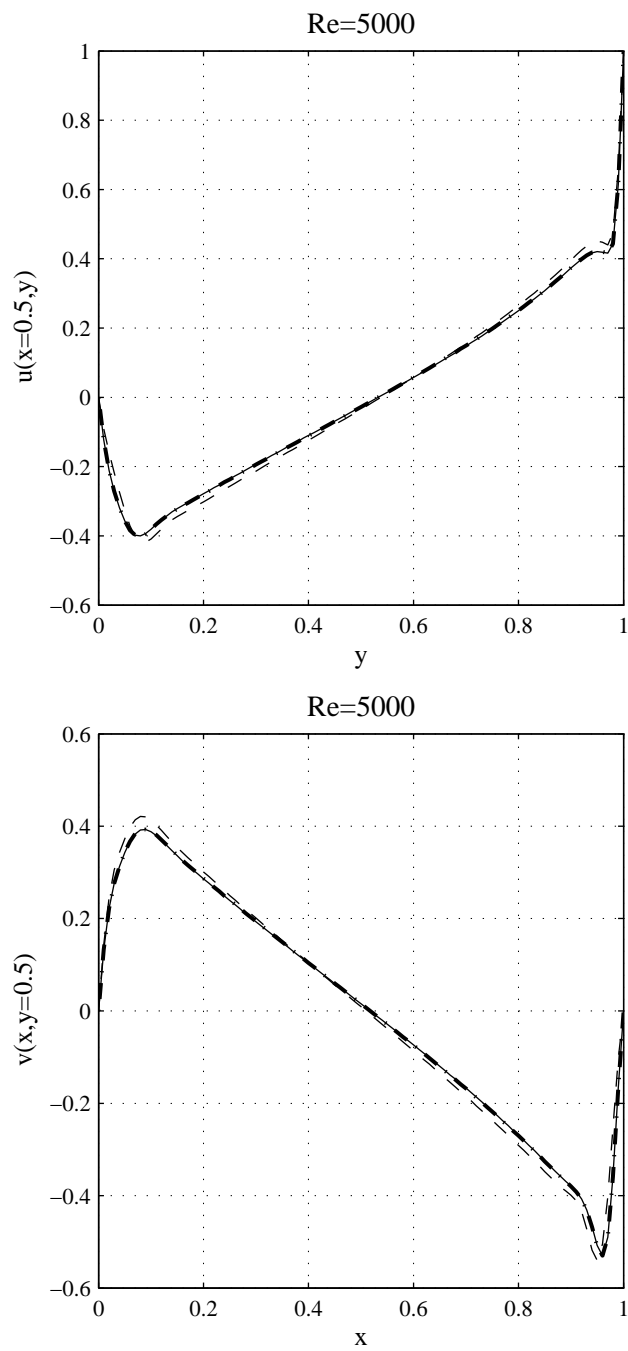
Figure 2.8 Velocity profiles through the cavity center, $Re = 5000$.

Table 2.7 Extrema of the velocity through the center lines of the cavity at $Re = 5000$.

Reference	Grid	u_{min}	y_{min}	v_{max}	x_{max}	v_{min}	x_{min}
Explicit scheme	52×52	-0.349	0.080	0.324	0.100	-0.525	0.980
Operator splitting	52×52	–	–	–	–	–	–
Internal iteration	52×52	-0.349	0.080	0.324	0.100	-0.525	0.980
Explicit scheme	102×102	-0.400	0.080	0.393	0.090	-0.530	0.960
Operator splitting	102×102	-0.418	0.090	0.421	0.080	-0.540	0.950
Internal iteration	102×102	-0.401	0.080	0.393	0.090	-0.530	0.960

Since a majority of the disagreement was observed on the grid 52×52 at $Re = 5000$, it seems necessary to refine the grid to get results close to the true solution. Analyzing the results obtained in this section, it seems plausible to conclude the numerical accuracy depends on the grid used. This statement is substantiated by results presented in the following part, where a grid convergence studied.

2.4.3   Convergence

To evaluate the grid dependence on spatial variables the solution was obtained on a sequence of grids with 32×32, 62×62, and 122×122 nodes. To estimate the rate of convergence, the validity of expression

$$f_e \approx f_h + Ch^\alpha \tag{2.22}$$

is accepted where f_e and f_h are quantities related to the exact and computed solutions, respectively. Coefficients C and α independent of h. Since given solutions on three grids equation (2.22) can be solved for three unknowns f_e, C, and α. In Tables 2.8 and 2.9, values of ψ_{min} were computed minimum values of the stream function. Parameter α_{min} represents the rate of convergence when in equation (2.22) instead f used ψ_{min}. Table 2.8 represents a steady-state. The solutions are qualified as steady when the absolute error between two time steps which is less than 10^{-8} on a significant time interval. The solutions show the second-order rate of convergence of finite-difference methods. Table 2.9 shows the results of a numerical experiment at fixed moment of time $t = 0.1$. This clearly shows that the rate of convergence of three schemes is the second-order.

Table 2.8 Verification for the rate of convergence of the three schemes at $Re = 100$, $\tau = 2 \times 10^{-4}$, and $\varepsilon = 10^{-8}$.

Reference	Grid	ψ_{min}	α_{min}	f_e	$|f_e - \psi_{min}|$
Explicit scheme	32×32	-0.1015785	1.953	-0.1035116	1.9331×10^{-3}
	62×62	-0.1030120			4.9960×10^{-4}
	122×122	-0.1033825			1.2910×10^{-4}
Operator splitting	32×32	-0.1024849	2.078	-0.1035016	1.0167×10^{-3}
	62×62	-0.1032607			2.4090×10^{-4}
	122×122	-0.1034445			5.7100×10^{-5}
Internal iteration	32×32	-0.1015785	1.953	-0.1035111	1.9326×10^{-3}
	62×62	-0.1030120			4.9910×10^{-4}
	122×122	-0.1033822			1.2890×10^{-4}

Table 2.9 Verification for the rate of convergence of the three schemes at $Re = 100$, $\tau = h^2$, and $t = 0.1$.

Reference	Grid	ψ_{min}	α_{min}	f_e	$|f_e - \psi_{min}|$
Explicit scheme	32×32	-0.1014032	1.910	-0.1033497	1.9465×10^{-3}
	62×62	-0.1028318			5.1790×10^{-4}
	122×122	-0.1032119			1.3780×10^{-4}
Operator splitting	32×32	-0.1022921	2.026	-0.1033371	1.0450×10^{-3}
	62×62	-0.1030805			2.5660×10^{-4}
	122×122	-0.1032741			6.3000×10^{-5}
Internal iteration	32×32	-0.1014053	1.910	-0.1033497	1.9444×10^{-3}
	62×62	-0.1028323			5.1740×10^{-4}
	122×122	-0.1032120			1.3770×10^{-4}

Table 2.10 Number of iterations to reach steady solution for $Re = 100, h_x = h_y = \frac{1}{50}$, and different τ.

τ	Explicit scheme	Operator splitting	Internal iteration
0.0030	Divergence	Divergence	**108**
0.0010	**243**	Divergence	243
0.0005	458	**458**	458
0.0001	1986	1985	1986

Table 2.11 Number of iterations to reach steady solution for $Re = 1000, h_x = h_y = \frac{1}{50}$, and different τ.

τ	Explicit scheme	Operator splitting	Internal iteration
0.00008	Divergence	Divergence	**1588**
0.00005	Divergence	Divergence	2404
0.00003	Divergence	**3581**	3757
0.00002	**5276**	5082	5340
0.00001	9606	9174	9667
0.000005	17251	16365	17312

For fixed values of h_x and h_y, the number of iterations needed for convergence to steady-state (reach criterion (2.10)) depend on τ. For definiteness, the Reynolds numbers $Re = 100$ and $Re = 1000$ were selected to present. The largest value of time-step τ^* and number of iterations to reach steady-state are shown in Tables 2.10 and 2.11 for $Re = 100$ and $Re = 1000$, respectively. The minimal number of iteration for each scheme is shown in a bold face. The minimal number of iterations on the

grid 52×52 are 5276 iterations , 3581 iterations, and 1588 iterations for the cases of the explicit, operator splitting, and internal iteration schemes, respectively. One can observe that the minimal number of the internal iteration method is less than the other two. Moreover, the results show that the internal iteration method requires slightly larger time-step.
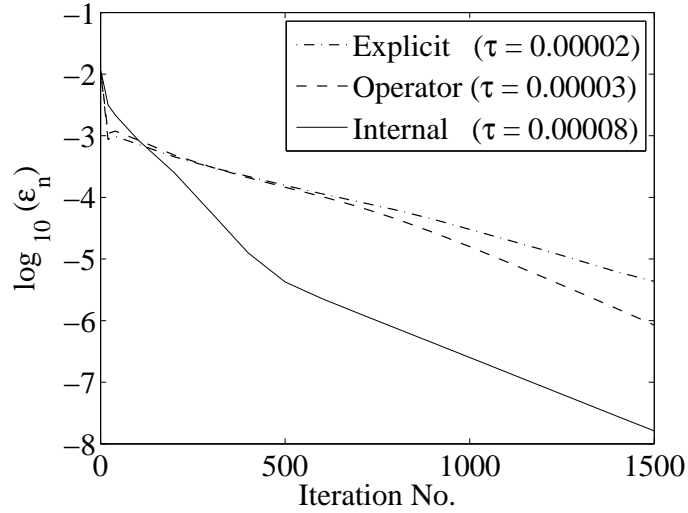
Figure 2.9 Iteration history for $Re = 1000$.

To show the history of convergence, Figure 2.9 is plotted in case $Re = 1000$ on the grid 52×52. It shows the absolute error ε_n versus the number of iterations when the largest value of time-step τ^* (as shown in Table 2.11) used and

$$\varepsilon_n = \max_{i,j} \left| \psi_{i,j}^n - \psi_{i,j}^{n-1} \right|.$$

The iterations were started with zero initial data and were terminated when $N = 1500$. In Figure 2.9, the error of internal iteration method decrease faster than the error of explicit and operator splitting schemes. From comparison, its is observed that the internal iteration method seem to be performing better than the other two methods.

Table 2.12 Largest value of time-step τ^* for different Re.

Grid	Re	Explicit scheme τ^*	Operator splitting τ^*	Internal iteration τ^*
52×52	100	1×10^{-3}	5×10^{-4}	3×10^{-3}
	200	3×10^{-4}	2×10^{-4}	7×10^{-4}
	500	7×10^{-5}	6×10^{-5}	1×10^{-4}
	1000	2×10^{-5}	3×10^{-5}	8×10^{-5}
	2000	6×10^{-6}	1×10^{-5}	4×10^{-5}
	3000	3×10^{-6}	1×10^{-5}	2×10^{-5}
	4000	1×10^{-6}	-	2×10^{-5}
	5000	9×10^{-7}	-	2×10^{-5}
102×102	100	5×10^{-4}	2×10^{-4}	2×10^{-3}
	200	1×10^{-4}	1×10^{-4}	3×10^{-4}
	500	4×10^{-5}	2×10^{-5}	1×10^{-4}
	1000	1×10^{-5}	1×10^{-5}	3×10^{-5}
	2000	2×10^{-6}	6×10^{-6}	1×10^{-5}
	3000	1×10^{-6}	4×10^{-6}	8×10^{-6}
	4000	1×10^{-6}	3×10^{-6}	7×10^{-6}
	5000	5×10^{-7}	2×10^{-6}	5×10^{-6}

Table 2.12 shows τ^* for which it is possible to reach a steady solution which correspond to other investigators. The results show that finite-difference solutions on the grid 52×52 are not acceptable for the case $Re = 4000$ and $Re = 5000$ which the operator splitting method used. It is shown that the present schemes converges to a 'correct' solutions in all the cases $Re \leqslant 3000$ considered. These calculations indicate that the proposed schemes are stable even when used the coarse mesh and relatively largest time-step. If the grid spacing is too coarse, then the operator splitting scheme will not compute a qualitatively correct solution for $Re > 3000$ as seen in the fourth column of Table 2.12. If precise information increase the Reynolds number $Re > 3000$ is needed and it is not cost-effective to use a small grid spacing, then the other two methods (explicit and internal iteration methods) should be considered to obtain this information. Moreover, the internal iteration method requires slightly larger time-step.

Also, the increase of the time to computational when the Reynolds number increased can be observed. The following Table 2.13 shows that the modification of explicit method (the internal iteration method) can reduce the computational time for higher Reynolds number ($Re \geqslant 1000$).

Table 2.13 Minimal number of iteration for different Re when $t = 0.42$.

Grid	Re	Explicit scheme		Operator splitting		Internal iteration	
		τ^*	No.	τ^*	No.	τ^*	No.
51×51	100	1×10^{-3}	420	5×10^{-4}	840	3×10^{-3}	140
	200	3×10^{-4}	1400	2×10^{-4}	2100	7×10^{-4}	600
	500	7×10^{-5}	6000	6×10^{-5}	7000	1×10^{-4}	4200
	1000	2×10^{-5}	21000	3×10^{-5}	14000	8×10^{-5}	5250
	2000	6×10^{-6}	70000	1×10^{-5}	42000	4×10^{-5}	10500
	3000	3×10^{-6}	140000	1×10^{-5}	42000	2×10^{-5}	21000
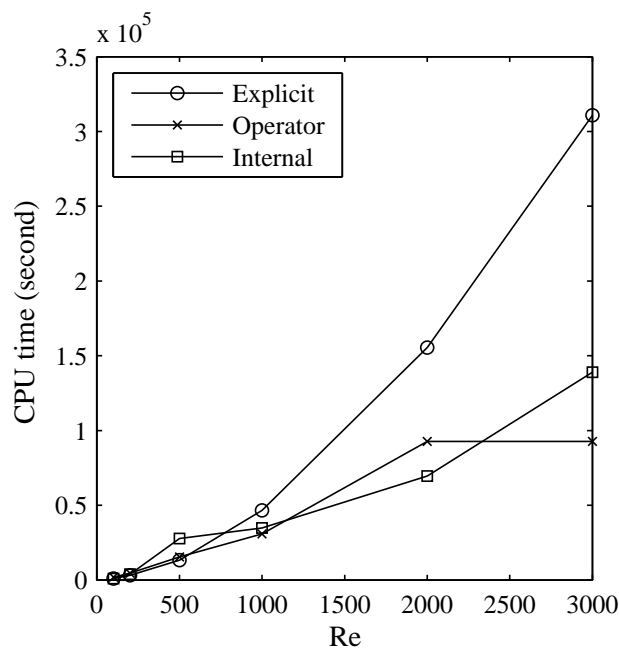
Figure 2.10 Curves based on the data in Table 2.13.

Computations were carried out on a personal computer with 2.4 GHz CPU. The CPU time per one time step (/one iteration) on the grid 52×52 is about 2.22031, 2.20781, and 6.61875 sec for cases of the explicit, operator splitting, and internal iter-

ation schemes, respectively. Table 2.13 shows the results of solving the problem (2.1) using three finite-difference schemes. The six different Reynolds numbers are displayed in the second column of Table 2.13. The next columns show the largest value of τ^* and the number of iterations required to obtain a solution at the moment of time $t = 0.42$. Since the operator splitting scheme involves roughly $1/3$ time as much work per method of the internal iteration and roughly the same time as the explicit scheme then the operator splitting method is slower than the other two methods for $Re < 500$, but probably not for $Re \geqslant 500$. Figure 2.10 shows the CPU-time needed to find solution at the moment of time $t = 0.42$ with largest value of the parameter τ^* on the grid 52×52.

2.5 Conclusion

This chapter is based upon three finite-difference schemes (explicit, operator, and internal iteration). The solutions computed with these schemes are in good agreement with the numerical data of other research (e.g., Shen, 1991; Botella and Peyret, 1998; Goyon, 1996; Bruneau and Saad, 2006; Christov and Marinova, 2001; Spotz, 1998). The numerical results are demonstrated that the internal iteration is one method to compute the characteristic of flow for the high Reynolds number. The largest time increment of three internal iterations scheme gives convergence to solution roughly three times faster as explicit scheme is founded.

As important feature that the internal iteration method allows coarsening of the grid depending on the flow solution. This feature is extremely useful for accuracy predicting flow fields in region with the high Reynolds number. Moreover, the rate of convergence of internal iteration scheme to solution is decreased faster than the explicit scheme.

2.6   References

Botella, O. and Peyret, R. (1998). Benchmark spectral results on the lid-driven cavity flow. **Computer & Fluids** 27(4):421–433.

Bruneau, C.H., and Saad M. (2006). The 2D lid-driven cavity problem revisited. **Computer & Fluids** 35:326–348.

Christov, C.I., and Marinova, R.I. (2001). Implicit vectorial operator splitting for incompressible Navier-Stokes equations in primitive. **Journal Computatinal Technologies** 6(4):92–119.

Christov, C.I., and Ridha, A. (1994). Splitting scheme for iterative solution of bi-harmonic equation, Application to 2D Navier-Stokes problems. **Advances in Numerical Methods and Appl., Singapure: World Sci.** 341–352.

Christov, C.I., and Ridha, A. (1995). Splitting scheme for the stream function formulation of 2D unsteady Navier-Stokes equations. **Comptes rendus de l'Academie des sciences Paris** 320(II b):441–446.

Christov, C.I., and Tang X.H. (2006). An Operator Splitting Scheme for the Stream-Function Formulation of Unsteady Navier-Stokes Equations. **International Journal for Numerical Methods in Fluids** 53(3):417–442.

Garcia, S. (2007). The lid-driven square cavity flow: from stationary to time periodic and chaotic. **Communications in Computational Physics** 2(5):900–932.

Goyon, O. (1996). High-Reynolds number solutions of Navier-Stokes equations using incremental unknowns. **Computer Methods in Applied Mechanics and Engineering** 130:319-335.

Iliev, O.P., and Makarov, M.M. (1995). A block matrix iterative numerical method for coupled solving 2D Navier-Stokes equations. **Journal of Computational Physics** 121:324–330.

Karnaidakis, G., Israeli, M., and Orszag, S.A. (1991). High-order splitting methods for the incompressible Navier-Stokes equations. **Journal of Computational Physics** 27:414–443.

Kim, J., and Moin, P. (1985). Application of fractional-step method to incompressible Navier-Stokes equations. **Journal of Computational Physics** 59:308–323.

Mallison, G.D., and De Vahl David, G. (1973). The method of false transients for the solution of coupled elliptic equations. **Journal of Computational Physics** 12:435–461.

Marchuk, G.I. (1975). **Methods of Numerical Mathematics 4**. Springer-Verlag.

Quartapelle, L. (1981). Volticity conditioning in the computation of two-dimensional viscous flows. **Journal of Computational Physics** 40:453–477.

Rosenfeld, M., Kwak, D., and Vinokur, M. (1991). A fractional step solution method for the unsteady incompressible Navier-Stokes equations in generalized coordinate system. **Journal of Computational Physics** 94:102–137.

Smagulov, Sh., and Christov, C.I. (1980 Preprint). Iterationless numerical implementation of the boundary conditions in vorticity-stream function formulation of Navier-Stokes equations. **Inst. Theor. Appl. Mech., Russian Acad. Sci.** Novosibirsk.

Spotz, W.F. (1998). Accuracy and performance of numerical wall boundary conditions for steady, 2D, incompressible streamfunction vorticity. **international**

journal for numerical methods in fluids 28:737–757.

Shen, J. (1991). Hopf bifurcation of the unsteady regularized driven cavity flow. **Journal of Computational Physics** 95:228–245.

Temam, R. (ed.). (1977). **Navier-Stokes Equations**. North-Holland, Amsterdam.

Vabishchevich, P.N. (1984). Implicit finite-difference schemes for the nonstationary Navier-Stokes equations with the stream function and vorticity as variables. **Differential Equations** 20:820–827.

CHAPTER III

NEW NUMERICAL METHOD FOR THE SIMULATION OF 2D AXISYMMETRICAL VISCOUS INCOMPRESSIBLE FLOW

In the present work, a finite-difference technique is developed for the implementation of a new method proposed by Aristov and Pukhnachev (Doklady Physics, 49(2), (2004)) for modelling axisymmetric viscous incompressible fluid flows. A new function is introduced that is related to the pressure and a system similar to the vorticity/stream function formulation which is derived for the cross-flow. This system is coupled to an equation for the azimuthal velocity component. The scheme and algorithm treat the equations for the cross-flow as an inextricably coupled system which allows one to satisfy two conditions for the stream function with no condition on the auxiliary function. The issue of singularity of the matrix is tackled by adding a small parameter in the boundary conditions. The scheme is thoroughly validated on girds with different resolutions.

The new numerical tool is applied to the Taylor flow between concentric rotating cylinders when the upper and lower lids are allowed to rotate independently from the inner cylinder, while the outer cylinder is held at rest. The phenomenology of this flow is adequately represented by the numerical model, including the hysteresis that takes place near certain specific values of the Reynolds number. Thus the present results can be construed to demonstrate the viability of the new model. The success can be attributed to the adequate physical nature of the auxiliary function.

The proposed technique can be used in the future for in-depth investigations of the bifurcation phenomena in rotating flows.

3.1 Introduction

Axisymmetric-rotating flows have been studied for a variety of reasons. Their technological applications are many (e.g., centrifugal pumps, cyclone separators and so on). Their importance to geophysical flows is indicated over a large range of scales (e.g., tornadoes, hurricanes, ocean circulations). Axisymmetric-rotating flows occur for an example in flows past axisymmetric bodies. The axisymmetric jet also belongs under this class. A familiar and well studied example of axisymmetric flow is the flow between concentric cylinders where the inner rotates, which is commonly called the Taylor-Couette problem. The transition from azimuthal Couette flow to a cellular Taylor vortex flow has been recognized as a cornerstone of hydrodynamic stability theory.

Traditionally, axisymmetric-rotating flows have been treated by representing NSEs in cylindrical coordinates. The stream function, or the velocity and pressure field are used to numerical simulation in many research. In Youd and Barenghi (2005) the governing equations are solved by a finite-difference method using the stream-function vorticity formulation. The equations are discretised using second-order accurate centred differences and are time stepped using a combination of second-order accurate Crank-Nicolson and Adam-Bashfort methods. In series of works (Brown and Lopez, 1990; Lopez, 1990; Lopez and Perry, 1992) the mechanism of vortex breakdown in swirling flows is studied. A comparison between experimental visualization and numerical simulations is presented. The system of NSEs is solved by employing the stream-function vorticity formulation, where the pressure does not appear explicitly. In Inamuro, Yamaguchi, and Ogino (1997) the NSEs with boundary

conditions are solved using a finite-volume method based on the SIMPLE algorithm. The QUICK scheme is used for the convective terms. The finite-element package ENTWIFE is utilized to numerical solution of the steady axisymmetric NSEs in Pfister, Schmidt, Cliffe, and Mullin (1988), Mullin and Blohm (2001), Mullin, Toya, and Tavener (2002), Abshagen et al. (2004). The nonlinear dynamics of the flow in a short annuals driven by the rotating of the inner cylinder and bottom end wall was considered in Lopez, Marques, and Shen (2004). To uncouple the velocity vector and the pressure in the incompressible NSEs a projection scheme is used. For the space variables a Legendre-Fourier approximation is utilized.

A new form of the NSEs of axisymmetric motion of a viscous incompressible fluid have been proposed in Aristov and Pukhnachev (2004). The axisymmetric NSEs in terms of new functions contain two transport equations for the stream function and the azimuthal velocity component and one elliptic equation for new unknown function which coupled new unknown function with other.

The main purpose of this chapter and its sequel is to develop and validate an efficient and accurate numerical scheme for the axisymmetric NSEs in terms of new variables developed in Aristov and Pukhnachev (2004). The plan of this chapter is the following. Section 3.2 contains the governing equations of motion. Section 3.3 includes detailed description of numerical algorithm. Results of evaluation of scheme in this research are presented in Section 3.4, where a detailed comparison with available numerical and experimental data is made. The problem of the onset of Taylor vortices in a viscose fluid contained between concentric rotating cylinders is an excellent benchmark problem for axisymmetric flows. The scheme of this study is evaluated with a combined numerical and experimental study Abshagen et al. (2004) of steady bifurcation phenomenon in a modified Taylor-Couette geometry where the end plates of the flow domain are allowed to rotate independently of the inner cylinder.

3.2   Governing equations

The Taylor-Couette flow provides opportunities for detailed comparison between the results of experimental and numerical investigations. Following Abshagen et al. (2004), a variant of standard Taylor-Couette flow geometry where the end plates (lids) can rotate independently from the inner cylinder is considered.
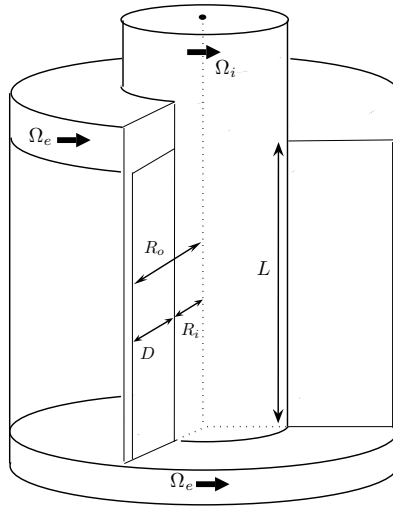
Figure 3.1 Sketch of the flow domain.

A schematic of the flow geometry is shown in Figure 3.1 where are also defined the parameters of the flow geometry:$R_i =$ is the radius of the inner cylinder, $R_o =$ is the radius of the outer cylinder, $L =$ is the axial length (height), $\Omega_i =$ is the angular velocity of the inner cylinder, $\Omega_e =$ is the angular velocity of the lids. Both the inner cylinder and the lids have the same axis and direction of rotation.

The lids rotate simultaneously with the same angular speed, and the ratio between the rate of rotation of the ends Ω_e and the inner cylinder Ω_i defines a dimensionless control parameter $\Omega = \Omega_e/\Omega_i$. The non-dimensional parameters of the problem are

$$\mathrm{Re} = \frac{DR_i\Omega_i}{\nu}, \quad \Omega = \frac{\Omega_e}{\Omega_i}, \quad \Gamma = \frac{L}{D}, \quad \eta = \frac{R_i}{R_o}, \quad D = R_o - R_i, \qquad (3.1)$$

where Re is the Reynolds number, Ω is the ratio of the angular speeds of the inner cylinder and end plates, and Γ (aspect ratio) is the ratio between the hight of the equipment L and the gap width D. The system of equations (1.11)–(1.14) is rendered dimensionless as follows

$$r = \frac{r^*}{D}, \quad z = \frac{z^*}{D}, \quad t = \frac{t^*\nu}{D^2}, \quad v = \frac{v^*D}{\nu}, \quad p = \frac{p^*D^2}{\nu^2}, \tag{3.2}$$

where the gap width D is used as the length scale, and the diffusive time across the gap, $D^2\nu^{-1}$, as the time scale.

In Abshagen et al. (2004) are presented sufficiently complete results from a combined numerical and experimental study of steady bifurcation phenomena in a modified Taylor-Couette geometry where the end plates of flow domain are allowed to rotate independently of the inner cylinder. The flow in the Taylor-Couette system with one stationary end plate and the other attached to the rotating inner cylinder was studied in Mullin and Blohm (2001) and Lopez, Marques, and Shen (2004).

Now, the results of article Aristov and Pukhnachev (2004) will be followed. The new form of the axisymmetric NSEs are written using the cylindrical polar coordinate system (r, θ, z)

$$\psi_t - \frac{1}{r}\psi_r\psi_z + \Phi_z = \mathbf{E}\psi, \tag{3.3}$$

$$J_t - \frac{1}{r}\psi_z J_r + \frac{1}{r}\psi_r J_z = \mathbf{E}J, \tag{3.4}$$

$$\mathbf{E}\Phi = \frac{1}{r^2}\left(J^2 + \psi_z^2\right) + \frac{2}{r}\psi_r\mathbf{E}\psi. \tag{3.5}$$

The main target of recent work is to develop and validate a finite-difference scheme to approximate solution of equations (3.3)–(3.5). Below, only the case where the no-slip conditions are satisfied at the boundary of the flow domain will be considered. In terms of the functions ψ and J, these conditions are represented in the form

$$\frac{\partial\psi}{\partial n} = 0, \quad \psi = 0, \quad J = \Omega r^2, \tag{3.6}$$

where $\dfrac{\partial \psi}{\partial n}$ means derivative in the direction of normal vector to the boundary, Ω is the rate of rotations of boundary surface. To close the formulation of the problem it is necessary to specify the initial conditions

$$\psi = \psi_0(r, z), J = J_0(r, z), \quad t = 0. \tag{3.7}$$

Equation (3.4) and boundary condition (3.6) for the function J can be solved independently under assumption that the function ψ is given. A difficulty in solving the system of equations for ψ and Φ supplemented by the boundary conditions above is that two boundary conditions are specified for ψ while none is available for Φ. This difficulty is similar to the vorticity-stream function equations in 2D. To overcome the difficulty caused by the absence of boundary condition for Φ in Aristov and Pukhnachev (2004) authors transform equation (3.5) into the fourth-order equation by applying the operator $\mathbf{E}$ and using boundary condition $\dfrac{\partial \psi}{\partial n} = 0$. In this case, the boundary conditions for functions ψ and Φ are uncoupled and iterative solution procedures can be used to find approximate solution. The weak point of such approach is the necessity to solve the Neumann problem for the bi-harmonic equation. Uncoupled solution of this problem can be found up to arbitrary function, which satisfies the Stokes equation $\mathbf{E}\widetilde{\Phi} = 0$.

3.3   Computational technique

A finite-difference scheme for a variant of standard Taylor-Couette flow geometry where the end plates can be rotated independently from the inner cylinder will be represented and validated. This problem was studied in Abshagen et al. (2004). The Couette flow occurs in the region

$$Q = \{\frac{\eta}{1 - \eta} < r < \frac{1}{1 - \eta}, 0 < z < \Gamma\}.$$

A sketch of domain geometry and main notations are shown in Figure 3.1. For the sake of simplicity, a uniform grid with h_r and h_z spacing in $r-$ and $z-$direction, respectively,

$$h_r = \frac{1}{(N_r - 2)}, \quad h_z = \frac{\Gamma}{(N_z - 2)},$$

$$Q_h = \Big\{ (r_i, z_j) | r_i = \frac{\eta}{1 - \eta} + (i - 1.5)h_r, \quad z_j = (j - 1.5)h_z, i = 1, \ldots, N_r,$$

$$j = 1, \ldots, N_z \Big\}$$

is assumed. The mesh is staggered in $r-$direction on $0.5h_r$ and in $z-$direction on
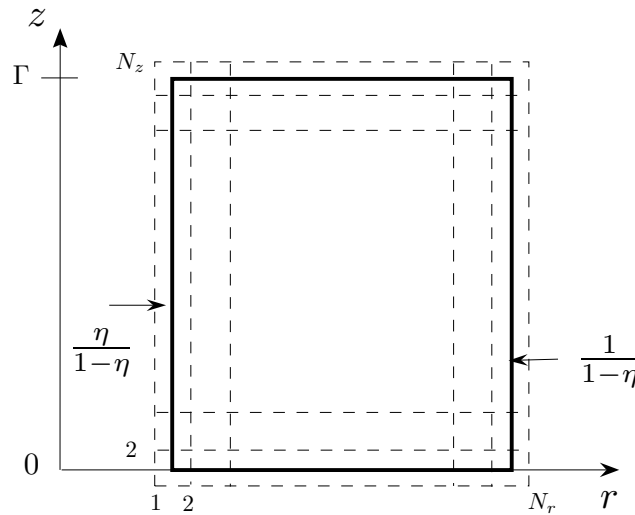
Figure 3.2 Computational domain with the grid.

$0.5h_z$ with respect domain boundaries. Such grid allows one to use central differences to approximate boundary conditions with the second-order on two-point stencils. Figure 3.2 shows the sketch of grid.

Consider first a time and spatial discretization of equation (3.4), the function J is treated on a half-time steps $t^{n+\frac{1}{2}}$, while the function ψ is taken on the main time step t^n. To approximate partial derivatives, the central finite-differences are used. The Crank-Nicolson approach utilized to increase the order of approximation with

respect time. The full discrete equations are

$$\frac{J_{i,j}^{n+1/2} - J_{i,j}^{n-1/2}}{\tau} = \frac{1}{8r_i h_r h_z} \left(\psi_{i,j+1}^n - \psi_{i,j-1}^n\right) \left(J_{i+1,j}^{n+1/2} - J_{i-1,j}^{n+1/2} + J_{i+1,j}^{n-1/2} - J_{i-1,j}^{n-1/2}\right)$$

$$- \frac{1}{8r_i h_r h_z} \left(\psi_{i+1,j}^n - \psi_{i-1,j}^n\right) \left(J_{i,j+1}^{n+1/2} - J_{i,j-1}^{n+1/2} + J_{i,j+1}^{n-1/2} - J_{i,j-1}^{n-1/2}\right)$$

$$+ \frac{1}{2} \left(\mathbf{E}J_{i,j}^{n+1/2} + \mathbf{E}J_{i,j}^{n-1/2}\right), \quad i = 2, \ldots, N_r - 1, \quad j = 1, \ldots, N_z - 1, \tag{3.8}$$

where

$$\mathbf{E}J_{i,j} = \frac{(J_{i+1,j} - 2J_{i,j} + J_{i-1,j})}{h_r^2} - \frac{(J_{i+1,j} - J_{i-1,j})}{2r_i h_r} + \frac{(J_{i,j+1} - 2J_{i,j} + J_{i,j-1})}{h_z^2}. \tag{3.9}$$

Equation (3.8) are supplemented by the boundary conditions

$$\frac{J_{1,j}^{n+\frac{1}{2}} + J_{2,j}^{n+\frac{1}{2}}}{2} = Re\frac{\eta}{1 - \eta}, \qquad \frac{J_{N_r-1,j}^{n+\frac{1}{2}} + J_{N_r,j}^{n+\frac{1}{2}}}{2} = 0, \quad j = 1, \ldots, N_z,$$

$$\tag{3.10}$$

$$\frac{J_{i,1}^{n+\frac{1}{2}} + J_{i,2}^{n+\frac{1}{2}}}{2} = Re\Omega r_i^2 \frac{1 - \eta}{\eta}, \qquad \frac{J_{i,N_z-1}^{n+\frac{1}{2}} + J_{i,N_z}^{n+\frac{1}{2}}}{2} = Re\Omega r_i^2 \frac{1 - \eta}{\eta}, \quad i = 1, \ldots, N_r.$$

The system of algebraic equations (3.8)–(3.10) can be solved by a direct method or by a suitable iterative method. In the numerical experiments, the standard routines DGBSV and DGBSVX of LAPACK are used.

Equations (3.3) and (3.5) for ψ and Φ are considered as a coupled system. This formulation is based on the idea of regarding the two boundary conditions for ψ as actual conditions for the $\psi - \Phi$ system. The second-order central-difference approximations are employed for the operators in equations (3.3) and (3.5). The system of difference equations is

$$\frac{\psi_{i,j}^{n+1} - \psi_{i,j}^n}{\tau} - \frac{(\psi_{i+1,j}^n - \psi_{i-1,j}^n)(\psi_{i,j+1}^{n+1} - \psi_{i,j-1}^{n+1}) + (\psi_{i+1,j}^{n+1} - \psi_{i-1,j}^{n+1})(\psi_{i,j+1}^n - \psi_{i,j-1}^n)}{8r_i h_r h_z}$$

$$+ \frac{\left(\Phi_{i,j+1}^{n+1} - \Phi_{i,j-1}^{n+1}\right)}{2h_z} = \frac{1}{2}\left(\mathbf{E}\psi_{i,j}^{n+1} + \mathbf{E}\psi_{i,j}^n\right), \tag{3.11}$$

$$\mathbf{E}\Phi_{i,j}^{n+1} = \frac{1}{r_i^2}\left((J_{i,j}^{n+1/2})^2 + \frac{1}{4h_z^2}(\psi_{i,j+1}^n - \psi_{i,j-1}^n)(\psi_{i,j+1}^{n+1} - \psi_{i,j-1}^{n+1})\right)$$
$$+ \frac{1}{2r_i h_r}\left((\psi_{i+1,j}^n - \psi_{i-1,j}^n)\mathbf{E}\psi_{i,j}^{n+1} + (\psi_{i+1,j}^{n+1} - \psi_{i-1,j}^{n+1})\mathbf{E}\psi_{i,j}^n\right), \tag{3.12}$$

$$i = 2,\ldots,N_r - 1, \quad j = 2,\ldots,N_z - 1.$$

Equations (3.11)–(3.12) are supplement by the boundary conditions in the following form

$$\frac{\psi_{2,j}^{n+1} + \psi_{1,j}^{n+1}}{2} = 0, \quad \frac{\psi_{2,j}^{n+1} - \psi_{1,j}^{n+1}}{h_r} = 0, \quad \frac{\psi_{N_r,j}^{n+1} + \psi_{N_r-1,j}^{n+1}}{2} = 0, \quad \frac{\psi_{N_r,j}^{n+1} - \psi_{N_r-1,j}^{n+1}}{h_r} = 0,$$

$$j = 1,\ldots,N_z, \tag{3.13}$$

$$\frac{\psi_{i,2}^{n+1} + \psi_{i,1}^{n+1}}{2} = 0, \quad \frac{\psi_{i,2}^{n+1} - \psi_{i,1}^{n+1}}{h_z} = 0, \quad \frac{\psi_{i,N_z}^{n+1} + \psi_{i,N_z-1}^{n+1}}{2} = 0, \quad \frac{\psi_{i,N_z}^{n+1} - \psi_{i,N_z-1}^{n+1}}{h_z} = 0,$$

$$i = 1,\ldots,N_r.$$

To represent equations (3.11)–(3.13) as a linear system with a banded matrix, equations are reordered. First, two new indices according to the equations

$$k_{(i,j)} = 2(i-1)N_z + 2j - 1, \quad i = 1,\ldots,N_r,$$

$$m_{(i,j)} = 2(i-1)N_z + 2j = k_{(i,j)} + 1, \quad j = 1,\ldots,N_z$$

are introduced. Each node (i,j) of the grid Q_h associates with two indices $k_{(i,j)}$ and $m_{(i,j)}$. An index $k_{(i,j)}$ is odd and an index $m_{(i,j)}$ is even. It is easy to see that

$$k_{(i+1,j)} = k_{(i,j)} + 2N_z, \quad k_{(i,j+1)} = k_{(i,j)} + 2,$$

$$k_{(i-1,j)} = k_{(i,j)} - 2N_z, \quad k_{(i,j-1)} = k_{(i,j)} - 2, \tag{3.14}$$

and

$$m_{(i+1,j)} = m_{(i,j)} + 2N_z, \quad m_{(i,j+1)} = m_{(i,j)} + 2,$$

$$m_{(i-1,j)} = m_{(i,j)} - 2N_z, \quad m_{(i,j-1)} = m_{(i,j)} - 2. \tag{3.15}$$

Let σ_k represents $\psi_{i,j}$ and $\sigma_m(= \sigma_{k+1})$ represents $\Phi_{i,j}$. Substituting σ_k instead $\psi_{i,j}$ and substituting σ_m instead $\Phi_{i,j}$ into equations (3.11)–(3.13), the algebraic system

can be recast as the following

$$\frac{\sigma_k^{n+1} - \sigma_k^n}{\tau} - \frac{1}{8r_i h_r h_z}\left(\left(\sigma_{k+2N_z}^n - \sigma_{k-2N_z}^n\right)\left(\sigma_{k+2}^{n+1} - \sigma_{k-2}^{n+1}\right) + \left(\sigma_{k+2N_z}^{n+1} - \sigma_{k-2N_z}^{n+1}\right)\right.$$

$$\left.\left(\sigma_{k+2}^n - \sigma_{k-2}^n\right)\right) + \frac{1}{2h_z}\left(\sigma_{k+1}^{n+1} - \sigma_{k-3}^{n+1}\right) = \frac{1}{2}\left(\mathbf{E}\sigma_k^{n+1} + \mathbf{E}\sigma_k^n\right),$$

$$(3.16)$$

$$\mathbf{E}\sigma_m^{n+1} = \frac{1}{r_i}\left((J_{i,j})^2 + \frac{1}{4h_z^2}(\sigma_{m+1}^n - \sigma_{m-3}^n)(\sigma_{m+1}^{n+1} - \sigma_{m-3}^{n+1})\right)$$

$$+ \frac{1}{r_i}\left(\frac{(\sigma_{m+2N_z-1}^n - \sigma_{m-2N_z-1}^n)}{2h_r}\mathbf{E}\sigma_{m-1}^{n+1} + \frac{(\sigma_{m+2N_z-1}^{n+1} - \sigma_{m-2N_z-1}^{n+1})}{2h_r}\mathbf{E}\sigma_{m-1}^n\right).$$

$$(3.17)$$

Boundary conditions (3.13) can be recast as following

$$\frac{\sigma_k^{n+1} + \sigma_{k+2N_z}^{n+1}}{2} = 0, \quad \frac{\sigma_{m+2N_z-1}^{n+1} - \sigma_{m-1}^{n+1}}{h_r} = 0, \ i = 1, j = 1, \dots, N_z, \quad (3.18)$$

$$\frac{\sigma_k^{n+1} + \sigma_{k-2N_z}^{n+1}}{2} = 0, \quad \frac{\sigma_{m-1}^{n+1} - \sigma_{m-2N_z-1}^{n+1}}{h_r} = 0, \ i = N_r, j = 1, \dots, N_z, \quad (3.19)$$

$$\frac{\sigma_k^{n+1} + \sigma_{k+2}^{n+1}}{2} = 0, \quad \frac{\sigma_{m+1}^{n+1} - \sigma_{m-1}^{n+1}}{h_z} = 0, \qquad j = 1, i = 1, \dots, N_r, \quad (3.20)$$

$$\frac{\sigma_k^{n+1} + \sigma_{k-2}^{n+1}}{2} = 0, \quad \frac{\sigma_{m-1}^{n+1} - \sigma_{m-3}^{n+1}}{h_z} = 0, \qquad j = N_z, i = 1, \dots, N_r, \quad (3.21)$$

where

$$E\sigma_k = \frac{(\sigma_{k+2N_z} - 2\sigma_k + \sigma_{k-2N_z})}{h_r^2} - \frac{(\sigma_{k+2N_z} - \sigma_{k-2N_z})}{2r_i h_r} + \frac{(\sigma_{k+2} - 2\sigma_k + \sigma_{k-2})}{h_z^2}.$$

Equations (3.18)–(3.21) are an approximation of the boundary conditions $\psi = 0$ and $\frac{\partial \psi}{\partial n} = 0$ at boundaries $r = \frac{\eta}{1-\eta}$, $r = \frac{1}{1-\eta}$, $z = 0$ and $z = \Gamma$. According to this representation, the linear system of a coupled formulation of the $\psi - \Phi$ problem can then be written as

$$B_{l-2N_z-1}\sigma_{l-2N_z-1}^{n+1} + B_{l-2N_z}\sigma_{l-2N_z}^{n+1} + B_{l-3}\sigma_{l-3}^{n+1} + B_{l-2}\sigma_{l-2}^{n+1} + B_{l-1}\sigma_{l-1}^{n+1} + B_l\sigma_l^{n+1} +$$

$$B_{l+1}\sigma_{l+1}^{n+1} + B_{l+2}\sigma_{l+2}^{n+1} + B_{l+2N_z-1}\sigma_{l+2N_z-1}^{n+1} + B_{l+2N_z}\sigma_{l+2N_z}^{n+1} + B_{l+2N_z+1}\sigma_{l+2N_z+1}^{n+1} = F_l,$$

$$(3.22)$$

where $l = 1, \dots, 2N_z N_r$. The matrix of system (3.22) has upper and lower band widths $2N_z + 1$. The standard subroutines DGBSV and DGBSVX of the LAPACK

are used to compute the solution of linear system (3.22). The matrix of this system is singular to working precision (as shown by DGBSVX the reciprocal condition number is zero). To make numerically nonsingular algebraic system , use of modification of the matrix is made. A small perturbation in the equations (3.20)–(3.21)is induced, which approximate the boundary conditions $\frac{\partial \psi}{\partial n} = 0$ at boundaries $z = 0$ and $z = \Gamma$. Now, boundary conditions are as follow

$$
\begin{aligned}
\frac{\sigma_k^{n+1} + \sigma_{k+2N_z}^{n+1}}{2} = 0, && \frac{\sigma_{m+2N_z-1}^{n+1} - \sigma_{m-1}^{n+1}}{h_r} = 0, \\
\frac{\sigma_k^{n+1} + \sigma_{k-2N_z}^{n+1}}{2} = 0, && \frac{\sigma_{m-1}^{n+1} - \sigma_{m-2N_z-1}^{n+1}}{h_r} = 0, \\
\frac{\sigma_k^{n+1} + \sigma_{k+2}^{n+1}}{2} = 0, && \frac{\sigma_{m+1}^{n+1} - \sigma_{m-1}}{h_z} = -\varepsilon\sigma_m^{n+1}, \\
\frac{\sigma_k^{n+1} + \sigma_{k-2}^{n+1}}{2} = 0, && \frac{\sigma_{m-1}^{n+1} - \sigma_{m-3}^{n+1}}{h_z} = -\varepsilon\sigma_m^{n+1}.
\end{aligned}
\tag{3.23}
$$

The effect of a small parameter ε to changes of a condition number of the matrix and relative output error are studied. Figure 3.3 shows the log-plot of the condition number (as computed by the routing DGBSVX of the LAPACK) versus the parameter $1/\varepsilon$. It is interesting to point out that, for a considered range of $\varepsilon \in [10^{-4}, 10^{-14}]$, an estimate of a relative error (as computed by DGBSVX) was of order 10^{-300}. In the next paragraph, influences of a parameter ε on a solution of a problem of the Taylor-Couette flow which is studied experimentally and numerically in Abshagen et al. (2004) will be studied.

3.4   Numerical example

3.4.1   Structure of two-cell flows

The Taylor-Couette flow provides opportunities for detailed comparison between the results of experimental and numerical investigations. In Abshagen et al. (2004) sufficiently complete results are presented from a combined numerical and ex-
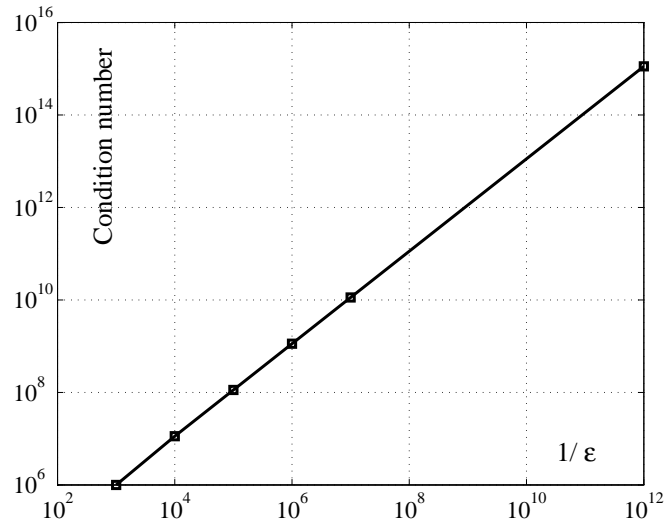
Figure 3.3 Condition number versus $1/\varepsilon$ as computed by DGESVX.

perimental studies of a steady bifurcation phenomena in a modified Taylor-Couette geometry where the end plates of flow domain are allowed to rotate independently from the inner cylinder.

The computation results for the case $\eta = \dfrac{R_i}{R_o} = 0.5, Re = 80$ and $\Gamma = 2$ are represented in Figure 3.1. A stream line plot in the (r, z) plane is shown in the first row of figures. The bottom row represents isolines of the function Φ. These flow configurations has arisen by continuous increase in the Reynolds number from zero. The patterns of stream line are in excellent agreement with results of Abshagen et al. (2004). As mention in Abshagen et al. (2004) when $\Omega = 0$, the flow state is characterized by inward flow adjacent to both end plates and return outward flow toward the outer cylinder in a narrow jet at the axial mid-plane. If the end plates co-rotating with inner cylinder ($\Omega = 1$), a different flow configuration appears when the Reynolds number is increased from zero. The direction of flow is opposite to that in the case of $\Omega = 0$. When the rotation rate of the end plates was increased from zero to one ($\Omega = 1$), two different flow pattern mutated smoothly into each other

by varying the rotation rate of the end plates Ω. The computational experiments shown that flow pattern changed in the range of Ω between 0.3 and 0.32 which are agreed with Abshagen et al. (2004). Flow patterns in Figure 3.4 are in a good agreement with the flow pattern in Abshagen et al. (2004) for the same parameters. The maximum values of the stream function are given in Table 3.1. A choice of these values is governed by the data available in Abshagen et al. (2004). This table shows that the scheme gives the same data as in Abshagen et al. (2004).

Table 3.1 Comparison of ψ_{max}/Re for the values $\Omega = 0$, 0.3, 0.304, 0.32, 1 and $Re = 80$, $\Gamma = 2$.

Ω	0	0.3	0.304	0.32	1
Present (42×82)	0.04257	0.00855	0.00584	0.01636	0.10010
Abshagen	0.04270	0.00869	0.00578	0.01667	0.10014

A comparison of Table 3.1 demonstrates that numerical model based on equations (3.3)–(3.5) is in close agreement with computational and experimental data Abshagen et al. (2004).
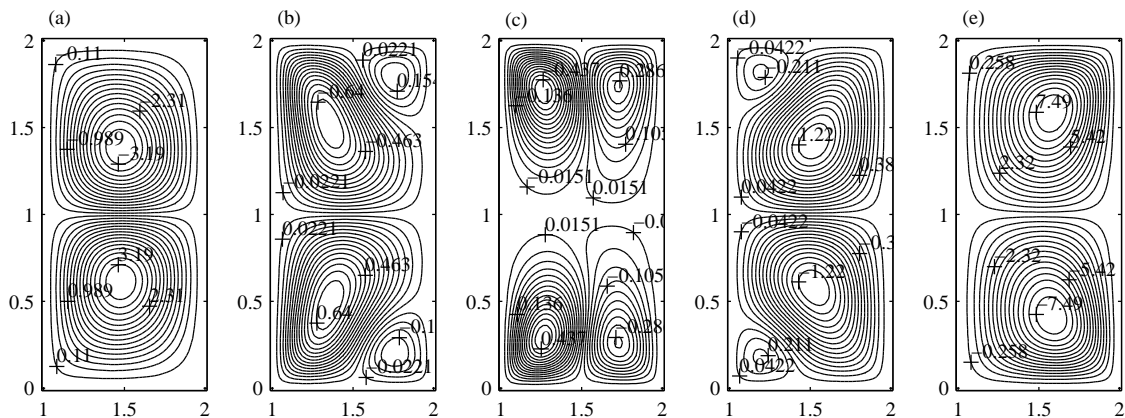
Figure 3.4 Contour plots of the stream function ψ at $\Gamma = 2$ and $Re = 80$.
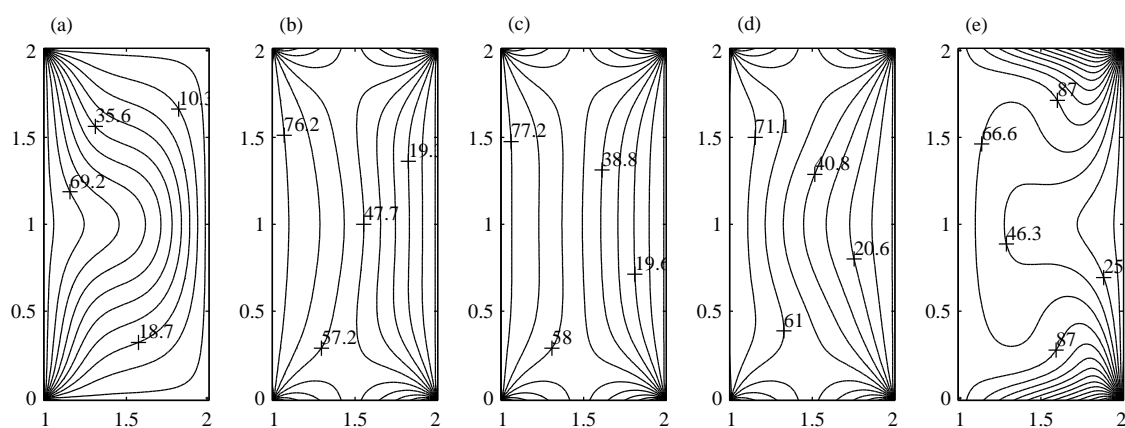
Figure 3.5 Contour plots of the function J at $\Gamma = 2$ and $Re = 80$.
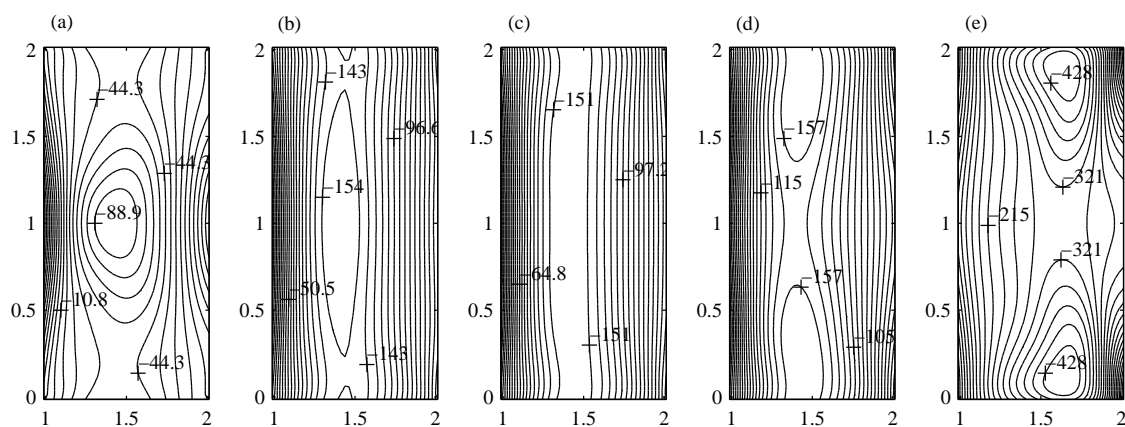
Figure 3.6 Contour plots of the function Φ at $\Gamma = 2$ and $Re = 80$.
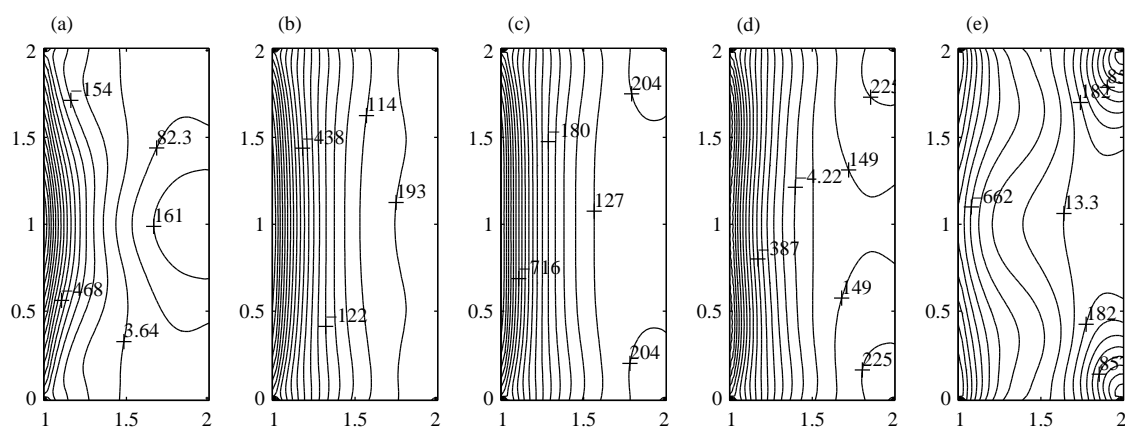
Figure 3.7 Contour plots of the pressure P at $\Gamma = 2$ and $Re = 80$.
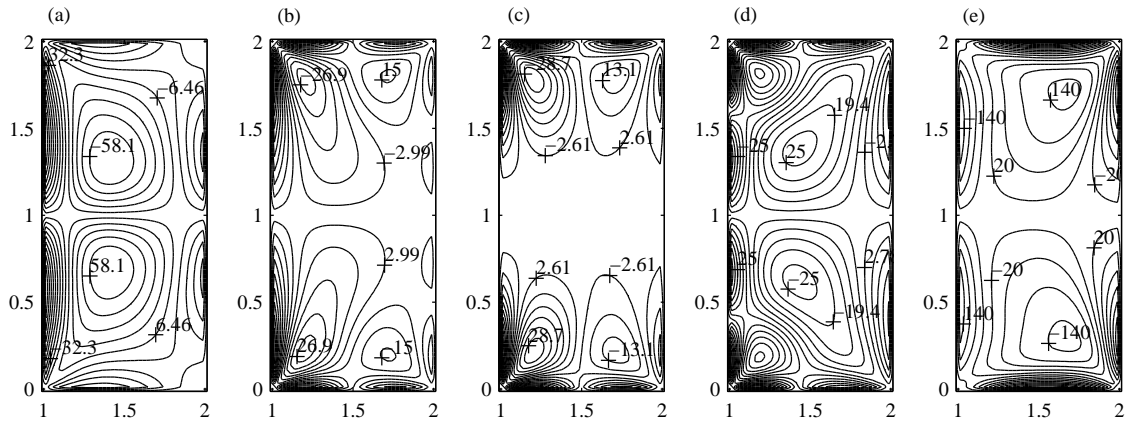
Figure 3.8 Contour plots of the vorticity at $\Gamma = 2$ and $Re = 80$.

To evaluate grid dependence on spatial variables the solution obtained on a sequence of grids with 12×22, 22×42, and 42×82 nodes. To estimate rate of convergence, the validity of expression

$$f_e \approx f_h + Ch^{\alpha} \tag{3.24}$$

is accepted where f_e and f_h are quantities related to an exact and computed solutions, respectively. Coefficients C and α independent of h. Since given solutions on three grids equation (3.24) can be solved for three unknowns f_e, C, and α. In Tables 3.2–3.4 ψ_{max}^h, Φ_{max}^h, and J_{max}^h were computed maximum values of the stream function ψ, new function Φ, and function J, respectively. Parameters α_ψ, α_Φ, and α_J, correspond to rate of convergence received from equation (3.24). Indices ψ, Φ, and J point out that maximum value of the stream function ψ, maximum value Φ, or maximum value J used in equation (3.24) instead f, respectively. In all cases represented in Tables 3.2–3.4 the flow is steady Abshagen et al. (2004). The solutions are qualified as steady when the relative error between two time steps which is less than 10^{-6} on a significant time interval

$$\frac{\max_{i,j} \left| f_{i,j}^{n+1} - f_{i,j}^n \right|}{\max_{i,j} \left| f_{i,j}^{n+1} \right|} \leqslant 10^{-6}$$

where $f_{i,j} = \{\sigma_{i,j}, \ J_{i,j}\}$.

Table 3.2 Results from a simulation on grid sequence and maximum values of the stream function at $Re = 80$.

Ω	$M_r \times N_z$	$h_r = h_z$	ψ_{max}^h	ε_ψ	α_ψ
0	12×22	0.1	3.20003	0.212157	2.53377
	22×42	0.05	3.37555	0.036637	
	42×82	0.025	3.40586	0.006327	
0.30	12×22	0.1	0.475481	0.224815	1.88292
	22×42	0.05	0.639341	0.060955	
	42×82	0.025	0.683769	0.016527	
0.304	12×22	0.1	0.430896	0.045125	1.17625
	22×42	0.05	0.456053	0.019968	
	42×82	0.025	0.467185	0.008836	
0.32	2×22	0.1	0.993318	0.343278	1.81581
	22×42	0.05	1.23909	0.097506	
	42×82	0.025	1.30890	0.027696	
1	12×22	0.1	7.80202	0.212172	2.53090
	22×42	0.05	7.97748	0.036712	
	42×82	0.025	8.00784	0.006352	

Table 3.3 Results from a simulation on grid sequence and maximum values of the function Φ at $Re = 80$.

Ω	$M_r \times N_z$	$h_r = h_z$	Φ^h_{max}	ε_Φ	α_Φ
0	12×22	0.1	175.920	82.3162	1.08608
	22×42	0.05	132.378	38.7742	
	42×82	0.025	111.868	18.2642	
0.30	12×22	0.1	140.289	102.198	0.974381
	22×42	0.05	90.1057	52.0143	
	42×82	0.025	64.5645	26.4731	
0.304	12×22	0.1	137.050	106.815	1.09096
	22×42	0.05	80.3790	50.1442	
	42×82	0.025	53.7749	23.5401	
0.32	2×22	0.1	123.901	105.662	1.08790
	22×42	0.05	67.9472	49.7085	
	42×82	0.025	41.6239	23.3852	
1	12×22	0.1	335.942	331.660	1.08564
	22×42	0.05	160.554	156.272	
	42×82	0.025	77.9144	73.6326	

Table 3.4 Results from a simulation on grid sequence and maximum values of the function J at $Re = 80$.

Ω	$M_r \times N_z$	$h_r = h_z$	J_{max}^h	ε_J	α_J
0	12×22	0.1	119.675	0.094704	2.89812
	22×42	0.05	119.686	0.083704	
	42×82	0.025	119.768	0.001704	
0.30	12×22	0.1	137.882	6.06125	1.05748
	22×42	0.05	141.031	2.91225	
	42×82	0.025	142.544	1.39925	
0.304	12×22	0.1	138.788	6.60877	1.41176
	22×42	0.05	142.896	2.50077	
	42×82	0.025	144.440	0.95677	
0.32	2×22	0.1	146.941	6.63921	1.04834
	22×42	0.05	150.370	3.21021	
	42×82	0.025	152.028	1.55221	
1	12×22	0.1	456.634	25.3367	0.871270
	22×42	0.05	468.120	13.8507	
	42×82	0.025	474.399	6.27900	

Table 3.5 Effect of parameter ε on numerical solutions (grid- 22×42).

Ω	ε	ψ_{min}	ψ_{max}	Φ_{min}	Φ_{max}	J_{min}	J_{max}
0	10^{-2}	-3.68293	3.68293	-87.1066	142.977	-39.9864	120.014
	10^{-6}	-3.37560	3.37560	-96.6644	132.361	-40.3143	119.686
	10^{-8}	-3.37555	3.37555	-96.6659	132.378	-40.3144	119.686
	10^{-10}	-3.37555	3.37555	-96.6612	132.477	-40.3144	119.686
	10^{-14}	-3.37555	3.37555	-95.6708	140.492	-40.3144	119.688
1	10^{-2}	-6.53545	6.53545	-322.564	110.315	-150.655	473.445
	10^{-6}	-7.97720	7.97720	-425.924	160.543	-155.978	468.122
	10^{-8}	-7.97748	7.97748	-425.944	160.554	-155.980	468.120
	10^{-10}	-7.97748	7.97748	-425.947	160.573	-155.980	468.120
	10^{-14}	-7.97748	7.97748	-422.439	190.444	-155.980	468.120
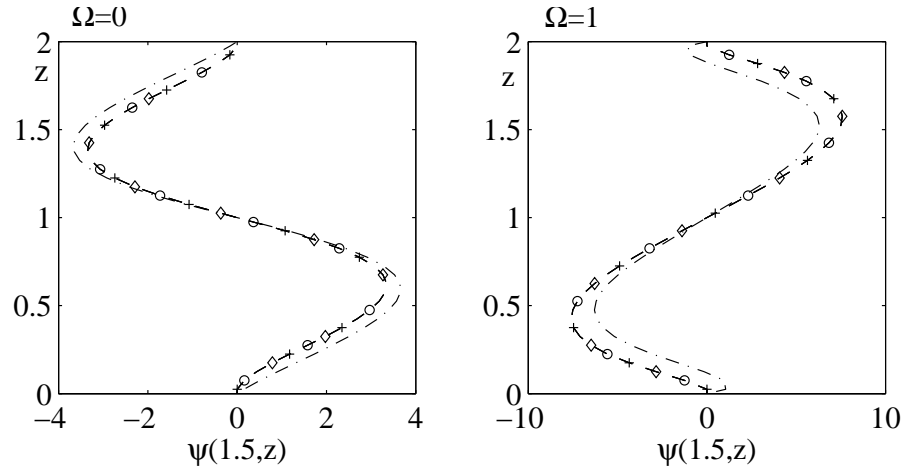
Figure 3.9 Effect of ε for $Re = 80, \eta = 0.5$, and $\Gamma = 2$. $- \cdot - \varepsilon = 10^{-2}$; $- \diamond - \varepsilon = 10^{-6}$; $- \circ - \varepsilon = 10^{-10}$; $- + - \varepsilon = 10^{-14}$.

Figure 3.10 Effect of ε on the 'exact' calculated boundary values of Φ for $Re = 80, \eta = 0.5$, $\Gamma = 2$ and $\Omega = 0$. (a)-(c) $\Phi(1, z)$, $\Phi(2, z)$, and $\Phi(r, 0) = \Phi(r, 2)$, respectively, $- \cdot - \varepsilon = 10^{-2}$; $- \diamond - \varepsilon = 10^{-6}$; $- \circ - \varepsilon = 10^{-10}$; $\underline{\hspace{1cm}} \varepsilon = 10^{-14}$.

Computational was carried out on a personal computer with 2.4 GHz CPU and the CPU-time per one time step (/one iteration) on the grid 22×42 was about 0.31989 sec.

Next, some numerical experimental results related with effect of ε on the solution will be shown. If the problems (3.16), (3.17), and (3.23) are solved by different ε, results listed in Table 3.5 are found, where dependence on ε of the maximal and minimal components of the solution are represented. Variations of ε in the range $10^{-6} - 10^{-10}$ have no significant influence on quantities shown in Table 3.5. Values $\varepsilon < 10^{-14}$ correspond to reciprocal condition number less than computer accuracy (as computed by DGBSVX). Figure 3.9 shows values of stream function versus z for $r = 1.5$ and $\Omega = 0$ and 1, ε varies from 10^{-2} to 10^{-14}. Figures 3.10 and 3.11 show the values of Φ at domain boundaries. One can observe that if $10^{-10} \leq \varepsilon \leq 10^{-6}$ the variations of Φ at boundaries are negligible. If ε too small, $\varepsilon \leq 10^{-12}$, Φ oscillates near 'correct' computed values. It is interesting to note that more significant oscillations were observed only at boundary of internal rotating cylinder ($r = 1$). One can see that for $\varepsilon \in [10^{-14}, 10^{-6}]$ values of the stream function change less than 1%.

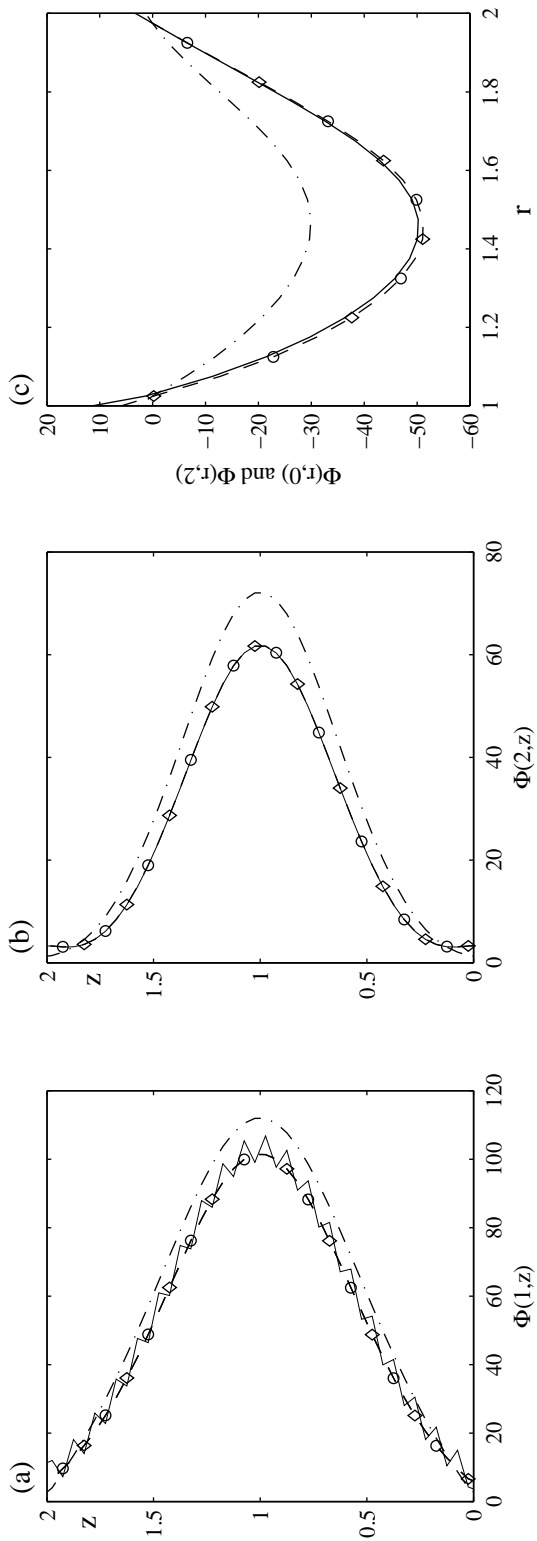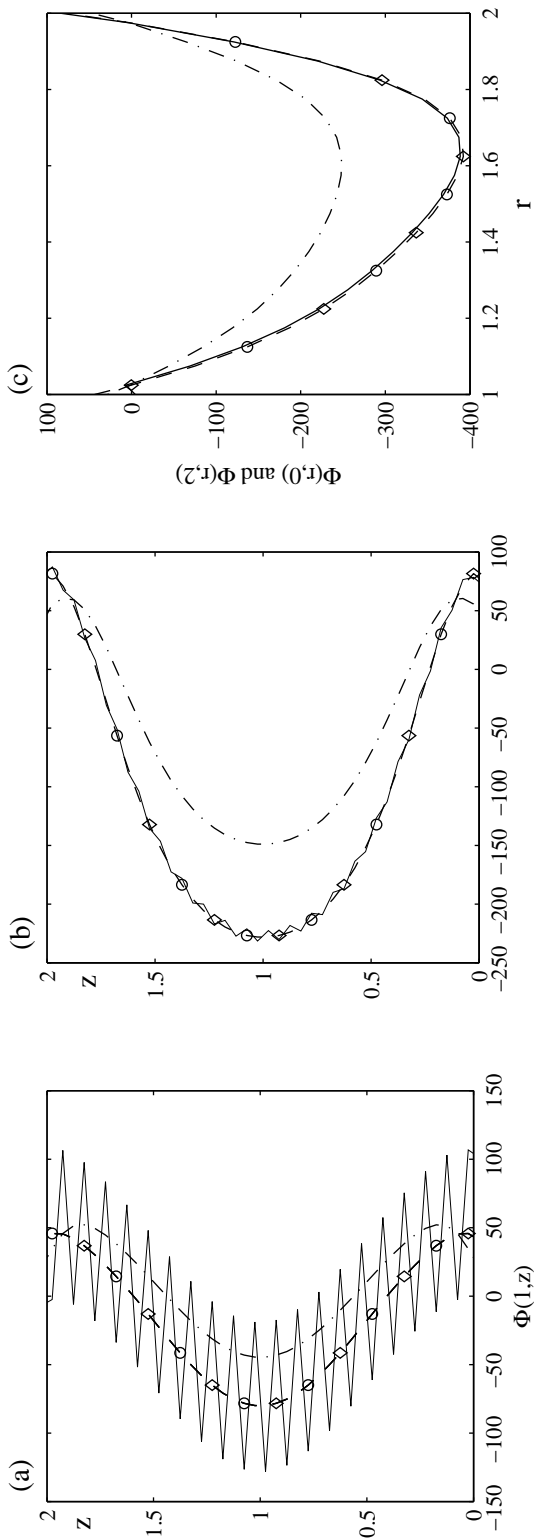**Figure 3.11** Effect of ε on the 'exact' calculated boundary values of Φ for $Re = 80, \eta = 0.5$, $\Gamma = 2$ and $\Omega = 1$. (a)-(c) $\Phi(1, z)$, $\Phi(2, z)$, and $\Phi(r, 0) = \Phi(r, 2)$, respectively, $- \cdot - \varepsilon = 10^{-2}$; $- \cdot - \varepsilon = 10^{-6}$; $- \diamond - \varepsilon = 10^{-10}$; $- \circ - \varepsilon = 10^{-10}$; $\underline{\quad\quad} \varepsilon = 10^{-14}$.
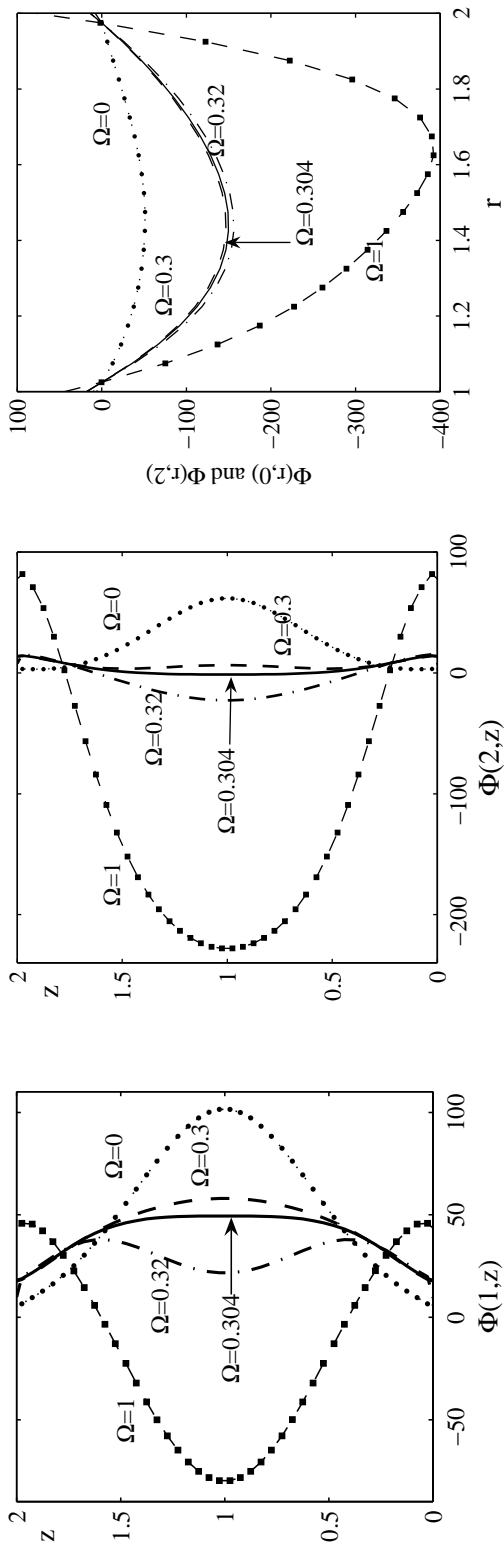
Figure 3.12 'Exact' calculated boundary values of Φ for $Re = 80, \eta = 0.5, \Gamma = 2$ and $\Omega = 0, 0.3, 0.304, 0.32, 1.0$. (a)-$\Phi(1,z)$; (b)-$\Phi(1,z)$; (c)- $\Phi(r,0)$ and $\Phi(r,2)$. $\cdots\cdots \Omega = 0$; $---\Omega = 0.30$; $\text{---}\Omega = 0.304$; $-\cdot-\cdot\Omega = 0.32$; $-\cdot\blacksquare\cdot-\Omega = 1$.

In order to illustrate the influence of rotation rate Ω on Φ distribution in more clear manner, computed boundary values of Φ for a range of Ω is shown in Figure 3.12. The surface plots of $\Phi(r, z)$ for $\Omega = 0,\ 0.3,\ 0.32,$ and 1 are displayed in Figure 3.13. It is noted that first that $\Phi(r, 0) = \Phi(r, 2)$, e.g., boundary values of Φ on top and bottom covers the same. Figure 3.12 shows 'correct' computed boundary values at $r = 1$ and $r = 2$ of Φ for different control parameter Ω. In the case $\Omega = 0$ (the end plates do not rotate) function Φ has positive maximum at the middle of domain $z = 1$, if $\Omega = 1$ (the end plates rotate synchronically with internal cylinder) Φ has negative extremum. Probably these have relation with direction of flow at $z = 1$.

Figure 3.13 Surface plots of calculated Φ for $\Omega = 0, 0.3, 0.32, 1.0$, $Re = 80, \eta = 0.5$, and $\Gamma = 2$.

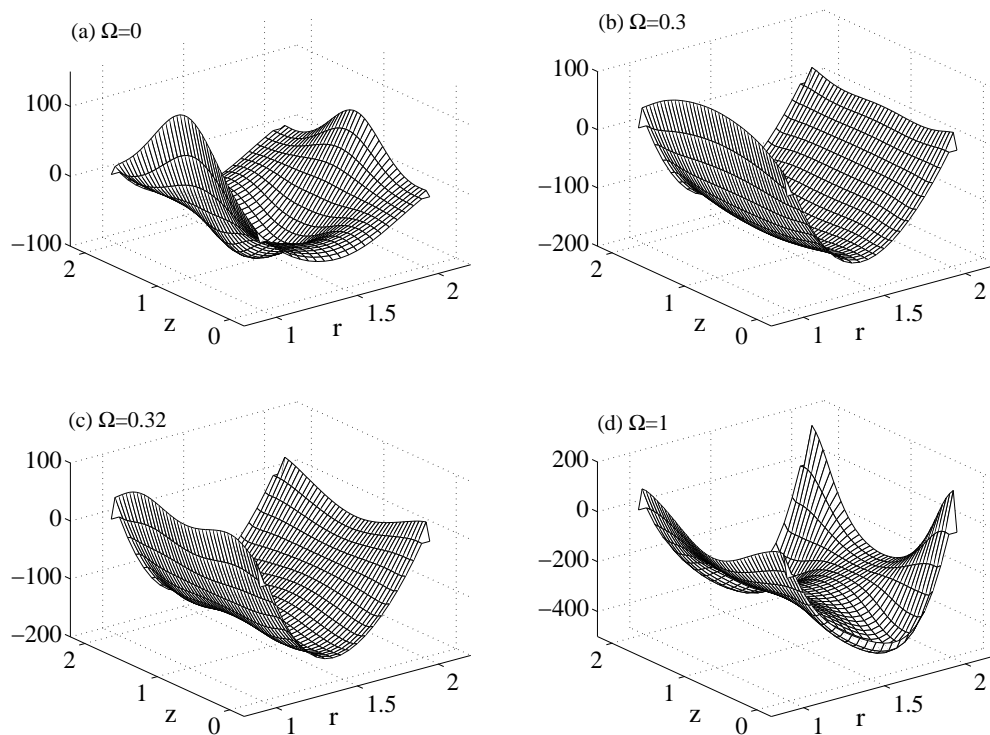## 3.4.2 Exchange process between one- and three-cell flows as a function of Re and Γ

In the case where both end walls rotate only states with even number of vortices are observed. Experimental and numerical study of the flow in a Taylor-Couette system with the bottom end plate attached to the inner cylinder and other stationary was considered in Mullin and Blohm (2001), Lopez, Marques, and Shen (2004). In Mullin and Blohm (2001) (as can seen in Figure 3.14) observations were generally made by varying the Reynolds number at fixed values of the aspect ratio. Re was increased or decreased in small steps of around 1% and left for a some time to allow transient behavior to decay. It has been observed in Mullin and Blohm (2001) that at an aspect ratio of the increasing Re led to the initial development of a steady three-cell flow which then collapsed to a single-cell state at a critical value of Re via a saddle-node bifurcation. The algorithm is utilized to compute a 'typical' sequence of states in case represented in Mullin and Blohm (2001). Aspect ratio fixed $\Gamma = 3.226$, Re was increased in small step by the formulae $Re = Re_0(1 - exp(-0.05(n - 1)))$, where n is the number of time step. The two steady states with two and three vortices are shown in Figure 3.15. At a Re_0 of approximately 75 a definite three-cell state is established. This state is shown in Figure 3.15 (a). When Re_0 is increased to approximately 312 the cell adjacent to the rotating bottom grows at the expense of the other two cells. This situation can be seen in Figure 3.15 (b). Further increase of Re_0 to approximately 350 leads to the collapse to a single-cell state. If Re is then reduced back (The simulation is started from state which corresponds to $Re_0 = 350$) $Re = 350 - 38.4(1 - exp(-0.05(n - 1)))$ to approximately 312 then the single-cell shown in Figure 3.15 (c) is observed. The grid consisted of 32×62 nodes and time step was equal to 0.001. The results of our numerical experiments exactly corresponds to the case represented in Mullin

and Blohm (2001), where results of numerical simulations compared with results of physical experiments.
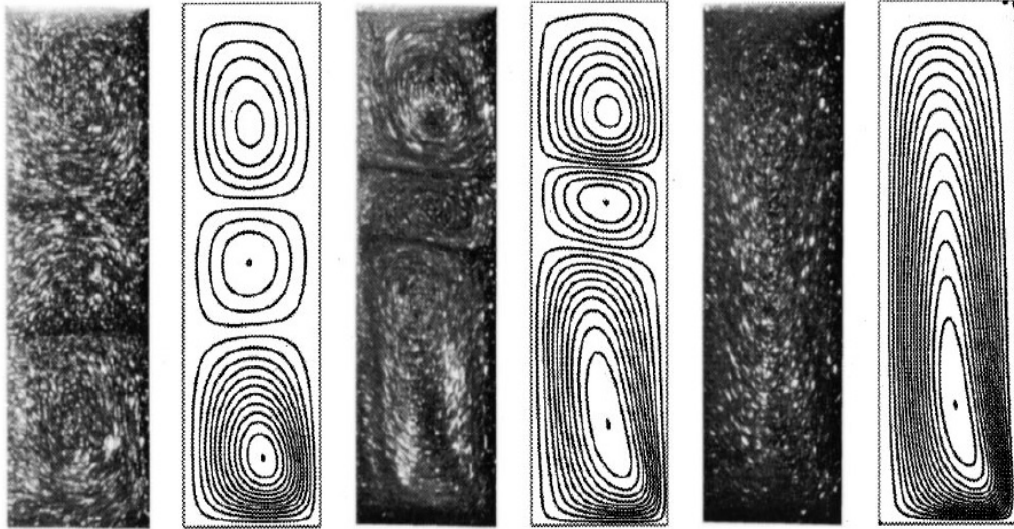
Figure 3.14 Sequence of flow pattern plots at $\Gamma = 3.226$ by Mullin and Blohm (2001). Three-cell at $Re = 75.3$. Three-cell at $Re = 257.9$. Single-cell at $Re = 311.6$.
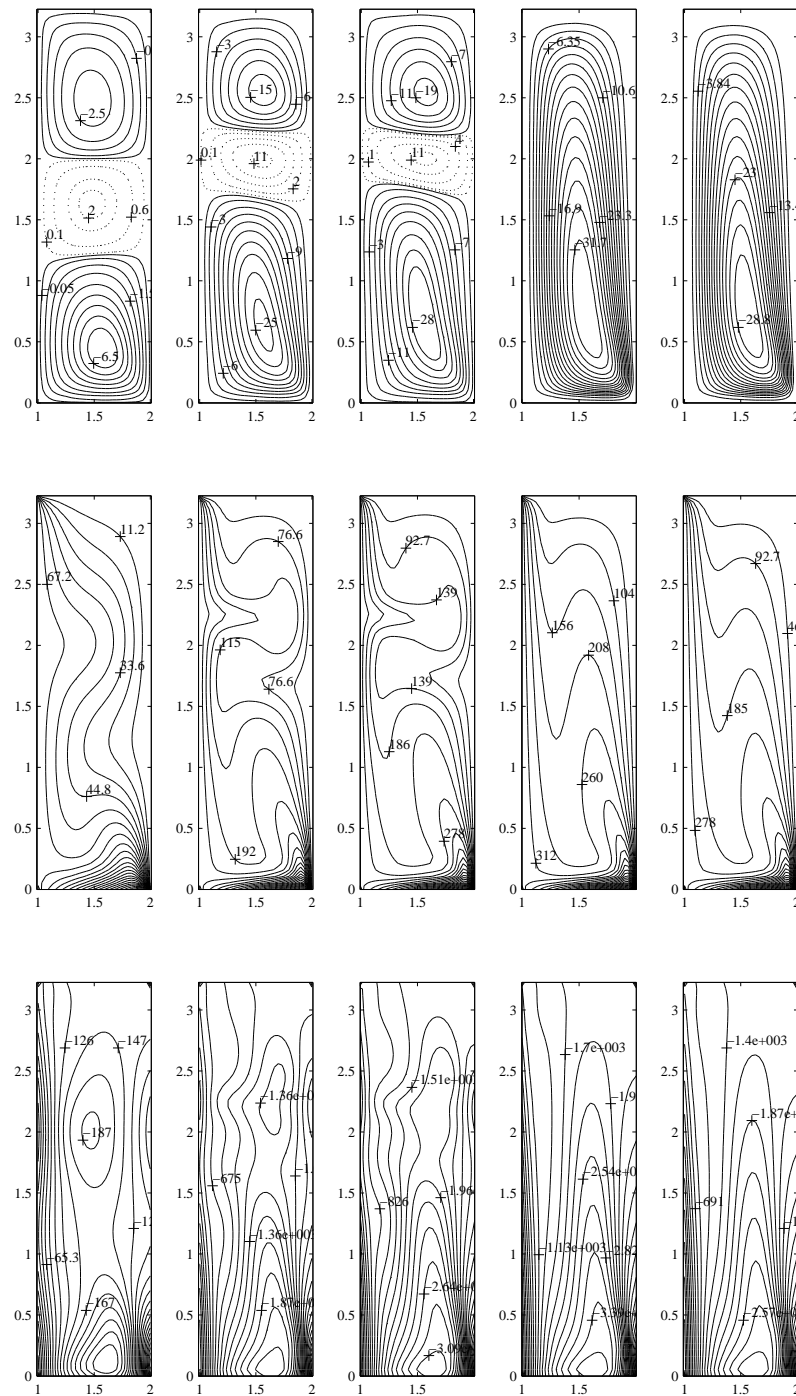
Figure 3.15 Sequence of flow pattern plots at $\Gamma = 3.226$. Three-cell at $Re = 75.3$. Three-cell at $Re = 257.9$. Three-cell at $Re = 311.6$. Single-cell at $Re = 350$. Single-cell at $Re = 312$. Streamlines ψ, function $J = rv$, and function Φ.

The dynamics of the flow in a short annulus driven by the rotation of the inner cylinder and bottom end wall is considered in Lopez, Marques, and Shen (2004). In this part, authors consider the parameter regime $Re \in [100, 200]$, $\Gamma \in [2.5, 3.25]$ and $\eta = 0.5$. In particular, they pointed out that for $Re = 100$ and low Γ, the flow consists of a single meridional cell, driven essentially by the rotation of the bottom end wall. As the length of the cylinders is increased (i.e., increasing Γ), at fixed Re, the rotating inner cylinder begins to play a more important role in the driving of the flow. Moreover, as Γ approaches 3, the flow undergoes a transition from the single meridional overturning cell structure to a three-cell structure with the middle cell counter-rotating (in the meridional plane) compared to the other two. At low Re, this transition from a one-cell state to a three-cell state is smooth and non-hysteretic.

Figure 3.16 Sequence of the steady axisymetric solutions for $Re = 100$ and Γ as indicated. $\Gamma = 2.00, 2.50, 2.70, 2.80, 2.81, 2.82, 2.85, 3.00$. Contour plots of the stream function ψ.

Figure 3.17 Sequence of the steady axisymmetric solutions for $Re = 100$ and Γ as indicated. $\Gamma = 2.00$, 2.50, 2.70, 2.80, 2.81, 2.82, 2.85, and 3.00. Contour plots of the function $J = rv$.
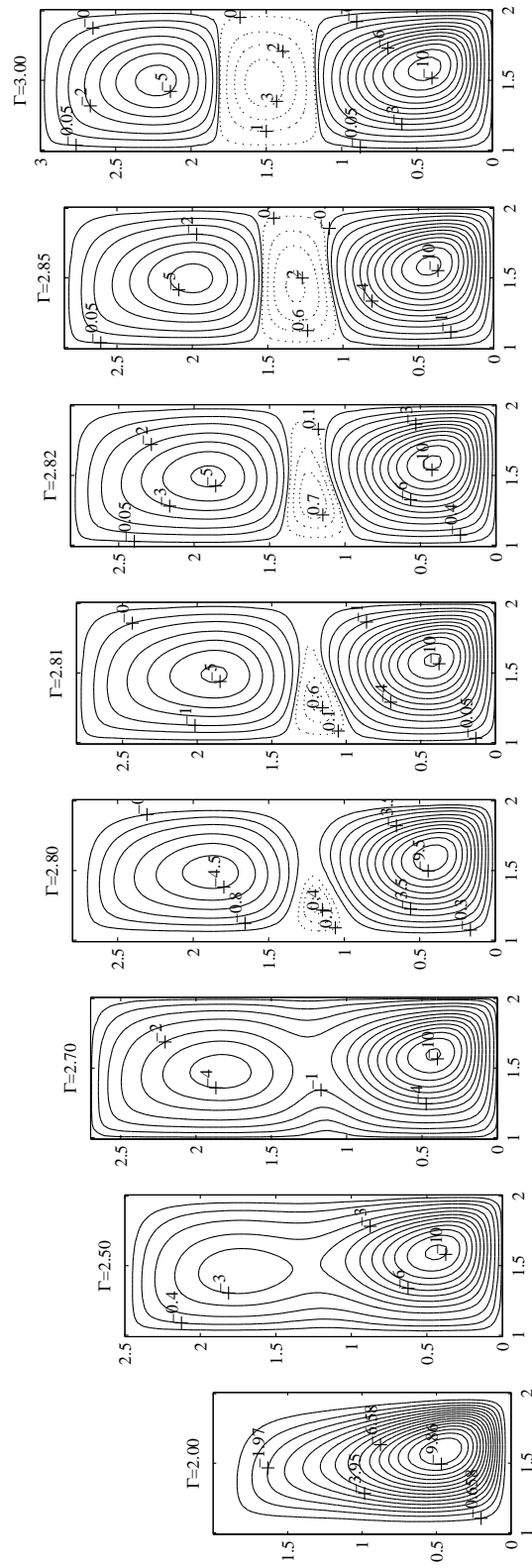
Figure 3.18 Sequence of the steady axisymmetric solutions for $Re = 100$ and Γ as indicated. $\Gamma = 2.00$, 2.50, 2.70, 2.80, 2.81, 2.82, 2.85, 3.00. Contour plots of the function Φ.
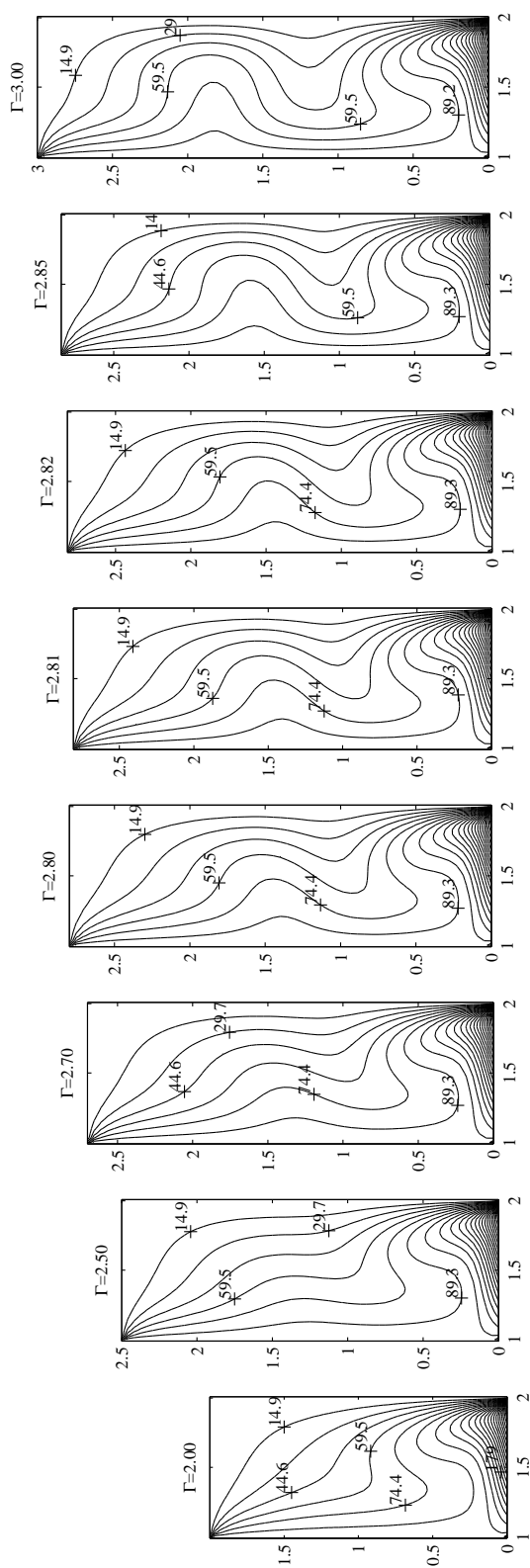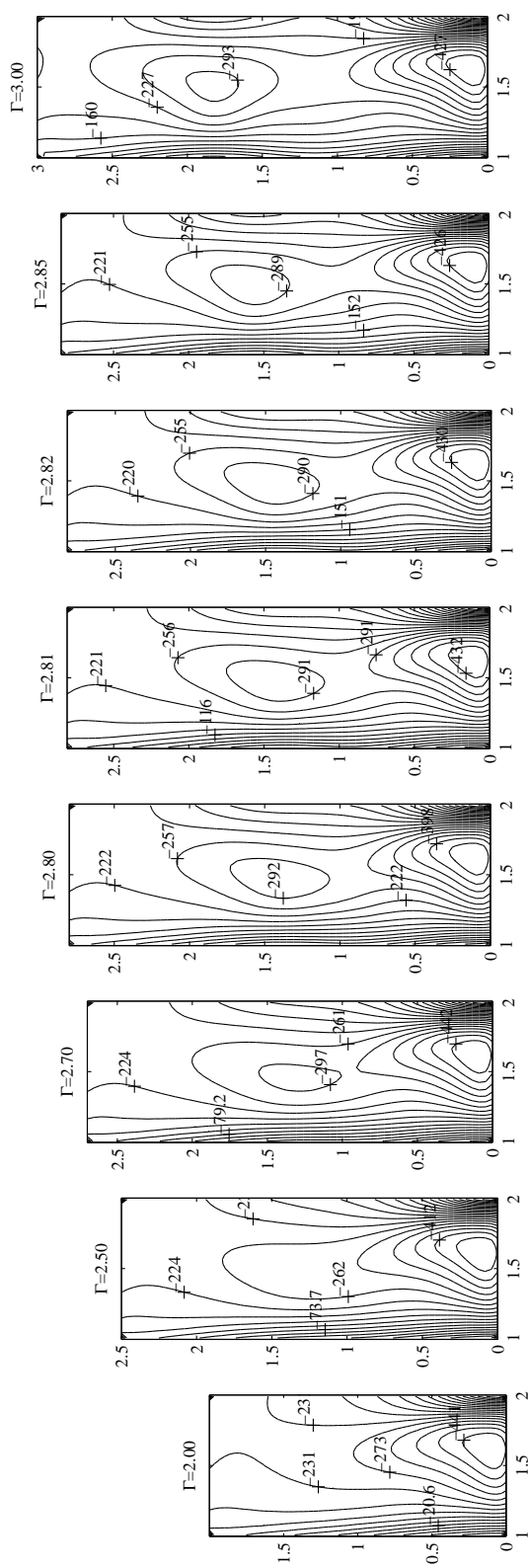
The results of numerical experiments are shown in Figures 3.16–3.18. Figures 3.16–3.18 shows the streamlines ψ, isolines of azimuthal velocity component $J = rv$, and isolines of Φ of the steady axisymmetric states, respectively, at $Re = 100$ as Γ is varied between 2.50 and 3.00. At Γ between about 2.7 and 2.8, the boundary layer on the rotating inner cylinder separates and a small weak separation bubble forms. The flow near the separation point advects flow with high angular momentum into the interior. As Γ is increased above 2.8, the separation bubble extends further into the interior, although its axial extent remains small. At about $\Gamma = 2.81$, the separation streamline extends to the stationary outer cylinder where it re-attaches; at the outer cylinder at slightly lower z the boundary layer also separates and attaches at the inner cylinder, and a three-cell state is established. With further increase in Γ, the weak middle cell strengthens and grows in axial extent, as seen in Figure 3.16(g) for $\Gamma = 3.00$. The numerical simulations of the axisymmetric short Taylor-Couette annulus flow are totaly consistent with scenario represented in Lopez, Marques, and Shen (2004).

The observation was focused on the exchange process between one and three-cell flows as a function of Re and Γ. The dependence of the size of the bottom driven vortex on Re for a range of aspect ratios Γ is plotted in Figure 3.19. Height of the cell as percentages of total height are plotted on the vertical axis. They were determined using numerical simulation. While Re was increased, the three-cell state appeared gradually until the bottom cell begin to shrink. Therefore, increasing of Re causes the growth of end-cell and collapse to a single cell state.
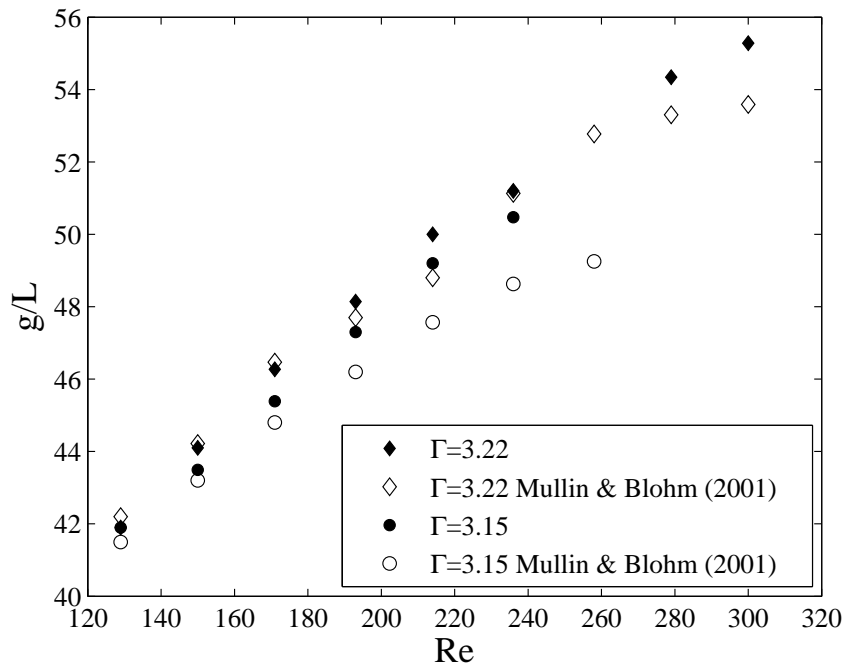
Figure 3.19 Cell size of the bottom vortex in a steady-cell state plotted as a function of Re for a various of Γ; height of the bottom cell g as percentage of the total height L of annulus is plotted on the vertical axis.

3.4.3 Taylor-Couette flow in a small aspect ratio

The dynamics of the Taylor-Couette flow in a small aspect ratio annulus (where the length of the cylinders is half of the annulus gap between them) is numerically investigated by Lopez and Marques (2003). In this paper, authors consider the dynamics of the flow which is driven by the inner cylinder only for $Re = 540$, $\eta = 0.675$, and $\Gamma = 0.5$. The results of numerical experiments in this dissertation are shown in Figure 3.20. The structure of this flow is clear from the contours of the angular momentum J and radial velocity component u. A two-cell counter-rotating meridional flow is formed to balance the fluid advected by the jet. These cells return swirling fluid back towards the inner cylinder along the stationary end walls, as shown by the
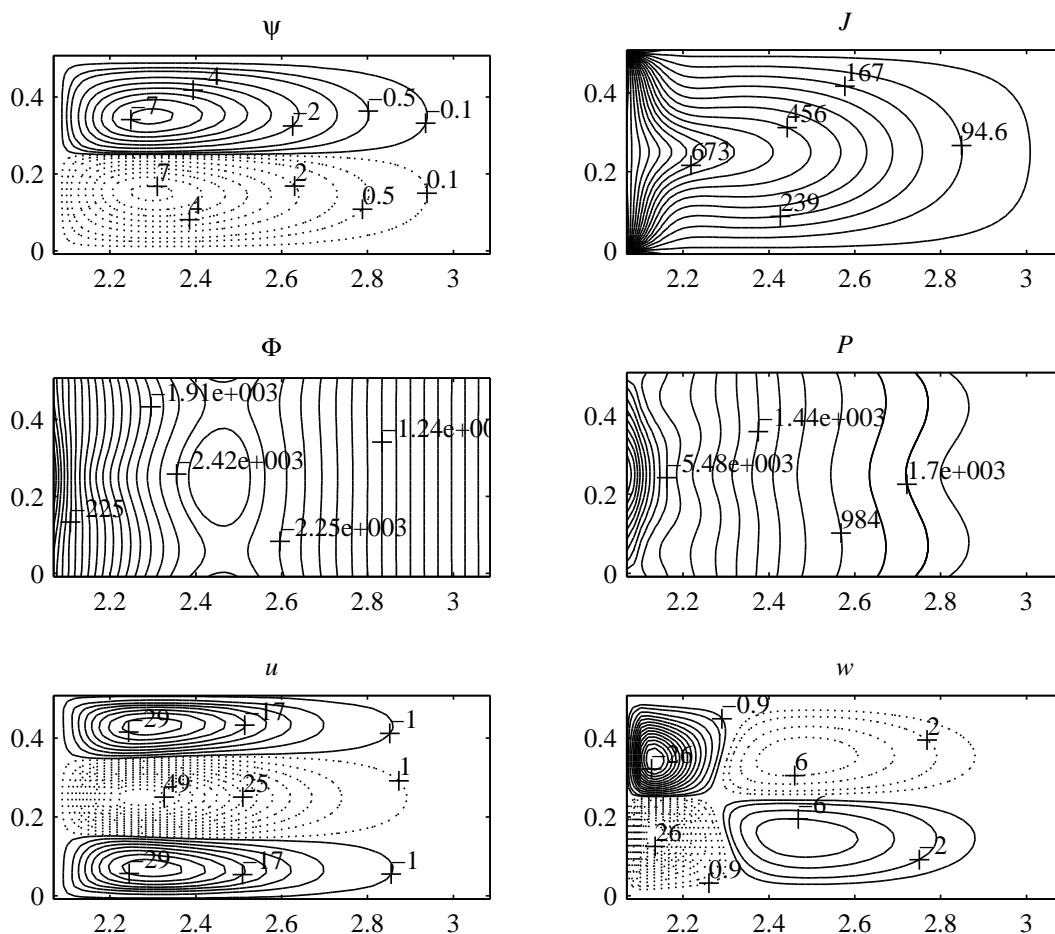
Figure 3.20 Contour plots at $\Gamma = 0.5$, $\eta = 0.675$, and $Re = 540$.

radial velocity u in part of Figure 3.20.

3.5   Conclusion

The new formulation for the axisymmetric Navier-Stokes flows proposed by Aristov and Pukhnachev (2004), is implemented numerically. The approximations for the different functions are staggered in time. Thus the equation for the azimuthal velocity component is decoupled from the rest of the equations and is approximated on fractional time steps. The equations for the stream function, ψ and the new unknown function of Aristov-Pukhnachev's formulation, Φ are considered as a coupled system at full time steps. The coupling for the latter system is crucial because of the lack

of boundary conditions for the new functions and the presence of two boundary conditions for the stream function. After special renumbering the grid points of hopscotch-type, the coupled system is formulated as a single system and solved by a LAPACK algorithm.

The main difficulty with this formulation is that the coupled system for ψ and Φ is singular. To avoid the singularity, part of the Neumann boundary conditions for the composite function are replaced by Robin boundary conditions with a small parameter multiplying the function. The result is that the originally infinite condition number of the system behaves as $1000\varepsilon^{-1}$ and even for very small $\varepsilon \propto 10^{-10}$, the Gaussian elimination is perfectly stable. The impact on the results of the actual value of the artificial small parameter is judiciously evaluated by numerical experiments and shown that for $\varepsilon \propto 10^{-6}$ the results are correct within six significant digits which is much better than the truncation error.

The new numerical model is applied to the flow between two rotating cylinders when the lids are also allowed to rotate. This particular Taylor-Couette flow exhibits a rich phenomenology depending on the relative rotations of the lids. This study shows that the new technique performs robustly and allows one to follow accurately the rearrangement of the flow patterns with the changes of the relative rotation of the lids, Ω. The results are in good quantitative agreement with Mullin and Blohm (2001), Abshagen et al. (2004), and Lopez, Marques, and Shen (2004) in the common ranges of the main parameters.

The present paper shows that the Aristov-Pukhnachev's formulation is a viable approach to the axisymmetric Navier-Stokes flows and can serve as a basis for efficient numerical models.

3.6   References

Aristov, S.N., and Pukhnachev, V.V. (2004). On the equations of axisymmetric motion of a viscous incompressible. **Doklady Physics** 49(2):112–115.

Abshagen, J., Cliffe, K.A., Langenberg, J., Mullin, T., Pfister, G., and Tavener, S.J. (2004). Taylor-Couette flow with independently rotating end plates. **Theoretical and Computational Fluid Dynamics** 18:129–136.

Brown, G.L., and Lopez, J.M. (1990). Axisymmetric vortex breakdown Part 2. Physical mechanisms. **Journal of Fluid Mechanics** 221:553–576.

Inamuro, T., Yamaguchi, A., and Ogino F. (1997). Fluid flow in a rotating cylindrical container with a rotating disk at the fluid surface. **Fluid dynamics research** 21:417–430.

Lopez, J.M. (1990). Axisymmetric vortex breakdown Part 1. Confined swirling flow. **Journal of Fluid Mechanics** 221:533–552.

Lopez, J.M., and Marques, F. (2003). Small aspect ratio Taylor-Couette: Onset of a very-low-frequency three-torus state. **Physical Review E** 68, 036302.

Lopez, J.M., Marques, F., and Shen, J. (2004). Complex dynamics in a short annular container with rotating botton and inner cylinder. **Journal of Fluid Mechanics** 501:327–354.

Lopez, J.M., and Perry, A.D. (1992). Axisymmetric vortex breakdown Part 3. Onset of pereodic flow and chaotic advection. **Journal of Fluid Mechanics** 234:449–471.

Mullin, T., and Blohm, C. (2001). Bifurcation phenomena in a Taylor-Couette flow with asymmetric boundary conditions. **Physics of Fluids** 13(1):136–140.

Mullin, T., Toya, Y., and Tavener, S.J. (2002). Symmetry breaking and multiplicity of states in small aspect ratio Taylor-Couette flow. **Physics of Fluids** 14(8):2778–2787.

Pfister, G., Schmidt, H., Cliffe, K.A., and Mullin, T. (1988). Bifurcation phenomena in Taylor-Couette flow in a very short annulus. **Journal of Fluid Mechanics** 191:1–18.

Taylor, G.I. (1923). Stability of a viscous liquid contained between two rotating cylinders. **Philosophical Transactions of the Royal Society A** 223:289–343.

Youd, A.J., and Barenghi, G.F. (2005). Reversing and nonreversing modulate Taylor-Couette flow at finite aspect ratio. **Physical Review E** 72:056231.

CHAPTER IV

FINITE DIFFERENCE METHOD FOR AXISYMMETRIC FLOW IN STREAM FUNCTION AND ANGULAR MOMENTUM FORM

As note before this chapter, the internal iteration method is reasonable to approximate solution of the NSEs in the stream function formulation. In this chapter, the results of numerical simulation of the Taylor-Couette flow by method of the internal iteration are compared with those obtained using numerical techniques developed for the new form of the NSEs.

4.1 Governing equations

The motion of an axisymmetric incompressible viscous fluid is governed by the NSEs (1.11)–(1.14). Let D be the characteristic length scale associated with the Taylor-Couette flow geometry. The following dimensionless variables: time, $t = \dfrac{t^*\nu}{D^2}$; space, $r = \dfrac{r^*}{D}$, $z = \dfrac{z^*}{D}$; and velocity, $v = \dfrac{v^*D}{\nu}$ are defined.

The axisymmetric NSEs for a swirling flow written in the stream function and angular momentum form using the cylindrical coordinates (r, θ, z) with corresponding the velocity components (u, v, w) are

$$J_t - \frac{1}{r}\psi_z J_r + \frac{1}{r}\psi_r J_z = \mathbf{E}J, \tag{4.1}$$

$$\frac{\partial \mathbf{E}\psi}{\partial t} + \frac{2}{r^2}\psi_z \mathbf{E}\psi - \frac{1}{r}\psi_z(\mathbf{E}\psi)_r + \frac{1}{r}\psi_r(\mathbf{E}\psi)_z + \frac{2}{r^3}JJ_z = \mathbf{E}^2\psi. \tag{4.2}$$

The main target of recent work is to develop and validate a finite-difference scheme to approximate solution of equations (4.1)–(4.2). Moreover, obtained solution is used to reconstruct a new unknown function in Aristov-Pukhnachev's form of the NSEs. Below, only the case where the no-slip conditions satisfied at the boundary of the flow domain will be considered. In terms of the functions ψ and J, these conditions are represented in the form

$$\frac{\partial \psi}{\partial n} = 0, \quad \psi = 0, \quad J = \Omega r^2, \tag{4.3}$$

where $\dfrac{\partial \psi}{\partial n}$ means derivative in the direction of the normal vector to the boundary, Ω is the rate of rotations of the boundary surface. To close the formulation of the problem it is necessary to specify the initial conditions

$$\psi = \psi_0(r, z), J = J_0(r, z), \quad t = 0. \tag{4.4}$$

4.2   Computational technique

Equations (4.1)–(4.2) hold in the region Q. The numerical treatment of these equations is based on the finite-difference method used to discreatize the $(r, z)-$region Q. To use the mesh staggered in $r-$direction on $0.5h_r$ and in $z-$direction on $0.5h_z$ with respect domain boundaries is used. Such grid allows one to use the central-differences to approximate boundary conditions with the second-order on two-point stencils. Technically, equation (4.1) is approximated as using the central finite-difference as follow:

$$
\begin{aligned}
\frac{J_{i,j}^{n+1/2} - J_{i,j}^{n-1/2}}{\tau} &= \frac{1}{8 r_i h_r h_z} \left(\psi_{i,j+1}^n - \psi_{i,j-1}^n \right) \left(J_{i+1,j}^{n+1/2} - J_{i-1,j}^{n+1/2} + J_{i+1,j}^{n-1/2} - J_{i-1,j}^{n-1/2} \right) \\
&\quad - \frac{1}{8 r_i h_r h_z} \left(\psi_{i+1,j}^n - \psi_{i-1,j}^n \right) \left(J_{i,j+1}^{n+1/2} - J_{i,j-1}^{n+1/2} + J_{i,j+1}^{n-1/2} - J_{i,j-1}^{n-1/2} \right) \\
&\quad + \frac{1}{2} \left(\mathbf{E} J_{i,j}^{n+1/2} + \mathbf{E} J_{i,j}^{n-1/2} \right), \quad i = 2, \ldots, N_r - 1, \quad j = 2, \ldots, N_z - 1,
\end{aligned}
$$

$$\tag{4.5}$$

where

$$\mathbf{E}J_{i,j} = \frac{(J_{i+1,j} - 2J_{i,j} + J_{i-1,j})}{h_r^2} - \frac{(J_{i+1,j} - J_{i-1,j})}{2r_i h_r} + \frac{(J_{i,j+1} - 2J_{i,j} + J_{i,j-1})}{h_z^2}. \quad (4.6)$$

Equation (4.5) are supplemented by the boundary conditions

$$\frac{J_{1,j}^{n+\frac{1}{2}} + J_{2,j}^{n+\frac{1}{2}}}{2} = Re\frac{\eta}{1-\eta}, \qquad \frac{J_{N_r-1,j}^{n+\frac{1}{2}} + J_{N_r,j}^{n+\frac{1}{2}}}{2} = 0, \ \ j = 1,\dots,N_z,$$

$$(4.7)$$

$$\frac{J_{i,1}^{n+\frac{1}{2}} + J_{i,2}^{n+\frac{1}{2}}}{2} = Re\Omega r_i^2 \frac{1-\eta}{\eta}, \qquad \frac{J_{i,N_z-1}^{n+\frac{1}{2}} + J_{i,N_z}^{n+\frac{1}{2}}}{2} = Re\Omega r_i^2 \frac{1-\eta}{\eta}, \ \ i = 1,\dots,N_r.$$

The system of algebraic equations (4.5)–(4.7) can be solved by a direct method or by a suitable iterative method. In numerical experiments, the standard routines DGBSV and DGBSVX of LAPACK are used.

Now, the internal iteration method is used to approximate solution of equation (4.2) as follows:

$$\frac{\left(\mathbf{E}_h\psi^{n+1,k}\right)_{i,j} - \left(\mathbf{E}_h\psi^n\right)_{i,j}}{\tau} + \frac{2}{r_i^2}\left(\Lambda_z\tilde{\psi}\right)_{i,j}\left(\mathbf{E}_h\psi^n\right)_{i,j}$$

$$-\frac{1}{r_i}\left(\Lambda_z\tilde{\psi}\right)_{i,j}\left[\frac{\left(\mathbf{E}_h\tilde{\psi}\right)_{i+1,j} - \left(\mathbf{E}_h\tilde{\psi}\right)_{i-1,j}}{2h_r}\right] + \frac{1}{r_i}\left(\Lambda_r\tilde{\psi}\right)_{i,j}\left[\frac{\left(\mathbf{E}_h\tilde{\psi}\right)_{i,j+1} - \left(\mathbf{E}_h\tilde{\psi}\right)_{i,j-1}}{2h_z}\right]$$

$$-\frac{1}{r_i^2 h_z}J_{i,j}^{n+\frac{1}{2}}\left(J_{i,j+1}^{n+\frac{1}{2}} - J_{i,j-1}^{n+\frac{1}{2}}\right) = E_h^2\psi_{i,j}^{n+1}, \quad (4.8)$$

where $\mathbf{E}_h = \Lambda_{r^2} - \frac{1}{2}\Lambda_r + \Lambda_{z^2}$ and $\mathbf{E}_h^2 = \Lambda_{r^4} - \frac{2}{r_i}\Lambda_{r^3} + \frac{3}{r_i^2}\Lambda_{r^2} - \frac{3}{r_i^3}\Lambda_r - \frac{2}{r_i}\Lambda_{rz^2} + 2\Lambda_{r^2z^2} + \Lambda_{z^4}$.

The central-difference operators are used for all derivatives

$$(\Lambda_r\psi)_{ij} = \frac{\psi_{i+1,j} - \psi_{i-1,j}}{2h_r};$$

$$(\Lambda_z\psi)_{ij} = \frac{\psi_{i,j+1} - \psi_{i,j-1}}{2h_z};$$

$$(\Lambda_{r^2}\psi)_{ij} = \frac{\psi_{i+1,j} - 2\psi_{i,j} + \psi_{i-1,j}}{h_r^2};$$

$$(\Lambda_{z^2}\psi)_{ij} = \frac{\psi_{i,j+1} - 2\psi_{i,j} + \psi_{i,j-1}}{h_z^2};$$

$$(\Lambda_{r^3}\psi)_{ij} = \frac{\psi_{i+2,j} - 2\psi_{i+1,j} + 2\psi_{i-1,j} - \psi_{i-2,j}}{2h_r^3};$$

$$(\Lambda_{z^3}\psi)_{ij} = \frac{\psi_{i,j+2} - 2\psi_{i,j+1} + 2\psi_{i,j-1} - \psi_{i,j-2}}{2h_z^3};$$

$$(\Lambda_{r^2 z}\psi)_{ij} = \frac{1}{2h_z h_r^2}\Bigg\{ (\psi_{i+1,j+1} - \psi_{i+1,j-1}) - 2(\psi_{i,j+1} - \psi_{i,j-1})$$
$$+ (\psi_{i-1,j+1} - \psi_{i-1,j-1}) \Bigg\};$$

$$(\Lambda_{r z^2}\psi)_{ij} = \frac{1}{2h_r h_z^2}\Bigg\{ (\psi_{i+1,j+1} - \psi_{i-1,j+1}) - 2(\psi_{i+1,j} - \psi_{i-1,j})$$
$$+ (\psi_{i+1,j-1} - \psi_{i-1,j-1}) \Bigg\};$$

$$(\Lambda_{r^4}\psi)_{ij} = \frac{\psi_{i+2,j} - 4\psi_{i+1,j} + 6\psi_{i,j} - 4\psi_{i-1,j} + \psi_{i-2,j}}{h_r^4};$$

$$(\Lambda_{z^4}\psi)_{ij} = \frac{\psi_{i,j+2} - 4\psi_{i,j+1} + 6\psi_{i,j} - 4\psi_{i,j-1} + \psi_{i,j-2}}{h_z^4};$$

$$(\Lambda_{r^2 z^2}\psi)_{ij} = \frac{1}{h_r^2 h_z^2}\Bigg\{ (\psi_{i+1,j+1} - 2\psi_{i+1,j} + \psi_{i+1,j-1}) - 2(\psi_{i,j+1} - 2\psi_{i,j} + \psi_{i,j-1})$$
$$+ (\psi_{i-1,j+1} - 2\psi_{i-1,j} + \psi_{i-1,j-1}) \Bigg\}.$$

The boundary conditions are approximated on two-point stencils with the second-order of approximation as follows

$$\psi_{2,j}^n - \psi_{1,j}^n = 0; \qquad \psi_{1,j}^n + \psi_{2,j}^n = 0 \quad \Rightarrow \quad \psi_{1,j}^n = \psi_{2,j}^n = 0, \qquad (4.9)$$

$$\psi_{N_r,j}^n - \psi_{N_r-1,j}^n = 0; \quad \psi_{N_r-1,j}^n + \psi_{N_r,j}^n = 0 \quad \Rightarrow \quad \psi_{N_r-1,j}^n = \psi_{N_r,j}^n = 0, \quad (4.10)$$

$$\psi_{i,2}^n - \psi_{i,1}^n = 0; \qquad \psi_{i,1}^n + \psi_{i,2}^n = 0 \quad \Rightarrow \quad \psi_{i,1}^n = \psi_{i,2}^n = 0, \qquad (4.11)$$

$$\psi_{i,N_z}^n - \psi_{i,N_z-1}^n = 0; \quad \psi_{i,N_z-1}^n + \psi_{i,N_z}^n = 0 \quad \Rightarrow \quad \psi_{i,N_z}^n = -\psi_{i,N_z-1}^n = 0, \quad (4.12)$$

where $\psi_{i,j}^n = \psi[x_i, y_j, t_n = (n-1)\tau]$, $i = 1, \ldots, N_r$, $j = 1, \ldots, N_z$, $n = 1, 2, \ldots$

4.3   Results

The developed here numerical method to have new evidences to corroborate the characteristic of the function Φ on the Taylor-Couette flow are applied. The case

when both end plates rotate with the same angular velocity, while independently from the inner cylinder and the outer cylinder is held at rest is considered. The $Re = 80$, $\eta = 0.5$, $\Gamma = 2$ and $\Omega = 0, 1$ are fixed.

The results from numerical simulations in terms of $\psi - J$ for the axisymmetric flow are presented and compared with the numerical results in Aristov-Pukhnechev's form. Table 4.1 represents the comparison maximum values of the stream function and angular momentum. The contour of streamlines for $\Omega = 0$ and $\Omega = 1$ are shown in Figure 4.1 which generated using either grid 32×62. In Figures 4.2 and 4.3, the values of the function Φ on the boundaries are marked with different lines: ——— $\psi - J$'s form; $\cdots$ Aristov-Pukhnechev's form. Note that the function Φ is computed from ψ after the iteration converge. They are in close agreement with computation data from Aristov-Pukhnechev's form.

Table 4.1 Comparison of $\tilde{\psi}_{max} = \psi_{max}/Re$ and J_{max} for the values $\Omega = 0, 1$ and $Re = 80$, $\Gamma = 2$.

Reference	$\Omega = 0$		$\Omega = 1$	
	$\tilde{\psi}_{max}$	J_{max}	$\tilde{\psi}_{max}$	J_{max}
Present	0.04237	119.732	0.09976	472.341
Aristov–Pukhnachev's form	0.04249	119.729	0.10002	472.318
Abshagen et al. (2004)	0.04270	–	0.10014	–
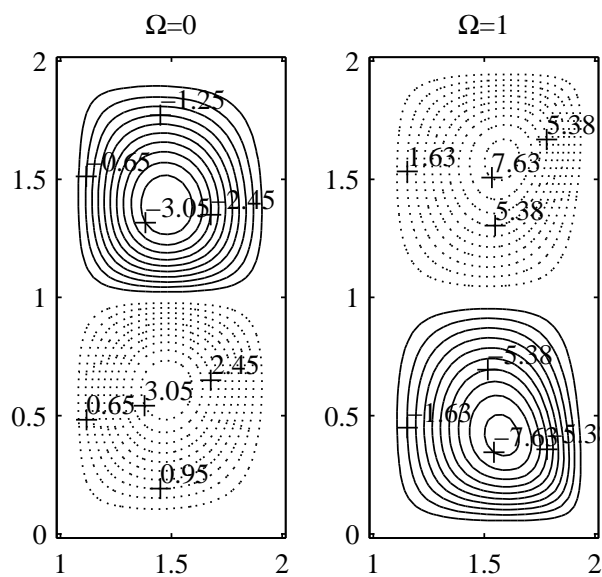
Figure 4.1 Contour plots of stream function at $\Gamma = 2$, $\eta = 0.5$, and $Re = 80$.
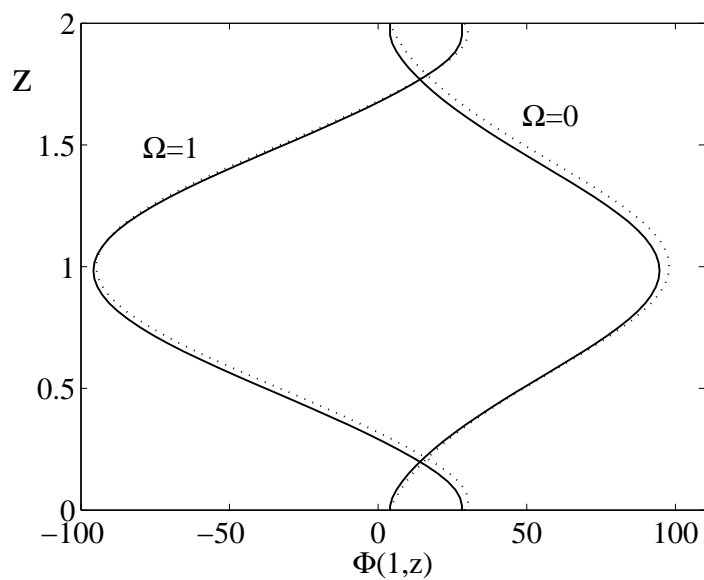
Figure 4.2 'Exact' calculated boundary values of $\Phi(1, z)$ in the case $Re = 80$, $\eta = 0.5$, and $\Gamma = 2$ for $\Omega = 0$ and $\Omega = 1$.
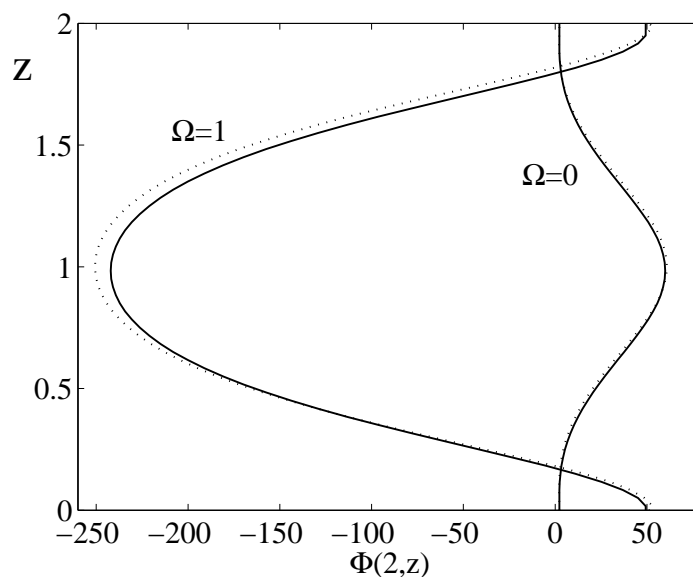
Figure 4.3 'Exact' calculated boundary values of $\Phi(2,z)$ in the case $Re = 80$, $\eta = 0.5$, and $\Gamma = 2$ for $\Omega = 0$ and $\Omega = 1$.

4.4 Conclusion

The results of this chapter shown suffice to illustrate that the new formulation of the Navier-Stokes equation purposed by Aristov and Pukhnachev (2004) can be used to simulate the axisymmetric flow. The simulation uncovered here can be used to corroborate the geometric structure of the boundary of the function Φ in Chapter III.

4.5 References

Aristov, S.N., and Pukhnachev, V.V. (2004). On the equations of axisymmetric motion of a viscous incompressible. **Doklady Physics** 49(2):112–115.

Abshagen, J., Cliffe, K.A., Langenberg, J., Mullin, T., Pfister, G., and Tavener, S.J.

(2004). Taylor-Couette flow with independently rotating end plates. **Theoretical and Computational Fluid Dynamics** 18:129–136.

CHAPTER V

FINITE DIFFERENCE FOR NEW FORM OF THE NAVIER-STOKES EQUATIONS FOR 2D PLANE FLOW

In the present work, a finite-difference method is developed for a new form of the Navier-Stokes equations proposed by Pukhnachev (2004) who introduces a new function that is related to the pressure and stream function. The scheme and algorithm treat the equations as a coupled system which allows one to satisfy two conditions for the stream function with no condition on the new function. The numerical algorithm is applied to the lid-driven cavity flow as the benchmark problem. The characteristic of this flow was adequately represented by the new numerical model.

5.1   Introduction

In the present study, the NSEs in terms of new variables for the 2D plane viscous incompressible flow had been introduced. The idea of Aristov and Pukhnachev (2004) and Pukhnachev (2004) for the cases of 2D axisymmetric and 2D plane motions were followed. The 2D NSEs in terms of the new functions contain one transport equation for the stream function and one elliptic equation for the new unknown variable. This system resembles the vorticity and stream function's form but the physical meaning of the coupling function is different.

It may be worthwhile to briefly mention why the 2D flow is important. It has

applications in the industry (e.g. progressive cavity pumps) and important to the scientific world, specifically in fluid mechanics. In general, a viscous fluid flow inside a driven cavity has been a common experiment approach used to check or improve numerical techniques (see for example, Botella and Peyret, 1998; Spotz 1998; Christov and Marinava, 2001; Bruneau and Saad, 2006).

The content of this chapter is organized as follows. In the next section, a new formulation of the NSEs with the no-slip boundary conditions was derived. Section 5.3 briefly describes the problem used for the test case and detailed description of numerical algorithm. The results of validation of the finite difference scheme are presented in Section 5.4. The detailed comparisons with available numerical and experimental data are made.

5.2 New Formulation of the Navier-Stokes equations

To make presentation self completed first demonstrate the transformation of the viscous incompressible NSEs to a new form. The 2D plane viscous incompressible flow is governed by the NSEs in the Cartesian coordinate system (x, y),

$$u_t + uu_x + vu_y = -\frac{1}{\rho}p_x + \nu\big(u_{xx} + u_{yy}\big), \tag{5.1}$$

$$v_t + uv_x + vv_y = -\frac{1}{\rho}p_y + \nu\big(v_{xx} + v_{yy}\big), \tag{5.2}$$

$$u_x + v_y = 0, \tag{5.3}$$

where u and v are the velocity components in $x-$ and $y-$directions, respectively; p is the pressure, ρ is the fluid density, and ν is the kinematic viscosity. The fluid is subjected to potential external forces. In 2D, the constrain of incompressibility $\nabla \cdot \bar{v} = 0$ can be satisfied exactly by expressing the velocity vector in terms of the stream function ψ according to

$$u = \frac{\partial \psi}{\partial y}, \quad v = -\frac{\partial \psi}{\partial x}. \tag{5.4}$$

A new form is based on the following observation. The substitution of equation (5.4) into equation (5.1) yields

$$\frac{\partial}{\partial y}\left(\psi_t - \psi_x\psi_y - \nu\Delta\psi\right) + \frac{\partial}{\partial x}\left(\frac{1}{\rho}p + \psi_y^2\right) = 0, \tag{5.5}$$

where

$$\Delta \stackrel{\text{def}}{=} \frac{\partial^2}{\partial x^2} + \frac{\partial^2}{\partial y^2}.$$

Therefore, there is a function Φ satisfies the relations

$$\frac{1}{\rho}p = -\psi_y^2 + \Phi_y, \tag{5.6}$$

and

$$\psi_t - \psi_x\psi_y + \Phi_x = \nu\Delta\psi. \tag{5.7}$$

Differentiating equation (5.6) and equation (5.7) with respect to y and x, respectively, and substituting the resulting expressions into (5.2), where u and v are expressed in terms of ψ obtaining

$$\Delta\Phi = 2\psi_y\Delta\psi. \tag{5.8}$$

The main target of recent work is to develop and validate a finite-difference scheme to approximate solution of problems (5.7)–(5.10). The case of the no-slip conditions satisfied at the boundary of the flow domain will be considered only. In terms of the function ψ only, boundary conditions are

$$\psi = 0, \ \frac{\partial\psi}{\partial n} = b(x, y), \tag{5.9}$$

where $\dfrac{\partial\psi}{\partial n}$ means derivative in the direction of the normal vector to the boundary. To complete the formulation of the problem it is necessary to specify the initial conditions

$$\psi = \psi_0(x, y), \ \Phi = \Phi_0(x, y), \ t = 0. \tag{5.10}$$

5.3   Numerical Technique

The standard benchmark problem for testing the 2D NSEs is the driven cavity flow as shown in Figure 5.1. The fluid contained inside a squared cavity is set into motion by the top wall which is sliding at constant velocity from left to right. Let L be the characteristic length scale associated with the cavity geometry and U be the characteristic velocity scale associated with the moving boundary.   The non-
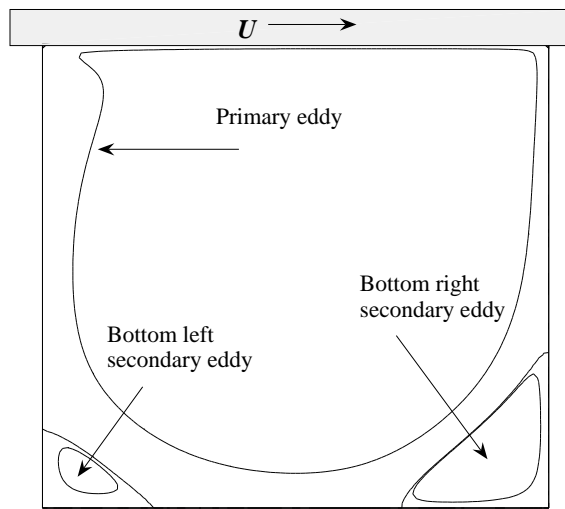
Figure 5.1 Square cavity with an infinitely long plate.

dimensional parameter of the problem is

$$\mathrm{Re} = \frac{LU}{\nu},\tag{5.11}$$

is the Reynolds number. The system of equations (5.1)–(5.3) is rendered dimensionless as follows

$$x = \frac{x^*}{L}, \quad y = \frac{y^*}{L}, \quad t = \frac{t^*\nu}{L^2}, \quad u = \frac{u^*}{U}, \quad v = \frac{v^*}{U}.\tag{5.12}$$

To discuss the detail of numerical algorithm, the lid-driven cavity flow is considered. The domain $Q = \{0 \leqslant x \leqslant 1,\ 0 \leqslant y \leqslant 1\}$, is covered with a uniform staggered grid

$$Q_h = \{(x_i, y_j) | x_i = (i - 1.5)h_x,\ y_j = (j - 1.5)h_y, i = 1, \ldots, N_x,\ j = 1, \ldots, N_y\}$$

with spacings

$$h_x = \frac{1}{N_x - 2}, \quad h_y = \frac{1}{N_y - 2},$$

in the $x-$ and $y-$directions, respectively. Such grid allows one to use the central differences to approximate boundary conditions with the second-order on two-point stencils.

The essential element of the proposed here algorithm is that equations (5.7) and (5.8) for ψ and Φ are considered as a coupled system. Note that ψ and Φ are evaluated on the full-time steps. This formulation is based on the idea of regarding the two boundary conditions for ψ as actual conditions for the $\psi - \Phi$ system. The second-order central-difference approximations for the operators in equations (5.7) and (5.8) are employed. The system of difference equations is

$$\frac{\psi_{i,j}^{n+1} - \psi_{i,j}^n}{\tau} - Re \frac{(\psi_{i+1,j}^n - \psi_{i-1,j}^n)(\psi_{i,j+1}^{n+1} - \psi_{i,j-1}^{n+1}) + (\psi_{i+1,j}^{n+1} - \psi_{i-1,j}^{n+1})(\psi_{i,j+1}^n - \psi_{i,j-1}^n)}{8 h_x h_y}$$
$$+ Re \frac{(\Phi_{i+1,1}^{n+1} - \Phi_{i-1,j}^{n+1})}{2 h_x} = \frac{1}{2} \left(\triangle \psi_{i,j}^{n+1} + \triangle \psi_{i,j}^n \right), \quad (5.13)$$

$$\triangle \Phi_{i,j}^{n+1} = \frac{1}{2 h_y} \left[(\psi_{i,j+1}^n - \psi_{i,j-1}^n) \triangle \psi_{i,j}^{n+1} + (\psi_{i+1,j}^{n+1} - \psi_{i-1,j}^{n+1}) \triangle \psi_{i,j}^n \right],$$

$$i = 2, \ldots, N_x - 1, \quad j = 2, \ldots, N_y - 1. \quad (5.14)$$

The boundary conditions are written in the following form

$$\begin{aligned}
\frac{\psi_{2,j}^{n+1} + \psi_{1,j}^{n+1}}{2} = 0, \quad & \frac{\psi_{2,j}^{n+1} - \psi_{1,j}^{n+1}}{h_x} = 0, \\
\frac{\psi_{N_x,j}^{n+1} + \psi_{N_x-1,j}^{n+1}}{2} = 0, \quad & \frac{\psi_{N_x,j}^{n+1} - \psi_{N_x-1,j}^{n+1}}{h_x} = 0, \\
\frac{\psi_{i,2}^{n+1} + \psi_{i,1}^{n+1}}{2} = 0, \quad & \frac{\psi_{i,2}^{n+1} - \psi_{i,1}^{n+1}}{h_y} = 0, \\
\frac{\psi_{i,N_y}^{n+1} + \psi_{i,N_y-1}^{n+1}}{2} = 0, \quad & \frac{\psi_{i,N_y}^{n+1} - \psi_{i,N_y-1}^{n+1}}{h_y} = 1,
\end{aligned} \qquad \begin{aligned} & j = 1, \ldots, N_y, \\ \\ & i = 1, \ldots, N_x. \end{aligned} \qquad (5.15)$$

Equations (5.13)–(5.15) are a coupled system of a linear equation. To combine equations (5.13)–(5.15) as a *single* linear system with a banded matrix, two new indices

are introduced as follows

$$k_{(i,j)} = 2(j-1)N_x + 2i - 1, \quad i = 1, \ldots, N_x,$$

$$m_{(i,j)} = 2(j-1)N_x + 2i = k_{(i,j)} + 1, \quad j = 1, \ldots, N_y.$$

Each node (i,j) of the grid Q_h associates with two indices $k_{(i,j)}$ and $m_{(i,j)}$. An index $k_{(i,j)}$ is an odd number and an index $m_{(i,j)}$ is an even number. It is easy to see that

$$k_{(i+1,j)} = k_{(i,j)} + 2, \quad k_{(i,j+1)} = k_{(i,j)} + 2N_x,$$

$$k_{(i-1,j)} = k_{(i,j)} - 2, \quad k_{(i,j-1)} = k_{(i,j)} - 2N_x, \tag{5.16a}$$

$$m_{(i+1,j)} = m_{(i,j)} + 2, \quad m_{(i,j+1)} = m_{(i,j)} + 2N_x,$$

$$m_{(i-1,j)} = m_{(i,j)} - 2, \quad m_{(i,j-1)} = m_{(i,j)} - 2N_x. \tag{5.16b}$$

Now, a new grid function σ_k is introduced. It is defined on the composite grid where σ_k represents $\psi_{i,j}$ and $\sigma_m(= \sigma_{k+1})$ represents $\Phi_{i,j}$. Substituting σ_k instead $\psi_{i,j}$ and substituting σ_m instead $\Phi_{i,j}$ into equations (5.13)–(5.14), the algebraic system can be recast as the following form

$$\frac{\sigma_k^{n+1} - \sigma_k^n}{\tau} + \frac{Re}{8h_x h_y}\Big[\left(\sigma_{k+2}^n - \sigma_{k-2}^n\right)\left(\sigma_{k+2N_x}^{n+1} - \sigma_{k-2N_x}^{n+1}\right) + \left(\sigma_{k+2}^{n+1} - \sigma_{k-2}^{n+1}\right)$$

$$\left(\sigma_{k+2N_x}^n - \sigma_{k-2N_x}^n\right)\Big] - \frac{Re}{2h_x}\left(\sigma_{k+1}^{n+1} - \sigma_{k-3}^{n+1}\right) = \frac{1}{2}\left(\Delta\sigma_k^{n+1} + \Delta\sigma_k^n\right),$$

$$\tag{5.17a}$$

$$\Delta\sigma_m^{n+1} = \frac{\left(\sigma_{m+2N_x-1}^n - \sigma_{m-2N_x-1}^n\right)}{2h_y}\Delta\sigma_{m-1}^{n+1} + \frac{\left(\sigma_{m+2N_x-1}^{n+1} - \sigma_{m-2N_x-1}^{n+1}\right)}{2h_y}\Delta\sigma_{m-1}^n, \tag{5.17b}$$

where

$$\Delta\sigma_k = \frac{\left(\sigma_{k+2} - 2\sigma_k + \sigma_{k-2}\right)}{h_x^2} + \frac{\left(\sigma_{k+2N_x} - 2\sigma_k + \sigma_{k-2N_x}\right)}{h_y^2}.$$

Since the straightforward implementation of the algorithm leads to a problem with a numerically singular matrix. There are different ways to regularize the problem. Adding a small term at the boundary gives the best results is found. According

to this idea, equation (5.15) can be rewritten for the function σ as follows

$$\frac{\sigma_k^{n+1} + \sigma_{k+2}^{n+1}}{2} = 0, \quad \frac{\sigma_{m+1}^{n+1} - \sigma_{m-1}^{n+1}}{h_x} = -\varepsilon\sigma_m^{n+1}, \quad i = 1, j = 1, \ldots, N_y, \quad (5.18a)$$

$$\frac{\sigma_k^{n+1} + \sigma_{k-2}^{n+1}}{2} = 0, \quad \frac{\sigma_{m-1}^{n+1} - \sigma_{m-3}^{n+1}}{h_x} = -\varepsilon\sigma_m^{n+1}, \quad i = N_x, j = 1, \ldots, N_y, \quad (5.18b)$$

$$\frac{\sigma_k^{n+1} + \sigma_{k+2N_x}^{n+1}}{2} = 0, \quad \frac{\sigma_{m+2N_x+1}^{n+1} - \sigma_{m-1}^{n+1}}{h_y} = 0, \quad j = 1, i = 1, \ldots, N_x, \quad (5.18c)$$

$$\frac{\sigma_k^{n+1} + \sigma_{k-2N_x}^{n+1}}{2} = 0, \quad \frac{\sigma_{m-1}^{n+1} - \sigma_{m-2N_x-1}^{n+1}}{h_y} = 1, \quad j = N_y, i = 1, \ldots, N_x. \quad (5.18d)$$

If the steady flow is needed then the algorithm can be considered as an iterative procedure. Iterations are terminated at the certain time $n = N$ when the following criterion is satisfied

$$\frac{\max_{i,j}\left|\sigma_{i,j}^{N+1} - \sigma_{i,j}^N\right|}{\max_{i,j}\left|\sigma_{i,j}^{N+1}\right|} \leqslant 10^{-8}.$$

Note that the linear system for the coupled formulation of the $\psi - \Phi$ problem can be written as the following multi-diagonal system for the composite grid function σ

$$B_{l-2N_x-1}\sigma_{l-2N_x-1}^{n+1} + B_{l-2N_x}\sigma_{l-2N_x}^{n+1} + B_{l-3}\sigma_{l-3}^{n+1} + B_{l-2}\sigma_{l-2}^{n+1}$$

$$+ B_{l-1}\sigma_{l-1}^{n+1} + B_l\sigma_l^{n+1} + B_{l+1}\sigma_{l+1}^{n+1} + B_{l+2}\sigma_{l+2}^{n+1}$$

$$+ B_{l+2N_x-1}\sigma_{l+2N_x-1}^{n+1} + B_{l+2N_x}\sigma_{l+2N_x}^{n+1} + B_{l+2N_x+1}\sigma_{l+2N_x+1}^{n+1} = F_l, \quad (5.19)$$

where $l = 1, \ldots, 2N_y N_x$. The matrix of the linear system (5.19) is banded with $2N_x + 1$ lower and upper bandwidths. The standard routings DGBSV and DGBSVX of the LAPACK routine are used to compute the solution of equation (5.19).

5.4   Results

A validation test involves the 2D cavity flow at the Reynolds number up to 1000, wherein the flow is laminar and steady. Computations were performed for the lid-driven cavity problem on the grids 32×32 up to 102×102.

The coupling for the latter system is crucial because of the lack of boundary conditions for the new function and the presence of two boundary conditions for the stream function. After special renumbering the grid points, the coupled system was formulated as a single system and solved by LAPACK routine. To avoid the singularity, small parameter ε was added in part of the Neumann boundary condition. The impact of ε on the results was judiciously evaluated by numerical experiments and shown that for $\varepsilon \in [10^{-10}, 10^{-4}]$ the approximate solution agreed with know test case.

In order to validate the scheme, the extrema values of the stream function and space location were compared with Botella and Peyret (1998), Christov and Marinova (2001), Bruneau and Saad (2006). Table 5.1 reports the characteristics of the primary and right bottom secondary eddies at $Re = 100$ and $Re = 1000$. These tables show the extrema values of ψ and the space location of the extrema values of ψ. Top rows present the quantities obtained from simulation. Then bottom rows display the quantities obtained by the other authors. For the primary vortex in cases $Re = 100$ and 1000, the numerical results agree within 5% with those obtained by the other authors. For the secondary vortex in case $Re = 1000$ with the grids 52×52 agree within 5% with Christov and Marinova (2001) but differ significantly up to 10% with those obtained by Botella and Peyret (1998). The geometrical structures of the flow are displayed in Figures 5.2 and 5.3 that were generated on grid 102×102. Note that the values of u (velocity along $x-$direction), v (velocity along $y-$direction), and vorticity ω were computed from ψ after the iteration converge. The values of u, v, and ω inside the domain were approximated using central-difference scheme while the values of u, v, and ω on the boundary were approximated using one side first-order difference scheme.

In Figure 5.4, the centerline $u-$ and $v-$velocity profiles were compared with

data of Ghia, Ghia, and Shin (1982). The computational had been done for the Reynolds number $Re = 1000$ with the grid 102×102. The velocity profiles are similar to the data of Ghia, Ghia, and Shin (1982).

Table 5.1 Some characteristics values of the cavity flow at $Re = 100$ and $Re = 1000$.

Re	Reference	Grid	Primary eddy		Bottom right secondary eddy	
			ψ_{min}	(x_{min}, y_{min})	ψ_{miax}	(x_{max}, y_{max})
100	Present	32×32	-0.103615	$(0.600, 0.733)$	3.34039×10^{-6}	$(0.967, 0.067)$
		52×52	-0.1035694	$(0.62, 0.74)$	9.420288×10^{-6}	$(0.94, 0.06)$
		102×102	-0.1035105	$(0.62, 0.74)$	1.189202×10^{-5}	$(0.94, 0.06)$
	Christov et al. (1994)	162×162	-0.10397	$(0.6198, 0.7369)$	–	–
	Botella et al. (1998)	48	-0.10007627	–	–	–
1000	Present	52×52	-0.119825	$(0.54, 0.56)$	1.561921×10^{-3}	$(0.86, 0.10)$
		102×102	-0.1192801	$(0.53, 0.56)$	1.688174×10^{-3}	$(0.87, 0.11)$
	Botella et al. (1998)	160	-0.1189366	–	1.729717×10^{-3}	–
	Christov et al. (2001)	512×512	-0.116269	$(0.5316, 0.5660)$	1.640×10^{-3}	$(0.8651, 0.1118)$
	Bruneau et al. (2006)	1024×1024	-0.11892	$(0.5312, 0.5654)$	1.7292×10^{-3}	$(0.8643, 0.1123)$
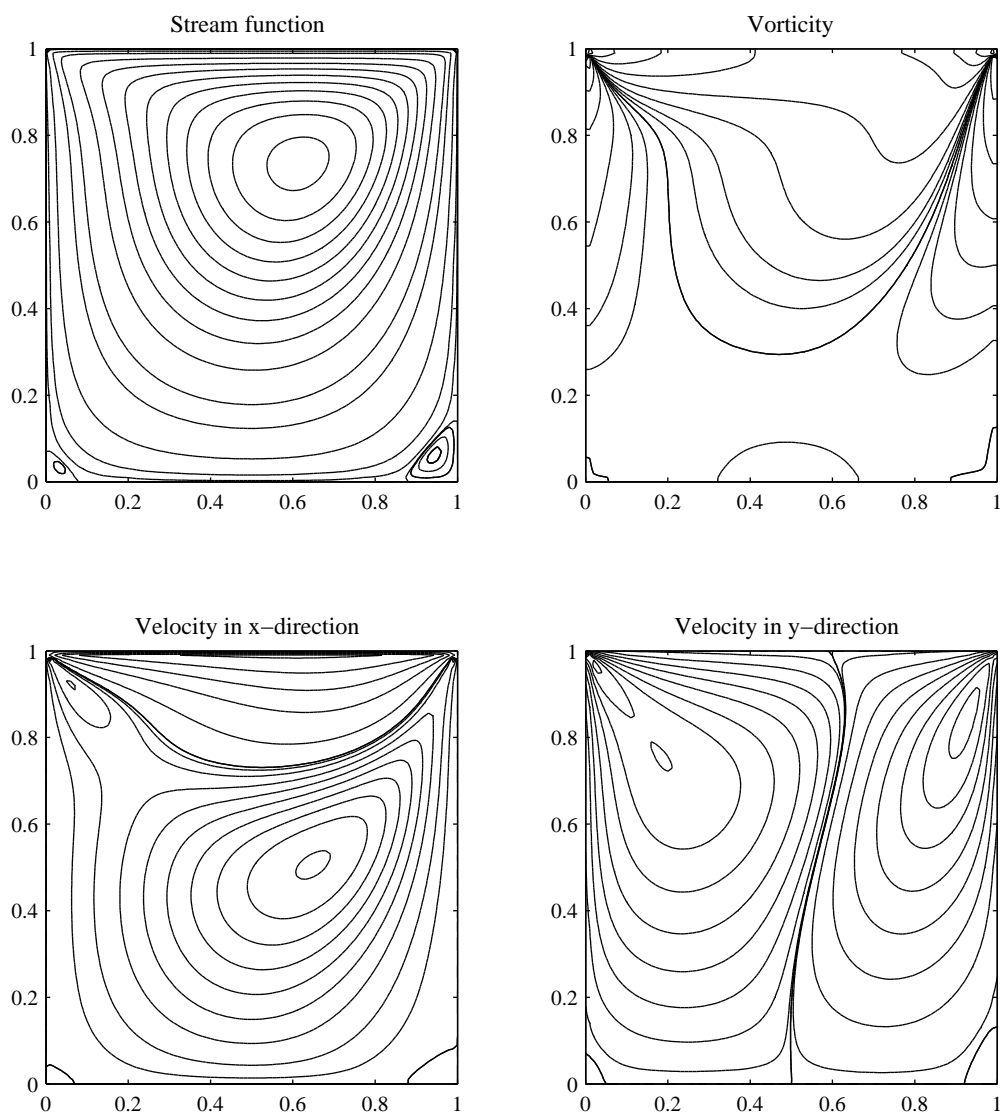
Figure 5.2 Stream function ψ, vorticity ω, u, and v contours for the lid-driven cavity flow at $Re = 100$.
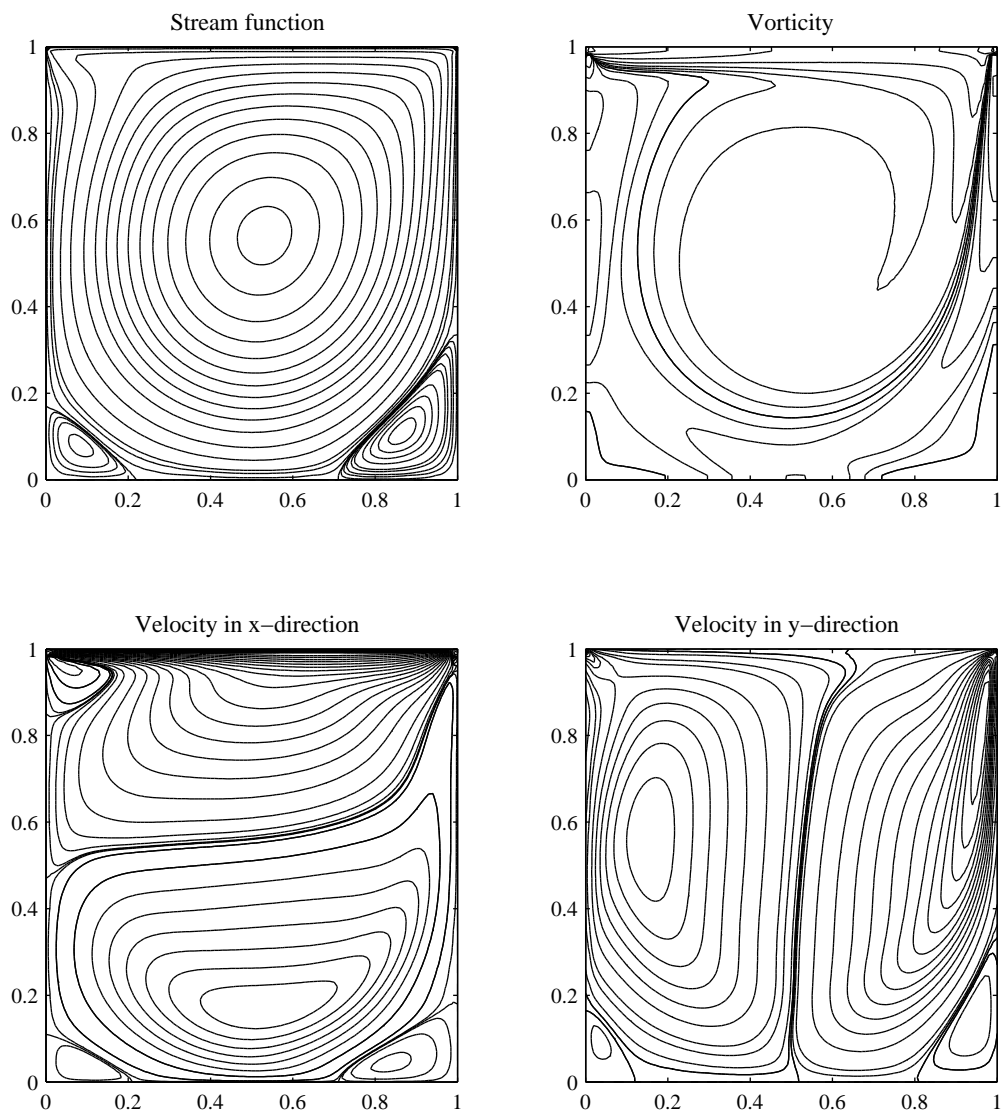
Figure 5.3 Stream function ψ, vorticity ω, u, and v contours for the lid-driven cavity flow at $Re = 1000$.

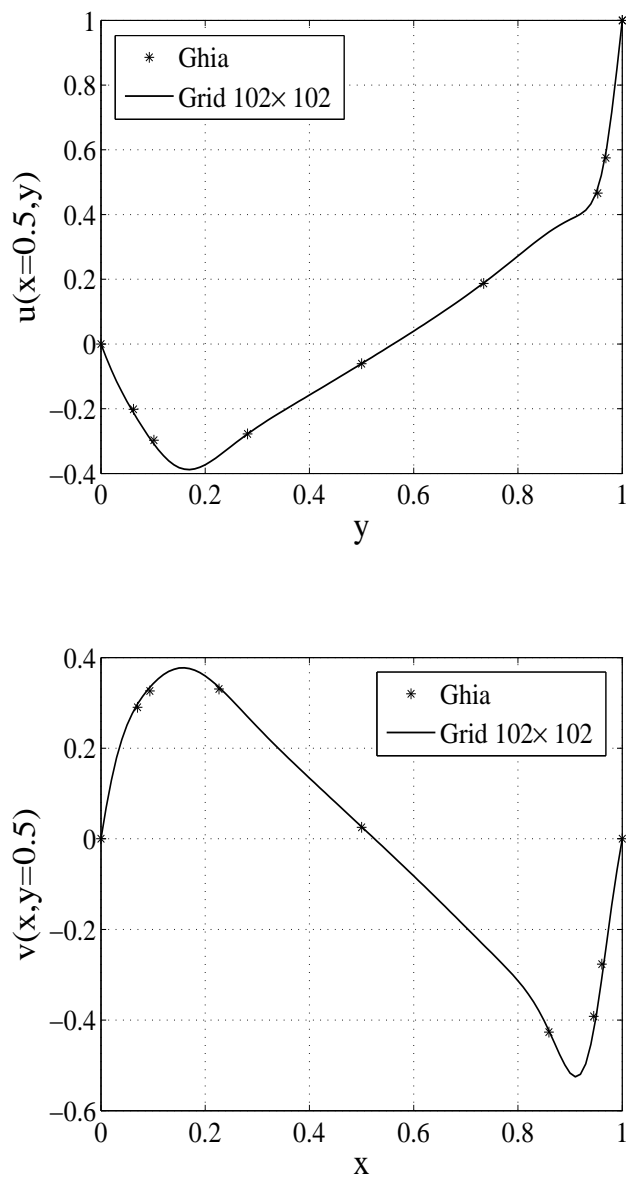**Figure 5.4** Vertical centerline $u-$profile and horizontal centerline $v-$profile for the lid-driven cavity flow at $Re = 1000$.
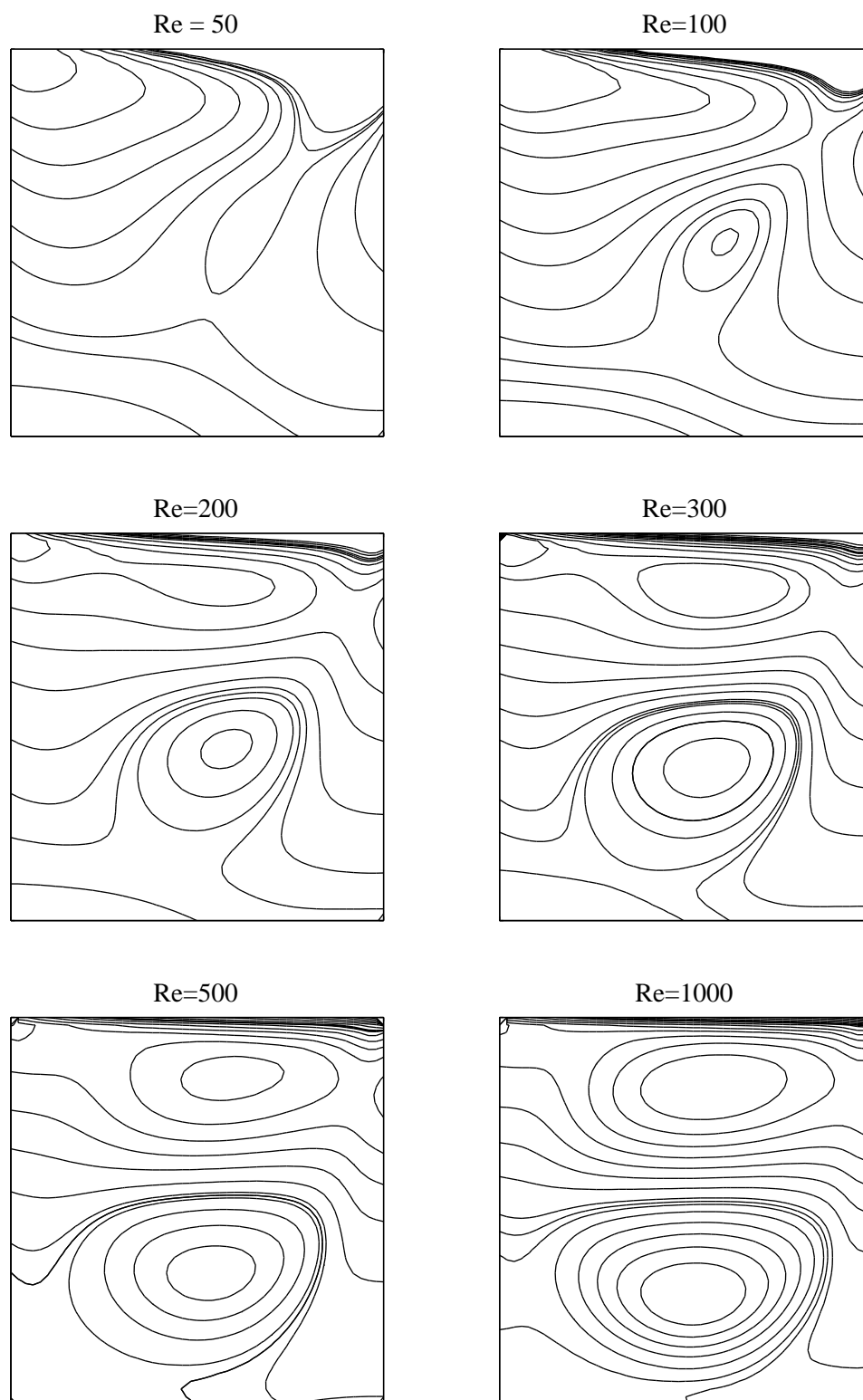
Re = 50

Re=100

Re=200

Re=300

Re=500

Re=1000

Figure 5.5 Contours of Φ for the lid-driven cavity flow.

Figure 5.5 shows the contour of a function Φ to understand the behavior of the function Φ for the different Reynolds number. Pattern of contour lines of Φ were drawn for the several Reynolds numbers, $Re = 50, 100, 200, 300, 500,$ and 1000. The set of figures was generated on the grid 52×52 with the parameter $\varepsilon = 10^{-6}$.

5.5   Conclusion

The finite-difference scheme developed and validated for the new formulation for the 2D Navier-Stokes equations proposed in Pukhnachev (2004). The new numerical algorithm demonstrated good accuracy and reasonable efficient for the lid-driven cavity was applied. The results of numerical experiments shown that the new formulation is a viable approach to the 2D Navier-Stokes flow.

5.6   References

Aristov, S.N., and Pukhnachev, V.V. (2004). On the Equations of Axisymmetric Motion of a Viscous Incompressible. **Doklady Physics** 49(2):112–115.

Botella, O., and Peyret, R. (1998). Benchmark spectral results on the lid-driven cavity flow. **Computers & Fluids** 27(4):421–433.

Bruneau, C.H., and Saad, M. (2006). The 2D lid-driven cavity problem revisited. **Computers & Fluids** 35:326–348.

Christov, C.I., and Marinova, R.S. (2001). Implicit vectorial operator splitting for incompressible Navier-Stokes equations in primitive variables. **Journal Computational Technologies** 6(4):92–119.

Christov, C.I., and Ridha, R.I. (1994). Splitting scheme for iterative solution of biharmonic equation, application to 2D Navier-Stokes problems. **Advances**

in Numerical Methods and Applications, Singapure: World Sciences 341–352.

Ghia, U., Ghia, K.N., and Shin, C.T. (1982). High-resolutions for incompressible flow using the Navier-Stokes equations and multigrid method. **Journal of Computational Physics** 48:387–411.

Pukhnachev, V.V. (2004). Integrals of motion of an incompressible fluid occupying the entire space. **Journal of Applied Mechanics and Technical Physics** 45(2):167–171.

Spotz, W.F. (1998). Accuracy and performance of numerical wall boundary conditions for steady, 2D, incompressible streamfunction vorticity. **International Journal for Numerical Methods in Fluids** 28:737–757.

CHAPTER VI

CONCLUSIONS

In this last chapter, first the major contributions made in this research are summarized, and then conclusions are drawn from the presented results. Finally, recommendations are presented for future research efforts.

6.1   Contributions

The contributions made in this research can be categorized as follows:

(i) Development of three finite-difference schemes for the 2D incompressible Navier-Stokes in terms of the stream function using the Crank-Nicolson approximation of the bi-harmonic term and differ by approximation of nonlinear convective terms

(ii) Application of these methods to the lid-driven cavity flow up to $Re = 10000$

(iii) Development of the novel finite-difference schemes for a new form of the Navier-Stokes equation proposed by Aristov and Pukhnachev (2004) and Pukhnachev (2004)

(iv) Application of these novel finite-difference schemes to the Taylor-Couette flow between two rotating cylinders when the lids are also allowed to rotate

(v) Application of these novel finite-difference schemes to the lid-driven cavity flow up to $Re = 1000$

First, three algorithms for the 2D incompressible Navier-Stokes equations have been presented. All terms of the Navier-Stokes equations are approximated by the central finite-differences and the idea of the Crank-Nicolson approach utilized to the bi-harmonic operator. Nonlinear terms are approximated by an explicit way (explicit scheme), an operator splitting technique (operator splitting scheme), and use of internal iteration on nonlinearity in third scheme (internal iteration scheme). The operator splitting scheme is absolutely stable. The explicit scheme and internal iteration scheme have simple computer realization. All three schemes have been compared on a benchmark problem of the lid-driven cavity flow. For the moderate Reynolds numbers up to 3000, three schemes have good accuracy and the maximum value of time increment to get convergence is smallest for an explicit scheme but largest for an internal iteration scheme. For the higher Reynolds number greater than 3000, the operator splitting scheme does not work on a coarse grid and the internal iteration scheme demonstrate the best performance. The explicit scheme requires a large computational time due to a small time increment.

Second, a new formulation of the 2D Navier-Stokes equations is derived according to Aristov and Pukhnachev (2004) and Pukhnachev (2004). A introduced new function is related to the pressure and a system that is similar to the vorticity/stream function formulation is derived. A novel numerical algorithm for the new form of the Navier-Stokes equations has been developed. The scheme and algorithm treat equations for the stream function and new unknown function as an inextricably coupled system which allows one to satisfy two boundary conditions for the stream function with no condition on the auxiliary function. The issue of singularity of the matrix is tackled by adding a small parameter in the boundary conditions. The scheme is thoroughly validated on girds with different resolutions.

The new numerical tool is applied to the Taylor flow between concentric rotating cylinders when the upper and lower lids are allowed to rotate independently from the inner cylinder, while the outer cylinder is held at rest. The phenomenology of this flow is adequately represented by the numerical model, including the hysteresis that takes place near the certain specific values of the Reynolds number.

Finally, the presented finite-difference scheme is applied to the lid-driven cavity. Thus the numerical results demonstrate the viability of the new model.

6.2   Conclusions

The following conclusions can be drawn from the present work.

First, for very high Reynolds numbers the nonlinearity of the Navier-Stokes equations and the implicit nature of the continuity condition can turn out to the rather different from theoretical properties. The internal iteration scheme shown better properties compare with the operator splitting scheme for which absolute stability have been proven.

Second, the steady solutions of the lid-driven cavity flow problem have been received by the internal iteration scheme up to Re=10000.

Third, the new formulation for 2D plane and axisymmetric Navier-Stokes flows proposed by Aristov and Pukhnachev (2004) and Pukhnachev (2004) is implemented numerically.

Fourth, the present dissertation shows that the Aristov-Pukhnachev's formulation is a viable approach for 2D plane and axisymmetric Navier-Stokes flows and can serve as a basis for efficient numerical models.

Finally, the proposed technique can be used in the future for in-depth investigations of the bifurcation phenomena in rotating flows.

6.3   Recommendations for future research

The following recommendations can be given for future research based on the current work. As the first category, convergence acceleration techniques for internal iteration scheme are suggested for further developed. Even though the current internal iteration scheme allows to get solution up to Re=10000 the fervor research is required for higher Reynolds number.

As the second category, the developed method for the new form of the Navier-Stokes equations can be applied to a numerical simulation of more complicated flow problem such as, the axisymmetric flow past body or the two-dimensional flow past circular cylinder.

As the last category, further investigation of developed methods is encouraged. The success can be attributed to the adequate physical nature of the auxiliary function.

6.4   References

Aristov, S.N., and Pukhnachev, V.V. (2004). On the equations of axisymmetric motion of a viscous incompressible. **Doklady Physics** 49(2):112–115.

Pukhnachev, V.V. (2004). Integrals of motion of an incompressible fluid occupying the entire space. **Journal of Applied Mechanics and Technical Physics** 45(2):167–171.

APPENDICES

APPENDIX A

DEFINITIONS OF MAIN TENSOR

OPERATIONS IN THE CURVILINEAR

COORDINATE SYSTEM

For the sake of simplicity we consider here coordinates in three-dimensional Euclidean space $\mathbb{R}^3$. All facts and definitions are valid in arbitrary space $\mathbb{R}^n$.

A set of triples (K^1, K^2, K^3), where K^1, K^2, K^3 are real numbers, is called an arithmetic spaces A^3. For all elements of A^3 the operations of summation, subtraction and multiplication by a scalar, and dot product are defined by usual way. For example,

$$(K^1, K^2, K^3) \cdot (L^1, L^2, L^3) = K^1 L^1 + K^2 L^2 + K^3 L^3.$$

Let $\Omega \subset \mathbb{R}^3(\bar{x})$ be an open set. A one-to-one and reciprocal continuously differentiable mapping $K : \Omega \longrightarrow A^3$ is called a coordinate system. This mapping is defined by the formula

$$\bar{x} \to K(\bar{x}) = (K^1(\bar{x}), K^2(\bar{x}), K^3(\bar{x})).$$

The values of the functions $K^i(\bar{x})$ are called the coordinates (curvilinear coordinates) of the point $\bar{x}$.

For any fixed point x_0 the equation $K^i(\bar{x}) = K^i(\bar{x})_0$ determines a coordinate surface $\Pi_i \subset \mathbb{R}^3$. This coordinate surface passes through the point $\bar{x}_0$. Any pair Π_i, Π_j of these surfaces is intersected along the curves

$$l_1 = \Pi_2 \cap \Pi_3, \; l_2 = \Pi_3 \cap \Pi_1, \; l_3 = \Pi_1 \cap \Pi_2,$$

which are called coordinate curves (or curvilinear axes of coordinates). Along the l_i-line only the coordinate K^i is changed; two other coordinates are constants. Let a point $\bar{x} \in \Omega$ be fixed. At this point there are vectors

$$\bar{e}_i = \frac{\partial \bar{x}}{\partial K^i}, \quad \bar{e}^{\,i} = \frac{\partial K^i}{\partial \bar{x}} = \nabla K^i, \;\; (i = 1, 2, 3), \tag{A.1}$$

which form a basis $\{\bar{e}_i\}$ and cobasis $\{\bar{e}^{\,i}\}$ in $\mathbb{R}^3$. These bases are called a coordinate basis and cobasis of the coordinate system K at the point $\bar{x}$. A vector $\bar{e}_i$ is a tangent vector to the coordinate line l_i. The vector $\bar{e}^i$ are normal to the coordinate surface Π_i. A vector $\bar{v}$ can be decomposed along either basis or cobasis vectors

$$\bar{v} = v_i \bar{e}^{\,i} = v^i \bar{e}_i.$$

The components v_i are called covariant components of the vector $\bar{v}$ and the components v^i are called contravariant components of the vector $\bar{v}$. A coordinate system is called orthogonal (at a point or on a set) if its basis is orthogonal (at the point or on the set).

$$\bar{e}_i \cdot \bar{e}_j = 0, \;\; \bar{e}^{\,i} \cdot \bar{e}^{\,j} = 0, \; (i \neq j).$$

The fundamental tensor and its inverse are defined by

$$g_{ij} = \bar{e}_i \cdot \bar{e}_j, \qquad g^{ij} = \bar{e}^{\,i} \cdot \bar{e}^{\,j}. \tag{A.2}$$

Coordinates of the fundamental tensor g with respect to an orthogonal coordinate system are

$$(g_{ij}) = \begin{bmatrix} g_{11} & 0 & 0 \\ 0 & g_{22} & 0 \\ 0 & 0 & g_{33} \end{bmatrix}, \quad (g^{ij}) = \begin{bmatrix} g^{11} & 0 & 0 \\ 0 & g^{22} & 0 \\ 0 & 0 & g^{33} \end{bmatrix},$$

where

$$g_{ii} = |\bar{e}_i|^2 = \left| \frac{\partial \bar{x}}{\partial K^i} \right|^2, \quad g^{ii} = |\bar{e}^{\,i}|^2 = |\nabla K^i|^2, \quad i = 1, 2, 3; \quad |g| = [\bar{e}_1 \cdot (\bar{e}_2 \times \bar{e}_3)]^2.$$

Vectors of a coordinate basis $\{\bar{e}_i\}$ depend on $\bar{x}$ or on $(K^1, K^2, K^3) = K(\bar{x})$. The derivatives of the basis vectors can be represented in terms of the basis $\{\bar{e}_i\}$

$$\frac{\partial \bar{e}_i}{\partial K^j} = \Gamma_{ij}^s \bar{e}_s,$$

where the coefficients Γ_{ij}^s are called Christoffel's symbols of second-order. Note that the Christoffel's symbols are not components of any tensor. These symbols are symmetric with respect to lower indices

$$\Gamma_{ij}^s = \Gamma_{ji}^s.$$

A dual formula for the representation of the Christoffel's symbols is

$$\frac{\partial \bar{e}^{\,i}}{\partial K^j} = -\Gamma_{js}^i \bar{e}^{\,s}.$$

The Christoffel's symbols are related to the derivatives of the fundamental tensor

$$\Gamma_{ij}^l = \frac{1}{2}\left(\frac{\partial g_{is}}{\partial K^j} + \frac{\partial g_{js}}{\partial K^i} - \frac{\partial g_{ij}}{\partial K^s}\right) g^{ls}. \tag{A.3}$$

Note that

$$\Gamma_{is}^s = \frac{1}{\sqrt{|g|}}\frac{\partial \sqrt{|g|}}{\partial K^i}, \ \ (i = 1, 2, 3),$$

where $|g| = \det(g_{ij})$. Covariant derivatives are expressed in terms of partial derivatives with respect to corresponding coordinates, Christoffel symbols and components of a tensor. The simplest are covariant derivatives of a scalar field F which coincide with the usual partial derivatives

$$F_{,i} = \frac{\partial F}{\partial K^i}.$$

The covariant derivatives of the covariant and contravariant components of a second order tensor Φ are

$$\Phi_{ij,l} = \frac{\partial \Phi_{ij}}{\partial K^l} - \Gamma_{li}^s \Phi_{sj} - \Gamma_{lj}^s \Phi_{is},$$

$$\tag{A.4}$$

$$\Phi_{,l}^{ij} = \frac{\partial \Phi^{ij}}{\partial K^l} + \Gamma_{ls}^i \Phi^{sj} + \Gamma_{ls}^j \Phi^{is}.$$

Similarly, the covariant derivatives of the mixed components are

$$\Phi_{i.,l}^{.j} = \frac{\partial \Phi_{i.}^{.j}}{\partial K^l} - \Gamma_{li}^s \Phi_{s.}^{.j} + \Gamma_{ls}^j \Phi_{i.}^{.s},$$

$$\Phi_{.i,l}^{j.} = \frac{\partial \Phi_{.i}^{j.}}{\partial K^l} - \Gamma_{li}^s \Phi_{.s}^{j.} + \Gamma_{ls}^j \Phi_{.i}^{s.}.$$

(A.5)

In the above equations and everywhere below, a comma with an index in a subscript denotes covariant differentiation. A derivative of the vector field $\bar{v}$ is the second order tensor which is denoted by the symbol $\left(\dfrac{\partial \bar{v}}{\partial \bar{x}} \right)$. Covariant and mixed coordinates of the $\left(\dfrac{\partial \bar{v}}{\partial \bar{x}} \right)$ are

$$\left(\frac{\partial \bar{v}}{\partial \bar{x}} \right)_{ij} = \frac{\partial v_i}{\partial K^j} - \Gamma_{ij}^s v_s = v_{i,j},$$

$$\left(\frac{\partial \bar{v}}{\partial \bar{x}} \right)^i_{,j} = \frac{\partial v^i}{\partial K^j} + \Gamma_{js}^i v_s = v^i_{,j}.$$

(A.6)

The divergence of a vector field $\bar{v}$ is a scalar

$$\mathrm{div}\bar{v} = tr \left(\frac{\partial \bar{v}}{\partial \bar{x}} \right) = e^i \left(\frac{\partial \bar{v}}{\partial \bar{x}} \right) \langle e_i \rangle.$$

The divergence can be expressed in terms of the covariant derivatives of the contravariant components of vector field $\bar{v}$

$$\mathrm{div}\,\bar{v} = v^i_{,i} = \frac{\partial v^i}{\partial K^i} + \Gamma_{is}^i v^s = \frac{\partial v^i}{\partial K^i} + \frac{v^i}{\sqrt{|g|}} \frac{\partial \sqrt{|g|}}{\partial K^i} = \frac{1}{\sqrt{|g|}} \frac{\partial}{\partial K^i} \left(\sqrt{|g|} v^i \right). \quad (A.7)$$

The vector

$$\nabla F = \frac{\partial F}{\partial \bar{x}} = \frac{\partial F}{\partial K^i} \, \bar{e}^{\, i}$$

is called a gradient of the scalar function F. Covariant components of the gradient vector are

$$(\nabla F)_i = F_{,i} = \frac{\partial F}{\partial K^i}.$$

(A.8)

The scalar

$$\triangle F = \mathrm{div}\,(\nabla F) = ((\nabla F)^i)_{,i} = (g^{is} (\nabla F)_s)_{,i} =$$

$$= \left(g^{is} \frac{\partial F}{\partial K^s} \right)_{,i} = g^{is} \left(\frac{\partial F}{\partial K^s} \right)_{,i} = g^{is} \left[\frac{\partial^2 F}{\partial K^s \partial K^i} - \Gamma^{\alpha}_{is} \frac{\partial F}{\partial K^{\alpha}} \right]$$

is called the Laplace operator of the scalar function F. We can rewrite this formula in the following form

$$\triangle F = \frac{1}{\sqrt{|g|}} \frac{\partial}{\partial K^i} \left(\sqrt{|g|} g^{is} \frac{\partial F}{\partial K^s} \right). \tag{A.9}$$

A curl of a vector $\bar{v}$ is a vector

$$\mathrm{curl}\, \bar{v} = E^{-1} \left\langle \left(\frac{\partial \bar{v}}{\partial \bar{x}} \right) - \left(\frac{\partial \bar{v}}{\partial \bar{x}} \right)^* \right\rangle.$$

For obtaining contravariant components of this vector there is

$$E \left\langle \mathrm{curl}\, \bar{v} \right\rangle = \left(\frac{\partial \bar{v}}{\partial \bar{x}} \right) - \left(\frac{\partial \bar{v}}{\partial \bar{x}} \right)^*.$$

In one uses a right-handed basis, then $\varepsilon_{123} = \bar{e}_1 \cdot (\bar{e}_2 \times \bar{e}_3) = \sqrt{|g|}$, the contravariant components of $\mathrm{curl}\, \bar{v}$ are

$$
\begin{aligned}
(\mathrm{curl}\, \bar{v})^1 &= \frac{1}{\sqrt{|g|}} \left(\frac{\partial v_3}{\partial K^2} - \frac{\partial v_2}{\partial K^3} \right), \\
(\mathrm{curl}\, \bar{v})^2 &= \frac{1}{\sqrt{|g|}} \left(\frac{\partial v_1}{\partial K^3} - \frac{\partial v_3}{\partial K^1} \right), \\
(\mathrm{curl}\, \bar{v})^3 &= \frac{1}{\sqrt{|g|}} \left(\frac{\partial v_2}{\partial K^1} - \frac{\partial v_1}{\partial K^2} \right).
\end{aligned}
\tag{A.10}
$$

The divergence of a tensor is a vector. The s-th contravariant component of this vector is

$$(\mathrm{div}\, P)^s = P^{sj}_{,j} = \mathrm{div}\, (\overline{P}^s) + \Gamma^s_{j\alpha} P^{j\alpha} \tag{A.11}$$

where $\overline{P}^s = (P^{s1}, P^{s2}, P^{s3})$ is s-th row of a matrix which represents second-order tensor P and

$$\mathrm{div}\, (\overline{P}^s) = \frac{\partial P^{sj}}{\partial K^j} + \Gamma^j_{j\alpha} P^{s\alpha}.$$

The vector

$$\Delta \bar{v} = \mathrm{div}\, \left(\frac{\partial \bar{v}}{\partial \bar{x}} \right)$$

is called the Laplace operator of the vector $\bar{v}$. Contravariant components of this vector are

$$(\triangle\bar{v})^l = g^{ij}\left(\left(\frac{\partial\bar{v}}{\partial\bar{x}}\right)^{l.}_{.j}\right)_{,i} = g^{ij}(v^l_{,i})_{,j} = g^{ij}\left[\frac{\partial v^l_{,i}}{\partial K^j} - \Gamma^s_{ji}v^l_{,s} + \Gamma^l_{js}v^s_{,i}\right] =$$

$$= g^{ij}\left[\left(\frac{\partial^2 v^l}{\partial K^j\partial K^i} + \frac{\partial\Gamma^l_{is}}{\partial K^j}v^s + \Gamma^l_{is}\frac{\partial v^s}{\partial K^j}\right) - \Gamma^s_{ji}\left(\frac{\partial v^l}{\partial K^s} + \Gamma^l_{s\alpha}v^\alpha\right)\right.$$

$$\left. + \Gamma^l_{js}\left(\frac{\partial v^s}{\partial K^i} + \Gamma^s_{i\alpha}v^\alpha\right)\right].$$

After regrouping, one has

$$(\triangle\bar{v})^l = (\triangle v^l) + 2g^{ij}\Gamma^l_{is}\frac{\partial v^s}{\partial K^j} + g^{ij}\left(\frac{\partial\Gamma^l_{is}}{\partial K^j} - \Gamma^\alpha_{ji}\Gamma^l_{\alpha s} + \Gamma^l_{j\alpha}\Gamma^\alpha_{is}\right)v^s \qquad (A.12)$$

where $(\triangle v^l) = g^{ij}\left[\frac{\partial^2 v^l}{\partial K^j\partial K^i} - \Gamma^s_{ji}\frac{\partial v^l}{\partial K^s}\right]$ is the Laplace operator of scalar function v^l. The vector

$$\frac{d\bar{v}}{dt} = \frac{\partial\bar{v}}{\partial t} + \frac{\partial\bar{v}}{\partial\bar{x}}\langle\bar{v}\rangle$$

Covariant and contravariant components of the acceleration are

$$\left(\frac{d\bar{v}}{dt}\right)_i = \frac{\partial v_i}{\partial t} + v^s v_{i,s} = \frac{\partial v_i}{\partial t} + v^s\frac{\partial v_i}{\partial K^s} - \Gamma^j_{is}v^s v_j,$$

$$\left(\frac{d\bar{v}}{dt}\right)^i = \frac{\partial v^i}{\partial t} + v^s v^i_{.,s} = \frac{\partial v^i}{\partial t} + v^s\frac{\partial v^i}{\partial K^s} + \Gamma^i_{js}v^j v^s.$$

$$(A.13)$$

If vectors of coordinate bases and cobases are not normed, then components of tensors have different numerical values in different bases even if directions of basis vectors coincides. Numerical values of tensor components divided by the length of corresponding basis or cobasis vectors, which define these components are called physical components of the tensor. For example, if $a_i = \bar{a}\bar{e}_i$ are covariant coordinates of a vector $\bar{a}$, then the physical components are

$$\tilde{a}_i = \frac{a_i}{|\bar{e}_i|}, \qquad (A.14)$$

the covariant components of a tensor L_{ij} related with the physical components as

$$\widetilde{L}_{ij} = \frac{L_{ij}}{(|\bar{e}_i|\,|\bar{e}_j|)}. \qquad (A.15)$$

APPENDIX B

THE CYLINDRICAL COORDINATE SYSTEM

The transformation K from the rectangular coordinates to the cylindrical coordinates can be expressed as

$$K^1 = \sqrt{x^2 + y^2}, \quad K^2 = \arctan \frac{y}{x}, \quad K^3 = z,$$

where the inverse mapping K^{-1} is

$$x = r \cos \theta, \quad y = r \sin \theta, \quad z = z, \quad (0 \le \theta \le 2\pi).$$

Coordinate surfaces $r = const > 0$ are circular cylinders (coaxial to $z-$axis), $\theta = const$ are half-planes passing through $z-$axis and $z = const$ are planes perpendicular to $z-$axis. Coordinate curves are: l_1 (intersection of $\theta = const$ and $z = const$) are straight rays going from $z-$axis and perpendicular to it; l_2 (intersection of $r = const$ and $z = const$) are circles (these circles lie on the planes, which are perpendicular to $z-$axis with a center in the $z-$axis); l_3 (intersection of $r = const$ and $\theta = const$) are straight lines that are parallel to $z-$axis.

The basis and cobasis of the cylindrical coordinate system are orthogonal and consist of the vectors

$$\bar{e}_1 = \frac{\partial \bar{x}}{\partial K^1} = \left(\frac{\partial x}{\partial r}, \frac{\partial y}{\partial r}, \frac{\partial z}{\partial r} \right) = (\cos \theta, \sin \theta, 0),$$

$$\bar{e}_2 = \frac{\partial \bar{x}}{\partial K^2} = \left(\frac{\partial x}{\partial \theta}, \frac{\partial y}{\partial \theta}, \frac{\partial z}{\partial \theta} \right) = r(-\sin \theta, \cos \theta, 0),$$

$$\bar{e}_3 = \frac{\partial \bar{x}}{\partial K^3} = \left(\frac{\partial x}{\partial z}, \frac{\partial y}{\partial z}, \frac{\partial z}{\partial z} \right) = (0, 0, 1),$$

$$\bar{e}^1 = \frac{\partial K^1}{\partial \bar{x}} = \left(\frac{\partial K^1}{\partial x}, \frac{\partial K^1}{\partial y}, \frac{\partial K^1}{\partial z} \right) = (\cos \theta, \sin \theta, 0),$$

$$\bar{e}^2 = \frac{\partial K^2}{\partial \bar{x}} = \left(\frac{\partial K^2}{\partial x}, \frac{\partial K^2}{\partial y}, \frac{\partial K^2}{\partial z} \right) = \frac{1}{r}(-\sin\theta, \cos\theta, 0),$$

$$\bar{e}^3 = \frac{\partial K^3}{\partial \bar{x}} = \left(\frac{\partial K^3}{\partial x}, \frac{\partial K^3}{\partial y}, \frac{\partial K^3}{\partial z} \right) = (0, 0, 1).$$

Hence,

$$\bar{e}_1 = (\cos\theta, \sin\theta, 0), \quad \bar{e}_2 = r(-\sin\theta, \cos\theta, 0), \quad \bar{e}_3 = (0, 0, 1),$$

$$\bar{e}^1 = (\cos\theta, \sin\theta, 0), \quad \bar{e}^2 = \frac{1}{r}(-\sin\theta, \cos\theta, 0), \quad \bar{e}^3 = (0, 0, 1).$$

The fundamental tensor is

$$(g_{ij}) = \begin{bmatrix} 1 & 0 & 0 \\ 0 & r^2 & 0 \\ 0 & 0 & 1 \end{bmatrix}, \quad (g^{ij}) = \begin{bmatrix} 1 & 0 & 0 \\ 0 & \dfrac{1}{r^2} & 0 \\ 0 & 0 & 1 \end{bmatrix}, \quad |g| = r^2.$$

The Christoffel symbols $(A.3)$ for the cylindrical coordinate system are

$$\Gamma^2_{12} = \Gamma^2_{21} = \frac{1}{r}, \quad \Gamma^1_{22} = -r$$

and all others are equal to zero. For example,

$$\Gamma^2_{12} = \frac{1}{2} g^{2s} \left(\frac{\partial g_{1s}}{\partial K^2} + \frac{\partial g_{2s}}{\partial K^1} - \frac{\partial g_{12}}{\partial K^s} \right) = \frac{1}{2} g^{22} \left(\frac{\partial g_{12}}{\partial K^2} + \frac{\partial g_{22}}{\partial K^1} - \frac{\partial g_{12}}{\partial K^s} \right) = \frac{1}{2} \frac{1}{r^2} 2r = \frac{1}{r}.$$

For the permutation tensor is $\varepsilon_{123} = r$ with

$$\varepsilon_{123} = \varepsilon_{231} = \varepsilon_{321} = -\varepsilon_{321} = -\varepsilon_{213} = -\varepsilon_{132}.$$

Since cylindrical coordinate system is orthogonal, then all physical components of any type coincide. Let (u, v, w) be physical components of a vector $\bar{v}$, then the tensor components of the vector $\bar{v}$ are

$$(v^1, v^2, v^3) = (u, \frac{v}{r}, w), \quad (v_1, v_2, v_3) = (u, rv, w).$$

We remind that physical components of a vector are related with covariant components by the formulae:

$$\tilde{v}_2 = \frac{v_2}{|e_2|} = \frac{v_2}{r}, \quad v_2 = r\tilde{v}_2 = rv.$$

Let P^{ij} are contravariant components of a second order tensor P. The physical components of $\widetilde{P}^{ij}$ are

$$\widetilde{P}^{ij} = \frac{P^{ij}}{(|\vec{e}^i||\vec{e}^j|)}.$$

For examples of the cylindrical coordinate system are

$$\widetilde{P}^{21} = \frac{P^{21}}{(|\vec{e}^2||\vec{e}^1|)} = rP^{21}, \quad P^{21} = \frac{1}{r}\widetilde{P}^{21} = \frac{1}{r}P_{\theta r}.$$

Hence, if the physical components of a tensor P are

$$P = \begin{bmatrix} P_{rr} & P_{r\theta} & P_{rz} \\ P_{\theta r} & P_{\theta\theta} & P_{\theta z} \\ P_{zr} & P_{z\theta} & P_{zz} \end{bmatrix},$$

then contravariant components of the tensor P are

$$(P^{ij}) = \begin{bmatrix} P_{rr} & \frac{1}{r}P_{r\theta} & P_{rz} \\ \frac{1}{r}P_{\theta r} & \frac{1}{r^2}P_{\theta\theta} & \frac{1}{r}P_{\theta z} \\ P_{zr} & \frac{1}{r}P_{z\theta} & P_{zz} \end{bmatrix}.$$

The coordinates of the gradient of a function F is

$$(\nabla F)_1 = (\nabla F)^1 = \frac{\partial F}{\partial r},$$

$$(\nabla F)_2 = \frac{\partial F}{\partial \theta}, \quad (\nabla F)^2 = \frac{1}{r^2}\frac{\partial F}{\partial \theta},$$

$$(\nabla F)_3 = (\nabla F)^3 = \frac{\partial F}{\partial z}.$$

A matrix of covariant derivatives

$$\Phi^i_{,j} = \frac{\partial \Phi^i}{\partial K^j} + \Gamma^i_{js}\Phi^s$$

is (here i is the number of a row)

$$(v^i_{,j}) = \begin{bmatrix} \dfrac{\partial u}{\partial r} & \dfrac{\partial u}{\partial \theta} - v & \dfrac{\partial u}{\partial z} \\ \dfrac{1}{r}\dfrac{\partial v}{\partial r} & \dfrac{1}{r}\dfrac{\partial v}{\partial \theta} + \dfrac{v}{r} & \dfrac{1}{r}\dfrac{\partial v}{\partial z} \\ \dfrac{\partial w}{\partial r} & \dfrac{\partial w}{\partial \theta} & \dfrac{\partial w}{\partial z} \end{bmatrix}.$$

Because

$$\text{div } \overline{v} = \frac{1}{\sqrt{g}} \frac{\partial}{\partial K^i} \left(\sqrt{g} v^i \right),$$

the divergence of a vector $\overline{v}$ can be expressed as follows

$$\nabla \cdot \overline{v} = \frac{1}{r} \frac{\partial (ru)}{\partial r} + \frac{1}{r} \frac{\partial v}{\partial \theta} + \frac{\partial w}{\partial z}.$$

Similar for the Laplace operator of a function F in expression $(A.9)$ hence,

$$\triangle F = \frac{1}{r} \frac{\partial}{\partial r} \left(r \frac{\partial F}{\partial r} \right) + \frac{1}{r^2} \frac{\partial^2 F}{\partial \theta^2} + \frac{\partial^2 F}{\partial z^2}.$$

Here we use the representation $(A.10)$ for contravariant components of curl of a vector $\overline{v}$ leading to

$$\omega^1 = \frac{1}{r} \frac{\partial w}{\partial \theta} - \frac{\partial v}{\partial z}, \quad \omega^2 = \frac{1}{r} \frac{\partial w}{\partial z} - \frac{1}{r} \frac{\partial w}{\partial r}, \quad \omega^3 = \frac{1}{r} \frac{\partial (rv)}{\partial r} - \frac{1}{r} \frac{\partial u}{\partial \theta}.$$

The divergence of a tensor P is a vector with contravariant components. By using equation $(A.11)$, yields

$$(\text{div } P)^1 = \text{div } (\overline{P}^1) - \frac{1}{r} P_{\theta\theta}, \quad \overline{P}^1 = (P_{rr}, \frac{1}{r} P_{r\theta}, P_{rz}),$$

$$(\text{div } P)^2 = \text{div } (\overline{P}^2) + \frac{1}{r^2} (P_{r\theta} + P_{\theta r}), \quad \overline{P}^2 = (\frac{1}{r} P_{\theta r}, \frac{1}{r^2} P_{\theta\theta}, \frac{1}{r} P_{\theta z}),$$

$$(\text{div } P)^3 = \text{div } (\overline{P}^3), \quad \overline{P}^1 = (P_{zr}, \frac{1}{r} P_{z\theta}, P_{zz}).$$

Therefore,

$$(div \ P)^1 = \frac{1}{r} \frac{\partial}{\partial r} (r P_{rr}) + \frac{1}{r} \frac{\partial}{\partial \theta} (P_{r\theta}) + \frac{\partial}{\partial z} (P_{rz}) - \frac{1}{r} \frac{\partial}{\partial \theta} (P_{\theta\theta}),$$

$$(div \ P)^2 = \frac{1}{r} \frac{\partial}{\partial r} (P_{\theta r}) + \frac{1}{r^2} \frac{\partial}{\partial \theta} (P_{r\theta}) + \frac{1}{r} \frac{\partial}{\partial z} (P_{\theta z}) + \frac{1}{r^2} (P_{r\theta} + P_{\theta r}),$$

$$(div \ P)^3 = \frac{1}{r} \frac{\partial}{\partial r} (r P_{zr}) + \frac{1}{r} \frac{\partial}{\partial \theta} (P_{z\theta}) + \frac{\partial}{\partial z} (P_{zz}).$$

The Laplace operator of a vector $\overline{v}$ is the vector with contravariant components

$$\triangle (\overline{v})^1 = \triangle (u) - \frac{2}{r^2} \frac{\partial v}{\partial \theta} - \frac{u}{r^2},$$

$$\triangle \left(\overline{v} \right)^2 = \triangle \left(\frac{v}{r} \right) + \frac{2}{r} \left(\frac{v}{r} \right) + \frac{2}{r^3} \frac{\partial u}{\partial \theta},$$

$$\triangle \left(\overline{v} \right)^3 = \triangle \left(w \right).$$

The acceleration has the components

$$\left(\frac{d\overline{v}}{dt} \right)^1 = D(u) - \frac{v^2}{r}, \quad \left(\frac{d\overline{v}}{dt} \right)^2 = \frac{1}{r} D(v) + \frac{uv}{r^2}, \quad \left(\frac{d\overline{v}}{dt} \right)^3 = D(w),$$

where

$$D(f) = \frac{\partial f}{\partial t} + u \frac{\partial f}{\partial r} + \frac{v}{r} \frac{\partial f}{\partial \theta} + w \frac{\partial f}{\partial z}.$$

CURRICULUM VITAE

NAME: Kanyuta Poochinapan.   **SEX:** Female.   **NATIONALITY:** Thai.

DATE OF BIRTH: March 25, 1977.   **MARITAL STATUS:** Single.

EDUCATIONAL BACKGROUND:

- B. Sc. in Mathematics, Chiang Mai University, Chiang Mai, Thailand, 1999.

- M. Sc. in Applied Mathematics, Chiang Mai University, Chiang Mai, Thailand, 2001.

- Student (Non-degree), Department of Mathematics, University of Louisiana at Lafayette, Lafayette, Louisiana, USA, August 2005 - July 2006.

WORK EXPERIENCE:

- Lecturer in Mathematics Department, Chiang Mai University, Chiang Mai, Thailand since 2001.

SCHOLARSHIPS:

- The Ministry of University Affairs of Thailand (MUA), 2003-2005.